Title
Mesoscale to Microscale Atmospheric Modeling Over Complex Terrain

Author
Wiersema, David

Publication Date
2020

Peer reviewed|Thesis/dissertation

Mesoscale to Microscale Atmospheric Modeling Over Complex Terrain

by

David Wiersema

A dissertation submitted in partial satisfaction of the

requirements for the degree of

Doctor of Philosophy

in

Engineering - Civil and Environmental Engineering

in the

Graduate Division

of the

University of California, Berkeley

Committee in charge:

Professor Fotini Katopodes Chow, Chair
Professor Robert Harley
Professor Inez Fung

Fall 2019

Mesoscale to Microscale Atmospheric Modeling Over Complex Terrain

Abstract

Mesoscale to Microscale Atmospheric Modeling Over Complex Terrain

by

David Wiersema

Doctor of Philosophy in Engineering - Civil and Environmental Engineering

University of California, Berkeley

Professor Fotini Katopodes Chow, Chair

Microscale atmospheric simulations of the planetary boundary layer are frequently used for wind energy forecasting, emergency response, mountain meteorology, air pollution modeling, and numerous other applications involving atmospheric flows over complex terrain. These models are typically configured using local observations and are limited to resolving only microscale flow features. Mesoscale meteorology, regional influences, and large-scale turbulence are not resolved with the traditional microscale modeling techniques. This dissertation details a series of developments to the Weather Research and Forecasting (WRF) model that enable mesoscale to microscale (i.e. multiscale) simulations. These multiscale simulations dynamically downscale meteorological conditions through a series of nested domains with increasingly high resolution, which allows mesoscale meteorology, regional influence, and large-scale flow features to influence microscale simulations.

Over steep terrain, the WRF model develops numerical errors that are due to grid deformation of the terrain-following coordinates. An alternative gridding technique, the immersed boundary method (IBM), has been implemented into the WRF model (Lundquist et al. 2012; Bao et al. 2018). Use of an IBM allows for microscale simulations over highly complex terrain (i.e. urban or mountainous). Here, an IBM and the WRF model's grid-nesting framework have been modified to seamlessly work together, which allows for a microscale large-eddy simulation over complex terrain with an IBM to be nested within a traditional mesoscale WRF simulation (Wiersema et al. 2020). Additionally, grid configurations are controlled using the vertical grid nesting method of Daniels et al. (2016) and turbulence development at intermediate resolutions is improved using the cell perturbation method of Muñoz-Esparza et al. (2015). Multiscale simulations are extremely challenging to configure due to the sensitivity of each nested domain to its configuration and to the configuration of its parent domain(s). This dissertation also begins to investigate the model sensitivity to grid resolution and surface boundary condition, which is integral information for modelers configuring the nested domains of future multiscale simulations.

Multiscale simulations are demonstrated for the prediction of transport and mixing of a tracer gas (SF_6) released in the central business district of Oklahoma City during the

Joint Urban 2003 field campaign. The simulations use either 5 or 6 nested domains with horizontal resolutions that range from several kilometers for the outermost domain to 2 m for the innermost domain. The multiscale simulations are compared with microscale-only simulations and with observations of wind speed, wind direction, and SF_6 concentrations. The microscale-only simulations use idealized lateral boundary conditions and are configured using local meteorological observations from the field campaign. The multiscale simulation, which is configured independent of local observations, shows similar model skill predicting wind speed and wind direction, and improved skill predicting SF_6 concentrations and turbulence kinetic energy when compared with the microscale-only simulations. Additionally, the multiscale simulation includes the effects of large-scale flow features and turbulence that the microscale-only simulations are incapable of resolving, which is shown to have a dramatic effect on predictions of transport and mixing. The analysis of simulations in this dissertation demonstrates the potential for multiscale simulations to improve predictions of transport and mixing over highly complex terrain and enable microscale simulations where local observations are not available.

To my parents, Michael and Kimberly Wiersema.

Contents

List of Figures

List of Tables

Acknowledgments

First and foremost, thank you to Tina Katopodes Chow and Katherine Lundquist for years of mentoring, guidance, and friendship.

The environmental fluid mechanics research group at UC Berkeley has provided extensive encouragement and peer review, without which this research would not be possible.

A great many people, too many to name, have supported me through cancer diagnosis, treatment, and recovery. I, and this research, would not be here without their support. Thank you.

I am especially grateful for the support of a Lawrence Scholars Program Fellowship from Lawrence Livermore National Laboratory (LLNL). Lawrence Livermore National Laboratory is operated by Lawrence Livermore National Security, LLC, for the U.S. Department of Energy, National Nuclear Security Administration under Contract DE-AC52-07NA27344.

Chapter 1

Introduction

1.1 Motivation

> "When dealing with pollution transport and dispersion in such flows one must take into account such interactions between meteorology and the local topography. Given sufficient resources, one can now do this through detailed, three-dimensional numerical modeling of the wind field and the resulting dispersion. Such methods bring along a host of new issues, including descriptions of the unresolvable subgrid-scale processes, incorporation of real data on initial and boundary conditions into the model, and model validation. This type of wind field modeling is in the mainstream of mesoscale meteorology today (Ray 1986), although its applications to dispersion are not as common. Given the increasing availability of supercomputers this approach might become more accessible as time goes on." (Venkatram and Wyngaard 1988, p. 56)

Three decades after this was written, high-resolution atmospheric simulations of flow through complex topography continue to lack realistic meteorological input, do not include regional or synoptic effects, and struggle with representing subgrid-scale processes. Recent simulations fall into two categories; low resolution simulations that easily include realistic meteorological input and regional effects but must parameterize important subgrid-scale processes, such as turbulence or the effects of complex terrain; and high resolution simulations that resolve important microscale meteorological processes but omit the effects of regional and mesoscale meteorology.

This dissertation details the development and validation of a modeling framework for high-resolution atmospheric simulations of flow through complex topography that resolves meteorological effects at scales as fine as ~ 2 m. The remainder of Chapter 1 is devoted to background knowledge and context. Chapter 2 introduces the multiscale modeling framework and the associated model developments. Chapter 3 suggests best practices for multiscale model configurations by evaluating simulation errors over complex terrain using a suite of grid resolutions and bottom boundary conditions. Chapter 4 investigates the representation

of turbulence in a multiscale simulation and its effects on transport and mixing. Chapter 5 summarizes the developments, findings, and contributions described in this dissertation and includes suggestions for future research that may further improve multiscale atmospheric simulations.

1.2 Background

Numerical weather prediction

In 1922, Lewis Fry Richardson proposed a method of weather forecasting by solving differential equations via a method of finite differences on a geographic grid. Using methods similar to those proposed by Richardson, the first successful numerical weather prediction (NWP) simulation (Charney et al. 1950) was performed soon after the construction of ENIAC, the first electronic general purpose computer. The two-dimensional NWP simulation could only resolve the largest atmospheric circulations but it demonstrated the feasibility of NWP and established techniques that persist in modern NWP simulations. Soon thereafter, improved performance of computing platforms enabled a "2.5-dimensional" simulation that resolved limited vertical variability (Charney and Phillips 1953). From these first NWP simulations until today, there has existed a persistent trend of improvements in computing resources being in lockstep with the fidelity and resolution of NWP simulations.

Scales of variability in the atmosphere range from approximately 10^6 to 10^{-2} m (Charney 1948; Tennekes and Lumley 1972; Holton 2004). The first NWP models used very coarse resolution grids and were capable of resolving only the largest scales of atmospheric phenomena (i.e. synoptic scales). In comparison, modern operational NWP models have grids approaching 1 km horizontal resolution and resolve a much wider range of scales (i.e. synoptic to regional) that includes behavior such as thunderstorm convection and orographic effects. The steady increase in resolved scales of atmospheric variability corresponds with the gradual improvement of forecast skill over the past 60 years.

In addition to grid resolution, the accuracy and range of NWP simulations is intrinsically associated with the quality of data used for initialization and forcing (Lorenz 1963). Improvements in forecast skill correspond with the increases in ground, radiosonde and satellite meteorological observations. Regional NWP models have benefited greatly from the improved skill of global NWP, which are used for initialization and forcing of the regional simulations.

Simulation of the planetary boundary layer

Most recent simulations of the planetary boundary layer (PBL) can be categorized as either mesoscale NWP simulations with grid resolution $\Delta \gtrsim 1$ km or microscale NWP simulations with grid resolution $\Delta \sim 10$ m. Grid resolution limits the smallest scale motions resolved by a simulation. The spatial extent of a simulation limits the largest scale motions

that can be resolved. Mesoscale simulations resolve large-scale meteorological effects with domain extents that range from continental to global but these simulations are unable to resolve microscale effects. In comparison, microscale simulations resolve small-scale effects but cannot resolve mesoscale meteorological effects and the domain extents are limited to regional simulations. As computational resources have improved, mesoscale modelers have pushed to increasingly high resolutions and microscale modelers have expanded their simulation domains to resolve more large-scale effects.

The spatial extent of a NWP simulation is restricted by the balance of available computational resources, the number of grid points, the grid resolution and the model time step. For a simulation to properly resolve the complex physics and meteorology within the PBL, a high spatial and temporal resolution is required. If a simulation is repeated with identical spatial extent but the grid spacing is halved then the total number of grid points is increased by a factor of 8. Additionally, the model time step must be halved to maintain numerical stability and avoid violating the Courant-Friedrichs-Lewy condition (Courant et al. 1928, 1967). Thus, a combination of increasing the total number of grid points and decreasing the time step results in a 16 fold increase in the simulation's computational cost when the grid is refined by a factor of two.

Adequately resolving microscale meteorology requires considerably higher grid resolution than used by mesoscale NWP simulations. This restricts the spatial extent of the simulation and imposes an upper limit to the scales of phenomena that can be resolved by the model. Because microscale behavior within the PBL is highly dependent upon regional and mesoscale meteorology, microscale simulations should be provided with, or approximate the effects of, unresolved large-scales that exist within the PBL. For this reason, potential improvements to microscale NWP simulations can be achieved by downscaling a mesoscale simulation to initialize and force a microscale simulation.

Grid nesting is a commonly used downscaling methodology wherein a "parent" simulation is used to inform lateral boundary conditions of an embedded "child" simulation. This allows for the child domain to be affected by large scales of motion that are resolved only by the parent domain. A wide range of spatial scales can be resolved within a simulation by downscaling through a telescoping sequence of nested domains.

An alternative method of downscaling is adaptive mesh refinement (AMR), where grid resolution is variable and transitions from coarse to fine resolution near regions of interest. This downscaling methodology is well demonstrated by the Model for Prediction Across Scales-Atmosphere (Skamarock et al. 2012). AMR is especially useful when simulating transient behavior that locally requires high resolution, such as shocks. Because the grid resolution is not consistent, physics parameterizations must be consistent and accurate throughout a wide range of potential grid resolutions (i.e. scale-aware). Construction of grids using AMR is tedious and the simulation accuracy is often highly dependent upon the grid quality.

The Weather Research and Forecasting model

The Weather Research and Forecasting (WRF) model is an open source, community developed, NWP model originally developed for mesoscale simulations (Skamarock et al. 2008). WRF is widely used for both operational forecasting and research applications. Immense community development has gradually expanded the model's capabilities to include large eddy simulation (LES) (Moeng et al. 2007; Kirkil et al. 2012; Mirocha et al. 2013), atmospheric chemistry modeling (Grell et al. 2005), four-dimensional data assimilation (Stauffer and Seaman 1990), wildland fire modeling (Coen et al. 2012), advanced atmospheric physics parameterizations, vertical grid refinement during nesting (Daniels et al. 2016), and immersed boundary methods for simulating flow over complex terrain (Lundquist et al. 2012; Bao et al. 2018). WRF is an ideal choice for future development due to the flexible and portable code plus the abundant and diverse group of developers.

The WRF model includes two dynamics solver "cores": the advanced research WRF (ARW) solver and the nonhydrostatic mesoscale model (NMM) solver. The NMM solver is primarily applied to operational simulations. Model developments described in this dissertation are compatible with the ARW solver and are implemented in WRF versions 3.6.1 and 3.8.1.

The ARW solver uses a time-split integration scheme that advances low-frequency modes with a third order Runge-Kutta integration scheme (RK3). High-frequency modes are integrated over each RK3 time step by advancing a perturbation form of the governing equations with a forwards-backwards integration scheme. This time-split approach reduces the model's computational expense by allowing for a larger RK3 time step. A comprehensive description of the ARW time integration scheme is included in the ARW technical note (Skamarock et al. 2008, see Section 3.1).

Spatial discretization schemes between 2^{nd} and 6^{th} order accuracy are available in the ARW solver. For both momentum and scalar variables, the simulations in this dissertation use a 5^{th} order accurate scheme for horizontal advection and a 3^{rd} order accurate scheme for vertical advection. Details regarding the spatial discretization and advection schemes are also included in the ARW technical note (Skamarock et al. 2008, see Section 3.2.3).

The WRF model uses an Arakawa C staggered grid. Pressure and scalar variables, such as potential temperature and water vapor, are defined at vertical half-levels on grid cell centers. The u velocities are defined on centers of the east and west grid cell faces and at vertical half-levels. The v velocities are defined on centers of the south and north grid cell faces and at vertical half-levels. The w velocities are defined on centers of the bottom and top grid cell faces and at vertical full-levels.

The WRF model's vertical coordinate, denoted as η, is terrain-following and a function of the dry hydrostatic-pressure:

$$\eta_k = (p_{hk} - p_{ht}) \,/\, (p_{hs} - p_{ht}) \tag{1.1}$$

where p_{hk}, p_{hs}, and p_{ht} are the hydrostatic pressures at vertical grid index k, the model bottom (i.e. surface), and the model top. η varies between 1.0 at the model bottom and 0.0

at the model top. During a simulation, the η levels remain constant however the pressures and heights at η levels will vary by a small amount.

Downscaling in the WRF model

Downscaling in WRF is accomplished with a grid nesting methodology. Nested domains can optionally be configured to upscale high resolution results to their respective parents (i.e. two-way nesting) (Moeng et al. 2007). The default horizontal grid refinement ratio ($\Delta_{\text{parent}}/\Delta_{\text{child}}$) is 3, however larger refinement ratios are possible (see Figure 2.6 in Chapter 2).

Prior to WRF version 3.8.1, concurrently run nested domains were required to use the same number and placement of vertical grid levels. The ability to refine the vertical grid when nesting, developed in part by this author (Daniels, Lundquist, Mirocha, Wiersema, and Chow 2016), is included within the public release of the WRF code since version 3.8.1.

Boundary conditions in the WRF model

Several idealized lateral boundary conditions (LBCs) are implemented in the WRF model and can be used on domains that are not nested or forced using a downscaled meteorological forecast product, including periodic, symmetric and open LBCs.

Periodic LBCs equate conditions along the west-east and south-north boundaries. Flow can repeatedly recirculate through the domain, which can be especially useful for developing flow in an idealized large-eddy simulation, where the flow would only reach a quasi-steady state after traversing many (i.e. hundreds) of grid points that would be computationally infeasible to simulate. Because grid points along the lateral boundaries are equated, a domain with periodic LBCs must have topography that is identical along the corresponding boundaries, which greatly limits simulations over realistic topography. It should also be noted that simulations with periodic LBCs provide a pseudo infinite domain extent but the largest resolvable scales are still restricted by the grid dimensions. Periodic LBCs are frequently used in idealized simulations because they can provide well-developed turbulence at inflow boundaries.

Open LBCs enforce zero gradients across the lateral boundary for prognostic variables, such as u, v, w and θ. Unlike periodic LBCs, open LBCs do not require matching topography along the lateral boundaries. Because open boundary conditions do not fix magnitudes at the lateral boundaries, variables can globally increase or decrease in magnitude while still satisfying the open boundary conditions. If a simulation does not include constraints for variable magnitudes, then open LBCs can result in a problematic runaway effect, such as wind speeds that continuously increase and eventually lead to model failure. If properly constrained, open LBCs can be useful in idealized simulations over realistic topography that is incompatible with periodic LBCs.

The WRF model's surface boundary condition is variable depending upon the physics parameterizations used. In Chapters 2 and 4, some simulation domains use the Janjić surface

layer scheme (Janjić 2002), the Noah land surface model (LSM) (Chen and Dudhia 2001), and the Mellor Yamada Janjić (MYJ) planetary boundary layer (PBL) scheme.

The Janjić surface layer scheme calculates friction velocities and exchange coefficients at the surface using Monin-Obukhov similarity theory (Monin and Obukhov 1954). The Noah LSM calculates heat and moisture fluxes using information on radiative forcing from the shortwave radiation scheme, precipitation forcing from the microphysics and longwave radiation schemes, and information about the land-surface and state (Skamarock et al. 2008, see p. 73). These heat and moisture fluxes are used by the MYJ PBL scheme as a bottom boundary condition for vertical transport.

Most PBL schemes, including the MYJ PBL scheme, are one-dimensional in the vertical direction and are based on the assumption that the scales of turbulent motions are smaller than the grid resolution and thus the effects of turbulence are not resolved but are instead entirely represented by the parameterization. This assumption is valid for mesoscale simulations (i.e. $\Delta \gtrsim 1$ km) but it is inappropriate at finer resolutions ($\Delta \lesssim 1$ km) where the grid resolution is fine enough to resolve significant turbulent motions. At microscale resolutions, a large-eddy simulation turbulence closure model should be considered in place of a planetary boundary layer scheme.

Large-eddy simulation

At microscale resolutions, NWP simulations begin to resolve influential scales of motion not resolved at mesoscale resolutions, including some of the scales that govern turbulent diffusion. In particular, the microscale NWP simulations can resolve the larger scales of turbulence present in the PBL, with the resolved turbulent scales controlled by the grid resolution.

In an LES simulation, subgrid scale motions, those with a wavelength smaller than the grid resolution (Δ), are removed via a low-pass filter represented by the function $\overline{G}$. Following the procedure in Lesieur and Métais (1996), a scalar or vector field (f) simplifies as follows when filtered,

$$\overline{f}\left(\boldsymbol{x},t\right) = \int f\left(\boldsymbol{x}-\boldsymbol{y},t\right)\overline{G}\left(\boldsymbol{y}\right)d\boldsymbol{y} \tag{1.2}$$

When considering the Navier-Stokes equations,

$$\frac{\partial u_i}{\partial t} + \frac{\partial\left(u_i u_j\right)}{\partial x_j} = -\frac{1}{\rho}\frac{\partial p}{\partial x_i} + \frac{\partial}{\partial x_j}\left[\nu\left(\frac{\partial u_i}{\partial x_j} + \frac{\partial u_j}{\partial x_i}\right)\right], \tag{1.3}$$

applying the filter yields,

$$\frac{\partial \overline{u}_i}{\partial t} + \frac{\partial\left(\overline{u}_i \overline{u}_j\right)}{\partial x_j} = -\frac{1}{\rho}\frac{\partial \overline{p}}{\partial x_i} + \frac{\partial}{\partial x_j}\left[\nu\left(\frac{\partial \overline{u}_i}{\partial x_j} + \frac{\partial \overline{u}_j}{\partial x_i}\right) + T_{ij}\right]. \tag{1.4}$$

T_{ij} is the subgrid scale tensor defined as,

$$T_{ij} = \overline{u}_i\overline{u}_j - \overline{u_i u_j}. \tag{1.5}$$

With an eddy-viscosity assumption, the subgrid scale tensor can be modeled as (for incompressible flow),

$$T_{ij} = 2\nu_t \overline{S}_{ij} + \frac{\delta ij}{3} T_{ij}, \tag{1.6}$$

where the filtered deformation tensor is,

$$\overline{S}_{ij} = \frac{1}{2}\left(\frac{\partial \overline{u}_i}{\partial x_j} + \frac{\partial \overline{u}_j}{\partial x_i}\right). \tag{1.7}$$

Next, a model is required to approximate the eddy viscosity, ν_t. Many such turbulence closure models have been developed with varying levels of accuracy, complexity, and computational cost.

Simulations in this dissertation use the Smagorinsky eddy-viscosity model (Smagorinsky 1963), which assumes the eddy viscosity is proportional to a characteristic turbulent length scale and a characteristic turbulent velocity. Assumptions are made that the characteristic length scale is related to the grid resolution and that the characteristic turbulent velocity is well represented by the local strain rate. This results in an eddy viscosity model

$$\nu_t = \left[C_S \left(\Delta_x \Delta_y \Delta_z\right)^{\frac{1}{3}}\right]^2 \left|\left(2\overline{S}_{ij}\overline{S}_{ij}\right)^{\frac{1}{2}}\right|. \tag{1.8}$$

Typical values of the Smagorinsky coefficient are $0.1 < C_S < 0.25$. The simulations in this dissertation use $C_S = 0.18$. It should be noted that the constant coefficient Smagorisnky model has been found to be overly dissipative and yields excess shear in near-wall regions (Lesieur and Métais 1996; Kirkil et al. 2012). Additionally, the constant coefficient Smagorinsky model is known to produce undesirable elongated flow features (Ludwig et al. 2009) and under-produce small-scale flow features.

The immersed boundary method

The immersed boundary method (IBM) is a technique for imposing the effects of a physical boundary on fluid flow. The first IBM algorithm was demonstrated in 1972 by Charles Peskin with simulations of flow within a human heart that included fluid-boundary interactions. Various IBM algorithms have been developed and applied to a diverse range of applications that includes simulations of flow over moving vehicles, fluid-particle interactions, and geophysical flows (Iaccarino and Verzicco 2003).

The unmodified WRF model is unable to simulate flow over topography with steep resolved slopes because of the limitations imposed by the terrain-following vertical coordinate. Over steep slopes, the grid cells near the bottom boundary are distorted, which introduces numerical errors. An IBM allows for use of a nonconforming grid, which can eliminate errors resulting from grid deformation. Because resolved slopes typically increase as grid resolution is refined, the benefits of an IBM become especially relevant at microscale grid resolutions over complex topography.

Several IBM algorithms have been developed for the WRF model. The first demonstration of an IBM in the WRF model was by Lundquist et al. (2010), who demonstrated two dimensional simulations of flow for canonical cases and over an urban skyline. Lundquist et al. (2012) extended the IBM implementation in WRF for three-dimensional simulations, investigated and improved the IBM's interpolation methods, and demonstrated three-dimensional idealized simulations of flow over urban terrain.

The simulations of Lundquist et al. (2010, 2012) used a ghost-point IBM algorithm that imposed a no-slip surface boundary condition. Bao et al. (2018) demonstrated a velocity-reconstruction IBM algorithm with a surface boundary condition that enforces a log-law by modifying near-surface velocities. Several IBM algorithms in the WRF model are compared in Bao et al. (2016) and Arthur et al. (2019), including an IBM algorithm that modifies shear-stress at grid points near the immersed boundary. Ma and Liu (2017) developed an IBM implementation independent of the codes used in the aforementioned studies and performed idealized simulations of flow over the Bolund hill using the constant coefficient Smagorinsky and the Lagrangian-averaged scale dependent Smagorinsky LES turbulence closure models.

Until recently, WRF simulations with an IBM were restricted to using idealized (i.e. periodic or open) lateral boundary conditions and simplified forcing. Wiersema et al. (2020), included as Chapter 2, demonstrates a multiscale WRF simulation with a sequence of domains extending from mesoscale to microscale grid resolutions, with terrain-following coordinates used at mesoscale resolutions and an IBM used at microscale resolutions. Initial conditions and forcing for the multiscale simulation are supplied by a meteorological forecast product, which is in contrast to the idealized and user-specified initial conditions and forcing used in previous IBM simulations.

1.3 Primary contributions of this research

1. Development of the Weather Research and Forecasting (WRF) model to allow vertical grid refinement during nesting.

2. Implementation of the immersed boundary method (IBM) velocity reconstruction method (VRM) algorithm in the WRF model.

3. Configuration of microscale-only and multiscale (i.e. mesoscale to microscale) simulations of transport and mixing during the Joint Urban 2003 field campaign.

4. Model skill evaluation for microscale-only and multiscale simulation results versus JU2003 observations.

5. Improvement in predictions of transport and mixing from a multiscale simulation relative to a traditional microscale-only simulation.

6. Investigation of model sensitivity to the bottom boundary condition and grid resolution for simulations over complex terrain.

7. Suggestions for the configuration of future multiscale simulations, particularly the intermediate resolution domains.

8. Evaluation of turbulence represented in microscale-only and multiscale simulations of transport and mixing during the Joint Urban 2003 field campaign.

9. Improvement in the representation of turbulence and predictions of turbulent kinetic energy from a multiscale simulation relative to a traditional microscale-only simulation.

10. Suggestions for future research and model development that are focused on improving multiscale atmospheric simulations over complex terrain.

Chapter 2

Mesoscale to microscale atmospheric simulations*

2.1 Introduction

Current numerical weather prediction (NWP) codes have been extensively validated and designed for mesoscale simulations with horizontal resolutions ranging from tens of kilometers to several kilometers (i.e. > 3 km). Advances in computational resources have enabled microscale simulations of the planetary boundary layer (PBL) at large-eddy simulation (LES) resolutions (i.e. < 100 m) that are beyond the original design space of available NWP codes. Downscaling of information from mesoscale to microscale resolutions requires the accurate simulation of phenomena with temporal and spatial scales spanning many orders of magnitude. Multiscale NWP models, if designed to properly simulate scales spanning the mesoscale and microscale, have the potential to greatly improve many applications of NWP, including air quality modeling, emergency response dispersion modeling, and wind energy forecasting.

Several methods have been developed to enable microscale NWP simulations to ingest downscaled mesoscale information. A common approach involves the coupling of separate mesoscale and microscale models. With this method, variables of interest are interpolated from a coarse mesoscale grid onto a high-resolution microscale grid. The coarse time step of mesoscale models and a lack of resolved sub-mesoscale motions often necessitates special treatments to mimic the effect of developed turbulence at inflow boundaries of the microscale model. Using different models for the mesoscale and microscale is further complicated by differences in governing equations, coordinate projections, grid systems, advection schemes, and parameterizations (Baklanov et al. 2002). Despite the potential shortcomings of this

*This chapter is a reproduction, with slight modifications, of the paper "Mesoscale to Microscale Simulations Over Complex Terrain with the Immersed Boundary Method in the Weather Research and Forecasting Model" by David J. Wiersema (the principal author), Katherine A. Lundquist and Fotini Katopodes Chow, published in Monthly Weather Review, January 2020, Volume 148(2), pages 577-595 [Wiersema et al. (2020)],

approach, coupling of mesoscale and microscale models has been found to improve results compared to microscale-only simulations of urban flow and dispersion (Park et al. 2015; Li et al. 2018).

An alternative to coupling separate mesoscale and microscale models is a grid nesting approach where information is dynamically downscaled from a coarse resolution "parent" domain that provides initial and lateral boundary conditions to a fine resolution "child" domain. A multiscale NWP simulation configured with grid nesting is therefore composed of a telescoping sequence of increasingly higher resolution domains. The Weather Research and Forecasting (WRF) model, used in this research, has a grid nesting approach to downscaling that has been previously validated and applied to nested LES simulations (Moeng et al. 2007; Marjanovic et al. 2014; Taylor et al. 2018).

Multiscale modeling with grid nesting may be impaired by poor grid quality (e.g. extreme aspect ratios and skewed cells), a lack of suitable parameterizations at intermediate scales, and difficulty in generating small-scale turbulent motions after grid refinements. Despite these challenges, multiscale modeling with grid nesting holds many advantages over the model coupling approach, such as the ease of updating lateral boundary conditions at each time step, conveniently aligned grids that are configured with a common projection, and compatible numerical methods for each grid.

Many NWP codes, including the WRF model, were originally designed for mesoscale simulations and require extensive development to permit multiscale modeling. WRF's terrain-following vertical coordinate is problematic for high-resolution simulations over complex terrain because grid distortion resulting from steep terrain slopes leads to numerical errors (Klemp et al. 2003; Zangl et al. 2004; Klemp 2011). When grid resolution is refined, steeper terrain slopes are sampled, thus restricting microscale simulations to application over shallow sloping terrain. Our solution to the challenges associated with complex terrain in microscale simulations is an alternative gridding technique that does not require a terrain-following coordinate, namely the immersed boundary method (IBM). The IBM implementation in WRF used here builds on the work of Lundquist et al. (2010, 2012) and Bao et al. (2018). WRF-IBM enables the simulation of microscale flow over complex terrain, such as urban street canyons or mountains. Microscale-only urban simulations using WRF-IBM with idealized boundary conditions by Lundquist et al. (2012) have shown comparable model skill to other computational fluid dynamics (CFD) codes such as FEM3MP (Chan and Leach 2007) and QUIC-LES (Neophytou et al. 2011). Previous WRF-IBM simulations by Lundquist et al. (2012) were performed with the ghost point method (GPM) IBM algorithm. The velocity reconstruction method (VRM) IBM algorithm, which has been validated by Bao et al. (2018), is used in these multiscale simulations because it facilitates nesting of a microscale IBM domain within a mesoscale terrain-following parent domain, a functionality that was not possible with the GPM.

Over complex terrain, a nested IBM domain will use a different vertical grid than a terrain-following parent domain, which necessitates vertical interpolation during nesting (see Fig. 2.1 later). Vertical gridding in the simulations presented here is managed with the vertical grid refinement method detailed in Section 2.2 (Daniels et al. 2016; Mirocha and

Lundquist 2017). This method provides control of the grid aspect ratio and placement of vertical grid levels for each domain in a nested simulation, which Mirocha et al. (2013) found to be critical for nested large eddy simulations in WRF. The combination of vertical grid refinement and IBM enable simulations over complex terrain which capture effects across a wider range of scales than previously possible. A single simulation may now contain nested domains with grid resolutions ranging between the mesoscale (kilometers) to the microscale (meters). To the authors' best knowledge, the simulations presented here are the first to dynamically downscale from a mesoscale NWP model to a microscale urban simulation within a single NWP code.

Simulations of a continuous tracer release from the Joint Urban 2003 (JU2003) field campaign in Oklahoma City, OK (Allwine and Flaherty 2006) are used here to systematically evaluate the performance and potential benefits of the VRM algorithm and the multiscale modeling framework. Previous JU2003 studies (Chan and Leach 2007; Hanna et al. 2011; Neophytou et al. 2011; Nelson et al. 2016; García-Sánchez et al. 2018) have examined wind flow and tracer transport and dispersion using many different models including diagnostic wind flow models, Reynolds-averaged Navier-Stokes simulations, and large-eddy simulations. The simulations presented here include a multiscale configuration of five nested domains with resolutions ranging from 6.05 km to 2 m. The NCEP North American Regional Reanalysis is used for initial conditions and lateral boundary updates for the outermost domain of the multiscale simulation. Because current models cannot replicate this multiscale configuration, we validate the multiscale modeling framework developments by comparison to observations and to idealized simulations. The two idealized setups (GPM and VRM) evaluated here are similar to previous modeling efforts by Golaz et al. (2009) and Lundquist et al. (2012) with a two-domain nested setup, grid resolutions of 10 m and 2 m, periodic lateral boundary conditions on the outer domain, and a pressure gradient forcing scaled according to JU2003 observations. Configurations for the idealized and multiscale simulations are detailed in Section 2.2. Predictions of velocities and passive tracer concentration from the three simulations are compared to the JU2003 observations using several statistical measures of model skill proposed by Chang and Hanna (2004) and Calhoun et al. (2004) that are described in Section 2.4. Comparison of model skill from the idealized simulations provides insight into the benefits of a more sophisticated IBM while comparison of the idealized VRM and multiscale simulations provides insight into the benefits of downscaling using a multiscale grid-nesting approach.

2.2 Improved multiscale modeling framework

The multiscale simulations presented here rely upon use of two major improvements to the WRF model; the immersed boundary method and vertical grid refinement.

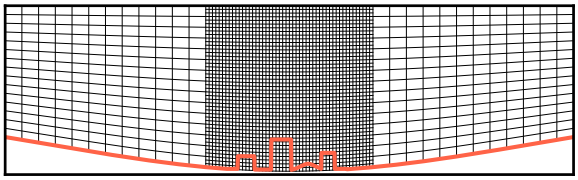

Figure 2.1: A vertical slice through a fictional nested domain with 2 grids using the VRM immersed boundary method and vertical grid refinement. The immersed boundary is shown in red.

The immersed boundary method

The immersed boundary method (IBM) is a technique for imposing the effects of a physical boundary on fluid flow. The method is especially useful for the simulation of flow over complex shapes or flexible surfaces because it does not require complicated meshing and it provides a convenient way to determine forces exerted by fluid on boundaries (Peskin 1972). IBM has the additional benefit of using a structured grid, which makes spatial discretization easier and eliminates numerical errors associated with grid transformations. Previous applications of the IBM are diverse and examples include simulations of flow over vehicles, fluid-particle interactions, and geophysical flows (Iaccarino and Verzicco 2003; Senocak et al. 2004; Mittal and Iaccarino 2005).

As simulations of environmental flows advance to higher resolutions, implementations of the immersed boundary method are increasingly common and are recently undergoing substantial research and improvement (Bao et al. 2018; Li et al. 2016). For atmospheric applications, the immersed boundary method can eliminate grid transformation errors where terrain-following coordinates are traditionally used or simplify meshing where a more traditional computational fluid dynamics model would be used with a conforming grid, such as simulations in urban terrain. Immersed boundary methods have been implemented for a variety of atmospheric simulations that notably include simulations of the Bolund Hill complex terrain test case (Jafari et al. 2012; Diebold et al. 2013; Bao et al. 2016; Ma and Liu 2017; Bao et al. 2018; DeLeon et al. 2018), flow over fractal trees (Chester et al. 2007), and urban simulations of transport and dispersion (Lundquist et al. 2012).

Figure 2.1 shows a slice through a grid with the immersed boundary (IB) shown in red. Boundary conditions are enforced at the IB through the addition of a forcing term to the governing equations. Several IBMs appear in the literature and can be categorized based upon whether the forcing term is introduced to the continuous or discretized governing equations. WRF-IBM falls within the latter category, also known as a discrete forcing approach, and includes a body force term in the conservation equations for momentum and scalars, Eq. (2.1). These body force terms are not computed directly but are instead

implicitly applied by modifying variables at grid points near the immersed boundary.

$$\partial_t \boldsymbol{V} + \boldsymbol{V} \cdot \boldsymbol{\nabla} \boldsymbol{V} = -\alpha \boldsymbol{\nabla} p + \nu_t \nabla^2 \boldsymbol{V} + \boldsymbol{g} + \boldsymbol{F_B} \tag{2.1a}$$

$$\partial_t \phi + \boldsymbol{V} \cdot \boldsymbol{\nabla} \phi = \kappa_t \nabla^2 \phi + F_\phi \tag{2.1b}$$

In Eq. (2.1a) $\boldsymbol{V}$ is the velocity vector, α the specific volume, p is pressure, $\boldsymbol{g}$ is gravitational acceleration, ν_t is turbulent viscosity, and $\boldsymbol{F_B}$ the body force term. In Eq. (2.1b) ϕ is a scalar quantity, which could represent potential temperature, moisture, or a passive tracer, κ_t is the scalar diffusivity, and F_ϕ is the additional scalar forcing. $\boldsymbol{F_B}$ and F_ϕ modify the conservation equations near the IB and assume values of zero away from the IB. The conservation equations, Eq. (2.1a) and Eq. (2.1b), are presented in a simplified form for illustrative purposes. Further information regarding the implementation of an IBM on the WRF governing equations can be found in Lundquist et al. (2010).

The immersed boundary method in WRF (WRF-IBM) has previously been used for a variety of microscale and large-eddy simulations. Lundquist (2010) developed WRF-IBM in two dimensions and coupled the IBM to a suite of atmospheric parameterizations, allowing for surface fluxes of heat and moisture at the immersed boundary. Lundquist et al. (2012) extended the method to three dimensions and simulated flow and dispersion within the central business district of Oklahoma City, OK. Arthur et al. (2018a) enabled topographic shading at immersed boundaries and evaluated the development of thermally driven downslope flow on an isolated mountain during the MATERHORN field campaign. Bao et al. (2018) implemented a surface stress parameterization at the IB and compared simulations to observations from the Askervein and Bolund field experiments. Each of these previous simulations used idealized initial conditions and forcing at lateral boundaries, preventing representation of time-varying weather effects on these smaller scale simulations.

In previous applications of WRF-IBM, idealized initial conditions and lateral boundary conditions were used because domains using the immersed boundary method could not easily be nested within those using WRF's native terrain-following coordinate. This was due to the ghost point method (GPM) IBM algorithm requiring computational grid points below the immersed boundary. These additional grid points introduce a discontinuity in grid heights at the interface between nested terrain-following and GPM domains, which is incompatible with the WRF model equations. The velocity reconstruction method (VRM) is an alternative to the GPM that does not require grid points beneath the IB, which greatly simplifies the nesting of a domain using VRM within a terrain-following parent grid. WRF-IBM uses a non-conforming structured grid that can optionally be independent of the IB or, if using VRM, the grid may optionally and selectively align with the IB. An example grid, shown in Figure 2.1, illustrates the approach used in these multiscale modeling efforts using VRM where the grid is allowed to conform to the underlying ground topography while complex features, such as buildings, are represented by the immersed boundary.

Ghost point method

The ghost point method (GPM) enforces desired boundary conditions by applying forcing at computational nodes considered to be within the "solid" portion of the domain. Nodes where forcing is applied are referred to as "ghost points". The procedure to modify each ghost point begins by reflecting the ghost point across the immersed boundary, which creates an "image point". The image point's magnitude is calculated based upon the magnitudes of nearby computational nodes using an interpolation scheme, which in this case is the inverse distance weighting (IDW) scheme, the details of which are discussed later in this section. An example illustrating this procedure is shown in Figure 2.2a. The magnitude of ϕ at a ghost point is then determined using Eq. (2.2a) for a Dirichlet boundary condition or Eq. (2.2b) for a Neumann boundary condition.

$$\phi_G = 2\phi_\Omega - \phi_I \tag{2.2a}$$

$$\phi_G = \phi_I - \overline{GI}\frac{\partial \phi}{\partial \boldsymbol{n}}|_\Omega \tag{2.2b}$$

where ϕ_G is the value at the ghost point, ϕ_I is the value at the image point, and ϕ_Ω is the value at the IB. $\overline{GI}$ is the distance between the ghost and image points and $\frac{\partial \phi}{\partial \boldsymbol{n}}|_\Omega$ is the surface-normal gradient value assigned at the IB for a Neumann boundary condition. For the simulations presented here using the GPM, a no-slip boundary condition is applied to velocities.

Because the GPM requires ghost points and at least two vertical grid levels positioned beneath the IB, the grid's bottom level is lowered relative to a WRF grid using terrain-following coordinates. This mismatch complicates nesting between terrain-following and GPM domains because it creates a discontinuity in domain height across the nest interface. For this reason, we have modified another WRF-IBM algorithm, the velocity reconstruction method first introduced by Bao et al. (2018) and described below, which is suited to our needs for multiscale modeling because it does not require ghost points, and thus is capable of being used on a domain nested within a parent domain using terrain-following coordinates. Additionally, Bao et al. (2018) found improved model performance when using IBM algorithms that use log-law boundary conditions, such as the velocity reconstruction method.

Velocity reconstruction method

The velocity reconstruction method (VRM) follows a similar approach to that of Senocak et al. (2004), where a log-law boundary condition at the IB is enforced by applying forcing at the computational nodes in the fluid domain that are adjacent to the immersed boundary, which are referred to here as "reconstruction points" (RP). Extensive validation of the VRM in WRF-IBM was performed by Bao et al. (2018), which includes simulation of flow over flat terrain, idealized hills, Askervein Hill in Scotland, and Bolund Hill in Denmark.

Boundary conditions at the IB are enforced by modification of each RP according to the following procedure, an example of which is illustrated in Figure 2.2b. First, a vector is

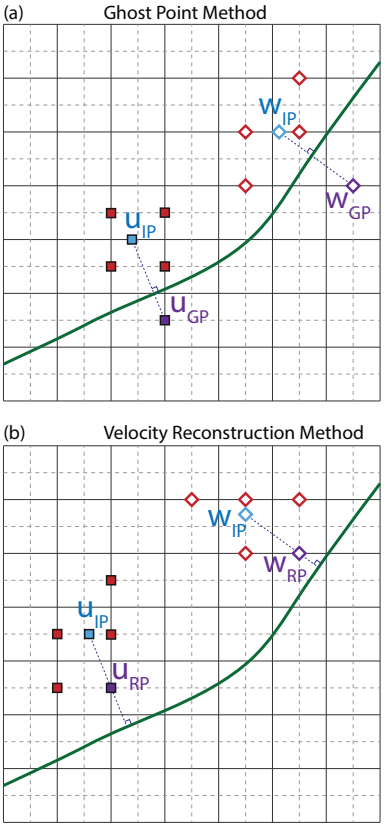

Figure 2.2: Two dimensional examples of point selection by the (a) GPM and (b) VRM algorithms. The immersed boundary is shown in green, reconstruction points (VRM) and ghost points (GPM) in purple, interpolation points (VRM) and image points (GPM) in blue, and nearest neighbors in red. The solid and dashed gray lines represent the Arakawa-C staggered grid used by WRF, with mass points located at the intersections of the dashed lines.

calculated that connects the RP and the nearest section of the IB. The "interpolation point" (IP) is then located by projecting away from the IB along this vector until reaching a cell face. u, v, and w velocities at the IP are calculated using the inverse distance weighting interpolation scheme described later in this section. The coordinate orientation at the IP is then rotated to be surface normal to the IB, aligning with the vector used earlier. The log-law for flow over a rough surface, Eq. (2.3) as written by Panofsky and Dutton (1984), is then used to relate velocities at the IP and RP.

$$U = \frac{u_*}{\kappa} \ln\left(\frac{z}{z_0}\right) \tag{2.3}$$

Here z is the surface normal distance from the IB, z_0 is the roughness height, u_* is the friction

velocity, κ is the Von Karman constant, and U is the magnitude of the velocity. It should be noted that relating the IP and RP using Eq. (2.3) assumes that the friction velocity is constant in the surface normal direction within the region that contains both the IP and RP. With this assumption the relationship between the IP and RP can be represented as follows, where d_{RP} and d_{IP} are the surface normal distances between the IB and the RP or IP.

$$U_{RP} = U_{IP} \frac{\ln\left(\frac{d_{RP}}{z_0}\right)}{\ln\left(\frac{d_{IP}}{z_0}\right)} \tag{2.4a}$$

w_{RP} is calculated by assuming $w = 0$ at the IB and a linear relationship of w with d, which yields

$$w_{RP} = w_{IP} \, \frac{d_{RP}}{d_{IP}} \tag{2.4b}$$

U_{RP} is then separated into u and v velocities, where θ is the horizontal wind direction defined using geographic convention.

$$\theta = \arctan\left(\frac{u_{IP}}{v_{IP}}\right) \tag{2.5a}$$

$$u_{RP} = U_{RP} \, \sin\theta, \quad v_{RP} = U_{RP} \, \cos\theta \tag{2.5b}$$

Finally, the u, v, and w velocities at the RP are rotated from being surface-normal to the IB back to the coordinate orientation of the grid.

Inverse distance weighting interpolation scheme

The IDW interpolation scheme is used to determine values for image and interpolation points when using GPM and VRM, respectively. First, the nearest neighboring grid points to the image/interpolation point are located by searching a box of grid points centered on the image/interpolation point. The simulations presented here search for nearest neighbors within either a $4 \times 4 \times 4$ or $6 \times 6 \times 6$ box of grid points for simulations using the GPM or the VRM, respectively. Each point in searched region is ranked based upon distance from the image/interpolation point. Points beneath the IB are removed from consideration. For the VRM, reconstruction points are also removed from consideration. The nearest n points are used as the nearest neighbors to the image/interpolation point, where $n = 8$ for the GPM and $n = 7$ for the VRM. Image/interpolation points will occasionally have fewer than n valid nearest neighbors, especially if the point is located over extremely complex terrain. The simulations presented below have been configured such that all image/interpolation points have at least two valid nearest neighbors.

The value at each image/interpolation point, φ, is calculated using Eq. (2.6a), which is a weighted average of the nearest neighbors to the image/interpolation point. Weights of nearest neighbors are calculated using Eq. (2.6b) where r_{max} is the maximum distance between a nearest neighbor and the image/interpolation point, and W_i is the weight of the i^{th} nearest neighbor, which is a distance r_i from the image/interpolation point. Image/interpolation

point locations, nearest neighbors, and weights are recalculated at each time step to avoid complications that may arise if the WRF grid point heights shift during runtime due to the model's mass-based vertical coordinate.

$$\varphi = \frac{\sum_{i=1}^{n} W_i \varphi_i}{\sum_{i=1}^{n} W_i} \tag{2.6a}$$

$$W_i = \left(\frac{r_{max} - r_i}{r_{max} r_i} \right)^{\frac{1}{2}} \tag{2.6b}$$

Vertical grid refinement

A key feature required for multiscale simulations is vertical refinement of nested domains. Prior to WRF version 3.8.1, the only available method of vertical grid refinement was ndown, a separate program that ingests parent grid output files and generates boundary updates for a nest. Because ndown processes output files, the parent simulation must be run to completion before the nested simulation can be run. Additionally, the boundary update frequency is limited to that of the parent grid output, which can prohibit downscaling of resolved turbulent flows.

We previously developed an improved vertical grid refinement method that has been included within the WRF public release since version 3.8.1 (Daniels et al. 2016) and is used here in version 3.6.1. This capability allows for nested domains with different vertical grids to be run concurrently without requiring a separate program like ndown. The lateral boundary conditions of a nest are updated at every time step using an interpolation between bracketing time steps from the corresponding parent. We have also included the ability to specify unique vertical grid levels for every domain in a sequence of nested grids. Additional details regarding the capabilities, implementation, and validation of the vertical nesting framework can be found in Daniels et al. (2016).

The vertical grid refinement capability is a critical component of the multiscale modeling framework described here. The ability to refine vertically provides control over each domain's grid aspect ratio ($\Delta x/\Delta z$), an important variable for accurate large-eddy simulations (Mirocha et al. 2013; Mirocha and Lundquist 2017). It should be noted that our multiscale simulation, detailed in Section 2.3, successfully applies the vertical grid refinement method to a sequence of five nested grids, a considerably more complex configuration than simulations from Daniels et al. (2016).

2.3 Simulations for Joint Urban 2003 dispersion study

During July of 2003, the Defense Threat Reduction Agency (DTRA) and the U.S. Department of Homeland Security (DHS) worked together to facilitate the Joint Urban 2003 (JU2003) atmospheric dispersion study in Oklahoma City, Oklahoma. Investigators from

universities, government laboratories, and private industry participated in the field campaign and analysis. Some of the primary objectives of this field campaign included the investigation of flows downwind of tall buildings and in street canyons and the investigation of tracer dispersion around and downwind of tall buildings. More details can be found in the study overview (Allwine and Flaherty 2006).

Joint Urban 2003 consisted of ten intensive observational periods (IOPs), each with 8 hours duration, throughout the 34 day span of the field campaign. A tracer gas, sulfur hexafluoride (SF_6), was released during each IOP as either a puff or continuous release. Meteorological conditions and tracer concentrations were measured at sites throughout the central business district. The locations of the SF_6 release site and the instruments used in this analysis are displayed in Figure 2.3. Observations from several instruments have been used for configuration and analysis of the simulations presented here, including a miniSODAR deployed by Argonne National Laboratory (ANL), 11 Dugway Proving Ground (DPG) Portable Weather Information Display Systems (PWIDS) with prop-vane anemometers, 15 DPG super PWIDS with sonic anemometers, 19 Lawrence Livermore National Laboratory (LLNL) "bluebox" integrating gas samplers, and 25 NOAA Air Resources Laboratory Field Research Division (ARL FRD) programmable integrating gas samplers (PIGS).

The simulations and analysis presented in this paper are limited to the first continuous tracer release of IOP 3 from 16:00 to 16:30 UTC 7 July 2003. During IOP 3 the SF_6 release location was at the north-east corner of the botanical gardens at 2 m above ground level (AGL) and Universal Transverse Mercator (UTM) coordinates (634603, 3925763), marked by the yellow star in Figure 2.3. This particular tracer release was selected for analysis because it was previously simulated in Chan and Leach (2007) and Lundquist et al. (2012), and therefore there are previous modeling studies to which we can compare our results. IOP 3 was selected for these previous studies because the wind direction was consistent over the 30 minute release period and the atmospheric stability was near neutral, which are benefits when using idealized lateral boundary conditions or a computational fluid dynamics model without atmospheric stability effects. While these attributes are beneficial for our idealized simulations, our multiscale simulation is capable of simulating a case with shifting wind conditions and non-neutral atmospheric stability. Demonstration of this ability will be the subject of future work.

Simulations are configured to enable comparisons between the GPM and VRM IBM algorithms as well as the idealized and multiscale configurations. Three simulations are analyzed here; two idealized configurations and one multiscale configuration. In the two idealized simulations, the GPM and VRM IBM algorithms are used, which builds on the work presented in Lundquist et al. (2012), where the GPM IBM algorithm was used in an idealized simulation of JU2003 IOP 3. Although the VRM algorithm was validated in Bao et al. (2018), its use here is presented as validation for urban applications, and allows for the quantification of differences between the GPM and VRM algorithms. The multiscale configuration is then presented, which uses both terrain-following grids and the VRM-IBM. Comparisons between the idealized and multiscale simulations provide insight into the performance of the multiscale setup.

Idealized configuration

The idealized simulations are configured similar to previous JU2003 modeling efforts at building-resolving scales which used simplified boundary conditions and forcing scaled to generate agreement with observations. Reynolds-averaged Navier-Stokes (RANS) simulations by Chan and Leach (2007), Chow et al. (2008), along with both the RANS and LES simulations by Neophytou et al. (2011) used inflow boundary conditions based upon steady velocity profiles constructed by fitting a log law profile to SODAR and weather station observations. The idealized simulations presented here adopt a similar configuration to simulations by Golaz et al. (2009) using the COAMPS-LES model and WRF-IBM simulations by Lundquist et al. (2012) and Bao et al. (2018) that use a two-domain nested configuration to produce turbulent inflow for the nested domain. This configuration simulates only the microscale and both domains use the 3D Smagorinsky turbulence closure. The parent domain uses periodic boundary conditions and a pressure gradient forcing term is applied to achieve agreement between the simulated and observed time-averaged velocity profiles. Figure 2.4 shows the grid layout for the idealized simulations.

Vertical grid refinement was used to maintain a near surface grid aspect ratio $\Delta x/\Delta z = 2.0$ for each domain. Aloft, the vertical grid levels are spaced increasingly far apart with a constant stretching coefficient, $(z_{k+1} - z_k) \,/\, (z_k - z_{k-1})$, of 1.016 for D1 and 1.028 for D2. Upon reaching $\Delta x/\Delta z = 0.5$ the grid aspect ratio is maintained for the remaining vertical grid levels. The coarsening of vertical resolution aloft was used to reduce computational costs without sacrificing high-resolution and grid quality in the region of interest (near surface). Due to the need for ghost points beneath each point of the immersed boundary, the WRF-IBM-GPM simulations have two additional levels located approximately 2 m and 4 m beneath the ground level.

Our idealized WRF-IBM simulations use a two-domain setup with a periodic parent domain (D1) at $\Delta x = \Delta y = 10$ m and a nested domain (D2) at $\Delta x = \Delta y = 2$ m, with a grid refinement ratio of 5. The domains use time steps of 0.05 s for D1 and 0.01 s for D2. In the east-west, north-south, and bottom-top dimensions, D1 has dimensions $241 \times 241 \times 146$ grid points and D2 has dimensions $351 \times 401 \times 243$ grid points. D1 has flat terrain while D2 includes building geometries. Both domains use a Smagorinsky turbulence closure with coefficient $C_s = 0.18$. D1 was run for seven hours to develop statistically steady turbulence prior to initialization of D2. D2 was initialized prior to the tracer release by 10 minutes, roughly twice the time required to traverse the domain at 3 m s^{-1} and a sufficient amount of time for the flow to fully develop around the complex urban terrain.

The idealized GPM and VRM simulations are forced by a uniform pressure gradient which is adjusted to generate agreement between the time-averaged velocity profile from D2 and the time-averaged miniSODAR observations at approximately 40 m AGL, shown in Figure 2.5. Both domains have a model top at 400 m AGL and a Rayleigh relaxation layer applied to W velocities within the top 40 m with a damping coefficient of 0.2 s^{-1}.

The observed velocity profile used for our idealized WRF-IBM simulations is the combination of data from several closely located instruments that measure at different heights. A

similar methodology for inflow profile generation was also used by Hanna et al. (2011) and Lundquist et al. (2012). The instruments used here include an ANL miniSODAR, two DPG PWIDS (P10 and P11), two DPG super PWIDS (SP17 and SP20), and the NOAA ARL FRD sonic anemometer located at the SF_6 release location. The ANL miniSODAR data from the 30 minute SF_6 release window was temporally averaged to provide velocities at 5 m increments from 15 to 135 m AGL, shown in Figure 2.5. Each of the DPG PWIDS (P10 and P11) and DPG super PWIDS (SP17 and SP20) was temporally averaged over the SF_6 release window. An average of these four stations, with each station given equal weight, was used as an estimate of velocities at 8 m AGL. Additionally, an ARL FRD sonic anemometer collocated with the SF_6 release site was similarly temporally averaged to provide an estimate of velocities at 2 m AGL.

The GPM simulation uses a no-slip bottom boundary condition for velocities and the VRM simulation uses the log-law boundary condition with roughness length $z_0 = 0.1$ m. Both GPM and VRM simulations use the traditional WRF boundary condition for scalar variables, which is a no-flux condition applied at the model bottom. No treatment is applied for scalars at the IB (i.e. building surfaces), however this has minimal effect on our results because the wind fields prevent advection of scalars through the IB and diffusion of scalar across the IB is negligible. A scalar immersed boundary condition exists for the GPM but was not used to maintain similarity between the GPM and VRM configurations. A scalar immersed boundary condition that does not require ghost points is currently under development for use with the VRM.

Multiscale configuration

The multiscale WRF-IBM simulation uses five nested domains with horizontal resolutions of 6.05 km, 550 m, 50 m, 10 m and 2 m. Resolutions are selected to optimize computational resources, while properly resolving flow features at scales of interest. Horizontal dimensions of the 10 m and 2 m domains are identical to the dimensions of the corresponding domains in the idealized simulations. Because the predominant wind direction (SSW) is known, the 10 m and 2 m domains are positioned in the northeast quadrant of their respective parent domains. This offset increases the fetch prior to inflow boundaries, which promotes the development of turbulence without increasing the domain extents and computational costs. The multiscale grid layout is depicted in Figure 2.6. The five domains are initialized in a cascading fashion with start times of 03:00, 06:00, 12:00, 15:00, and 15:50 UTC. Conditions on the 2 m domain are saved every two seconds during the release window between 16:00 and 16:30 UTC. Ideally, studies would be conducted to evaluate the optimal number of nests, grid refinement ratios, the necessary spatial extents of each domain, and domain start times, however the computational costs of such studies currently exceed available resources.

Lateral boundary conditions and initial conditions for the outermost 6.05 km domain are prescribed using data from the NCEP North American Regional Reanalysis (Mesinger et al. 2006), which has horizontal resolution of 32 km. The VRM IBM algorithm is used on the 10 m and 2 m domains while the standard WRF terrain-following coordinate is used on the

Table 2.1: Multiscale model configuration for JU2003 simulations. TF = terrain-following coordinate. KF = Kain-Fritsch cumulus parameterization. Smag = 3D Smagorinsky Turbulence Closure.

	D1	D2	D3	D4	D5
Δx & Δy [m]	6050	550	50	10	2
coordinate	TF	TF	TF	IBM	IBM
time-step [s]	30	3	0.25	0.05	0.01
east-west grid points	221	232	254	241	351
south-north grid points	221	232	254	241	401
bottom-top grid points	51	51	76	146	243
turbulence	MYJ	MYJ	Smag	Smag	Smag
micro-physics	WSM3	WSM3	WSM3	none	none
longwave radiation	RRTM	RRTM	RRTM	none	none
shortwave radiation	Dudhia	Dudhia	Dudhia	none	none
surface layer scheme	MM5	MM5	MM5	none	none
land surface model	Noah	Noah	Noah	none	none
cumulus parameterization	KF	KF	none	none	none

6.05 km, 550 m, and 50 m domains. Domains run with the VRM use a constant roughness length of $z_0 = 0.1$ m. The 6.05 km and 550 m domains use the Mellor-Yamada-Janjić planetary boundary layer scheme (Mellor and Yamada 1982; Janjić 2002) while the 50 m, 10 m and 2 m domains use the 3D Smagorinsky turbulence closure scheme with $C_s = 0.18$. A summary of grid configuration and physics options is included in Table 2.1.

A model top of 200 hPa is used for all domains of the multiscale simulation. Near surface vertical grid levels for the multiscale 10 m and 2 m domains are selected to match, as closely as possible, those used in the comparable domains of the idealized simulations. Above the model top of the idealized simulations (400 m AGL), vertical grid levels stretch in height at a constant rate of $(z_{k+1} - z_k) / (z_k - z_{k-1}) = 1.05$. This greatly reduces the number of grid points, and correspondingly the computational costs, of the microscale domains while maintaining an optimal grid aspect ratio near the surface in the region of interest.

Urban geometry

Urban geometry represented by the immersed boundary was created by sampling, at each grid point, a shapefile containing vectorized building information. Narrow gaps between buildings and other insufficiently resolved features were manually adjusted to ensure that each of the VRM interpolation points had a minimum of two nearest neighbors for the inverse distance weighting interpolation. WRF-IBM currently uses a two-dimensional array to store the immersed boundary height at each grid point, which restricts the model

topography to solid shapes without void space. Due to this restriction, an elevated walkway at UTM coordinates (634850, 3925800) was omitted from the model topography because WRF-IBM is currently unable to resolve flow in the free space beneath the suspended structure. Additionally, several buildings near inflow boundaries, specifically the southern edge, were removed due to spurious interactions with the inflow conditions. Nonphysical behavior around buildings near the inflow boundaries of the 2 m domain is not unexpected as these buildings are not represented on the 10 m parent domain and the flow on the parent domain is unobstructed. Identical building geometry representations were used for both the idealized and multiscale simulations.

Variations in the ground elevation within the microscale modeling domain are small in magnitude, with minimum and maximum elevations of 360 and 365 m ASL. Due to restrictions from periodic boundary conditions, the idealized simulations ignore the underlying ground topography and only building heights above ground level are included in the immersed boundary height. An advantage of the multiscale simulation, in contrast, is that no periodic boundary conditions are used and the underlying ground topography can be included. For the multiscale simulation, the building heights above ground level are combined with the underlying ground topography interpolated from the parent domain. To maintain flat rooftops, the IB height is averaged at points within each building footprint, which results in minor adjustments within each building geometry.

2.4 Simulation results and discussion

The WRF-IBM simulations illustrate the complex behavior of atmospheric flows within urban environments. Both the idealized and multiscale simulations display channeling effects in street canyons and many other microscale flow features including separation zones, return flows, and recirculation in the lee of buildings. Contours of instantaneous wind speed, Figure 2.7, illustrate many of these intricacies seen in all three simulations. The analysis presented below includes qualitative comparisons of observations and simulation results of wind speed, direction, and SF_6 concentration that have been time-averaged over the SF_6 release period. Additionally, quantitative analysis is performed using measures of model skill to evaluate the accuracy of various model configurations in predicting winds and SF_6 concentrations compared to observations.

During IOP 3, the ANL miniSODAR was located within the botanical gardens and sampled flow that was relatively unobstructed upstream. Figure 2.5 compares time-averaged vertical profiles of horizontal wind speed and direction from the simulations to the time-averaged miniSODAR measurements. Both idealized simulations (GPM and VRM) overestimate the horizontal wind speed, sometimes by up to 2.5 m s^{-1}, in the region between ground level and approximately 40 m AGL, despite tuning the pressure gradient to match the observations at 40 m AGL. The multiscale simulation, which does not include *a priori* knowledge of the JU2003 observations (i.e. tuning), shows improved agreement between 5 and 30 m AGL and 100 to 140 m AGL with an overestimation from the surface until 100 m AGL. Unlike the

idealized simulations, the multiscale simulation produces a profile with similar shape to that seen from the miniSODAR, possibly due to the large-scale flow features downscaled from the mesoscale domains. All of the simulations show excellent agreement with the measured wind direction. This agreement is expected in the idealized simulations because the pressure gradient forcing is tuned to generate agreement with the observations, but the multiscale model has no such tuning and yet shows comparable agreement to the observed wind direction.

A possible explanation for the overestimation of the near surface wind speed in all three simulations is the omission of terrain-features upstream of the miniSODAR. To test this theory, the multiscale simulation was run a second time with roughness elements added to D4, the 10 m domain. Ideally we would add the actual building geometries to the 10 m domain; however, the great majority of structures within the 10 m domain have too few grid points per building to be properly resolved. According to Tseng et al. (2006), a minimum of six to eight grid points is necessary across a bluff body to achieve reasonable results when using an IBM in a LES. For this reason, we have instead used a regular pattern of large roughness elements to represent the urban terrain. These elements have footprints of 80×80 m and are 10 m in height with the element center-points described by an array with 320 m spacing and 30ffset between rows to roughly align with the predominant wind direction. Figure 2.8 shows the immersed boundary height on the 10 m domain (D4) of this modified multiscale simulation.

Figure 2.5 shows that the addition of these roughness elements to the 10 m domain resulted in noticeably improved agreement between the 2 m domain (D5) and the observed near-surface wind speed profile, particularly between 15 and 40 m AGL. If future computational resources allow, the 2 m domain could be extended southward to provide additional fetch and resolve flow around more buildings upstream from the miniSODAR and the SF_6 release location. Another solution could be to add artificial drag at grid points that fall within poorly resolved terrain features. While these modifications could potentially yield improvements, the current simulation configurations are sufficient for the focus of this paper, which is analyzing the performance and benefits of the multiscale configuration. Investigation and analysis of treatments for poorly resolved terrain features will be the focus of future research as it appears to be of importance for improving future multiscale models.

A quantitative analysis of model skill is discussed below, however visual comparison of model results to time-averaged wind speed/direction from DPG PWIDS (P) and super PWIDS (SP), shown in Figure 2.9, indicate that all three simulations have similar behavior to observations within the street canyons, in the lee of buildings, and on rooftops. Importantly, all three simulations agree reasonably well with P11 and SP17, which are collocated at the SF_6 release location.

Figure 2.10 shows time series of horizontal wind speed and wind direction at 8 m AGL above the SF_6 release location. All simulations, idealized and multiscale, display similar behavior of the time-averaged horizontal wind speed, but differences between simulations are clearly visible in the timeseries of wind direction. Fluctuations in wind direction from the idealized GPM and idealized VRM simulations are of lower magnitude than those in the multiscale simulation, which includes larger deviations from the mean wind direction and

lower frequency variations. These characteristics indicate the presence of large-scale features from the coarse resolution parent domains transitioning into the 2 m domain of the multiscale simulation. The effects of increased meandering of the flow in the multiscale simulation are evident in Figure 2.11 where the time-averaged plume of the idealized VRM simulation is considerably more spatially constrained compared to that from the multiscale simulation. As hypothesized by Nelson et al. (2016), our multiscale simulation appears to reproduce some of the transient flow interactions within the urban topography that are driven by oscillations in the prevailing wind direction.

Quantitative performance measurements of the simulations compared to JU2003 observations are calculated using methods suggested by Chang and Hanna (2004): fraction of predictions within a factor of x (FACx); fractional bias (FB); geometric mean bias (MG); geometric variance (VG); and normalized mean squared error (NMSE). Differences in wind direction are evaluated using the scaled average angle (SAA) skill test devised by Calhoun et al. (2004). Combinations of these performance metrics have previously been applied to Joint Urban 2003 simulations by Chan and Leach (2007) and Chow et al. (2008) using the FEM3MP model, Hanna et al. (2011) when comparing four diagnostic urban wind flow models with Lagrangian particle dispersion models, and by Lundquist et al. (2012) using the WRF-IBM-GPM model.

$$\begin{aligned}
\text{FACx} =& \text{fraction of data that satisfies...} \\
& \ldots\ 1/x \leq X_p/X_o \leq x && \text{(2.7a)} \\
\text{FB} =& 2\left(\overline{X_o} - \overline{X_p}\right) / \left(\overline{X_o} + \overline{X_p}\right) && \text{(2.7b)} \\
\text{MG} =& \exp\left(\overline{\ln\left(X_o\right)} - \overline{\ln\left(X_p\right)}\right) && \text{(2.7c)} \\
\text{VG} =& \exp\left(\overline{\left(\ln\left(X_o\right) - \ln\left(X_p\right)\right)^2}\right) && \text{(2.7d)} \\
\text{NMSE} =& \overline{\left(X_o - X_p\right)^2} / \left(\overline{X_o}\ \overline{X_p}\right) && \text{(2.7e)} \\
\text{SAA} =& \Sigma\left(|U_i||\phi_i|\right) / \left(N|\overline{U_i}|\right) && \text{(2.7f)}
\end{aligned}$$

In the above equations, X_o is the set of observational data and X_p are the corresponding predictions from the simulation, N is the number of observations, ϕ_i is the difference between observed and predicted wind directions, and $|U_i|$ is the predicted wind speed. Here we use values for X_o and X_p that are time-averages over the 30 minute release period. An overbar indicates averaging of all locations.

The methods above are chosen to provide a broad analysis of model performance. FACx, MG, and FB provide insight into the systematic bias of the predictions. NMSE and VG provide insight into the scatter of the data and indicate whether there is agreement between the distributions of predictions and observations. Some skill metrics, such as FB and NMSE, are more heavily influenced by data points with large magnitudes versus small, which is fine for variables such as wind speed that do not vary over many orders of magnitude. The time-averaged observed and predicted SF_6 concentrations span several orders of magnitude (0.001 to 100 ppbv), so the logarithmic forms of mean bias and variance, MG and VG, are

more appropriate for analysis of SF_6 concentrations as these metrics evenly weigh the under and over predictions (Hanna et al. 1993).

Concentration floors are applied to the LLNL "bluebox" samplers and the NOAA ARL FRD PIGS because each dataset has a minimum concentration that could be accurately measured due to errors from the instruments and analysis procedures. Additionally, several of the skill test calculations are mathematically valid only for predictions and observations that are nonzero. PIGS data points of SF_6 concentration less than the method limit of detection (MLOD) have a quality control flag. Flagged PIGS data points are modified to 1 pptv, which corresponds to half of the minimum analyzed concentration used during calibration. Instrument limit of detection and MLOD are not available from the LLNL "bluebox" samplers. A 5 pptv floor to the LLNL "bluebox" concentrations is introduced by modifying data points that are below the lowest reference concentration from the calibration curves of the gas chromatograph used to analyze the samples, 9.3 pptv. To maintain consistency, the concentration floors are also applied to the predicted time-averaged station concentrations.

Graphical representations of model skill for predicting wind speed/direction and concentration are shown in Figure 2.12. The simulations display excellent FAC2 scores for predicting horizontal wind speed with all three simulations reporting a score of 0.91 compared to PWIDS and the lowest score compared to Super PWIDS being an impressively high value of 0.73. Despite at least one of the idealized simulations matching or slightly outperforming the multiscale simulation in every wind speed/direction skill test, it is important to remember that both idealized simulations (GPM and VRM) were provided with an initialization constructed using JU2003 observations. Additionally, the pressure gradient forcing used for the idealized simulations was tuned to maintain agreement with miniSODAR velocity profile observations. While the idealized simulations rely upon *a priori* knowledge of the local meteorology, the multiscale simulation is run as a forecast and uses initial conditions and forcing that are independent of the JU2003 observations and are provided by external datasets, as is typical in mesoscale forecasting. Thus, the agreement of the multiscale simulation with observations of wind speeds/directions and SF_6 concentrations is quite remarkable considering the absence of model tuning.

Eq. (2.7b) can be rearranged to yield Eq. (2.8), from which it becomes clear that the negative fractional bias scores in Figure 2.12 indicate that all three models are slightly overestimating wind speeds compared to both PWIDS and super PWIDS.

$$\frac{\overline{X_p}}{\overline{X_o}} = \frac{1 - \frac{1}{2}\mathrm{FB}}{1 + \frac{1}{2}\mathrm{FB}} \tag{2.8}$$

The idealized VRM simulation shows the least overestimation of wind speeds with FB scores of -0.05 (PWIDS) and -0.09 (super PWIDS), which implies overprediction by factors of 1.05 and 1.09. FB scores from the idealized GPM and multiscale simulations are clustered around -0.25±0.01, which roughly corresponds to a factor of 1.29 overprediction. Earlier, when evaluating the vertical profiles of wind speed, it was suggested that the omission of terrain-features could be responsible for the overestimation of the near surface wind speed. The negative

FB scores are another indication that the simulations presented here are missing some important small-scale features of the terrain that would produce additional drag and slow the near-surface winds. When compared to the idealized GPM simulation, the improved FB score of the idealized VRM simulation indicates that the log-law bottom boundary condition used by the VRM yields less bias in the magnitude of wind speeds than the no-slip bottom boundary condition used by the GPM. Drawing conclusions about the multiscale simulation from the differences in FB scores is complicated by variations in the idealized and multiscale model configurations, such as the lateral boundary conditions and forcing methods.

Skill tests evaluating the prediction of SF_6 concentrations, displayed in the second row of Figure 2.12, show the multiscale simulation produced the highest model skill followed by the idealized VRM simulation, which outperformed the idealized GPM simulation. For each simulation, the FAC5 agreement with the bluebox samplers is higher than that of the FRD samplers, likely because of the FRD samplers being sited further downwind from the release location. FAC5 comparing to the bluebox samplers was 0.68, 0.74, and 0.95 for the idealized GPM, idealized VRM, and multiscale simulations respectively and 0.44, 0.56, and 0.64 compared to the FRD samplers. The multiscale simulation's exceptional skill test results show that we can achieve admirable predictions of urban dispersion by appropriately downscaling mesoscale forecasts to force microscale simulations.

Both the idealized and multiscale simulations display model skill that exceeds the minimum performance for an acceptable model as noted in many previous studies, such as Chang and Hanna (2004) and Tewari et al. (2010). These standards include greater than 50% of predictions within a factor of two (FAC2 ≥ 0.5) and less than 30% mean bias ($0.7 \leq \text{MG} \leq 1.3$). Compared to previous microscale simulations of transport and dispersion during JU2003, (Chan and Leach 2007; Hanna et al. 2011; Lundquist et al. 2012; Li et al. 2018), the model skill of the multiscale simulation for prediction of SF_6 concentrations is exceptional, with FAC2 / FAC5 scores of 0.58 / 0.95 and 0.56 / 0.76 compared to the bluebox and FRD samplers, respectively. The simulation of transport and dispersion during IOP 3 by Li et al. (2018), which used coupled mesoscale and microscale models, offers an excellent comparison to the multiscale model presented here and produced FAC2 / FAC5 of 0.37 / 0.84 compared to the bluebox samplers. The favorable FAC2 / FAC5 scores of the multiscale simulation indicate that transport and dispersion models can obtain substantial improvements in model skill by dynamically downscaling meteorological fields from the mesoscale to microscale.

2.5 Summary and conclusions

The expansion of WRF's multiscale framework presented here enables simulations over complex terrain with resolutions ranging from the mesoscale to the microscale and forcing supplied by an operational forecast. The velocity reconstruction method (VRM) immersed boundary method (IBM) algorithm is designed such that a domain run with VRM can be nested within a terrain-following parent domain. Using VRM, microscale domains can accurately simulate flow over complex terrain, such as dense urban environments. The

vertical grid refinement functionality of Daniels et al. (2016) facilitates transitioning from terrain-following domains in the mesoscale to IBM domains in the microscale. The vertical refinement method also enables control over the grid aspect ratio of each domain in a sequence of nests, which is critical for producing high quality simulations across a range of scales.

The performance of the multiscale model was evaluated here by comparison to idealized simulations of a continuous tracer release from IOP 3 of the Joint Urban 2003 (JU2003) field experiment in Oklahoma City, OK. The idealized simulations use a two-domain nested configuration with resolutions of 10 m and 2 m, periodic lateral boundary conditions (parent domain only), simplified terrain, and forcing based upon local measurements taken during JU2003. Two idealized simulations were also analyzed, one using the ghost point method IBM algorithm of Lundquist et al. (2012) and another using the VRM. The idealized simulations share many features with configurations of previous JU2003 modeling efforts by Chan and Leach (2007), Neophytou et al. (2011), and Lundquist et al. (2012). The multiscale simulation consisted of five nested domains with horizontal resolutions of 6.05 km, 550 m, 50 m, 10 m, and 2 m. Initial conditions and boundary conditions were supplied by the NCEP North American Regional Reanalysis dataset. Unlike the idealized simulations, the multiscale simulation did not use large scale forcing parameters dependent on observations from the JU2003 field experiment. Terrain-following coordinates were used on the 6.05 km, 550 m, and 50 m domains and VRM was used for the 10 m and 2 m domains.

Evaluation of the three simulations included a suite of statistical measurements of model skill for the prediction of wind speeds and SF_6 concentrations, as suggested by Chang and Hanna (2004). All three simulations displayed excellent skill at predicting wind speeds/directions, including the multiscale simulation, which was run in a forecasting mode. For prediction of SF_6 concentrations, the multiscale simulation outperformed the idealized simulations by displaying the highest skill in nine out of the ten metrics calculated. These impressive skill scores may be a result of increased plume meandering caused by downscaled motions with scales larger than those produced in the idealized simulations. The high level of skill shown by the multiscale simulation implies that microscale simulations over complex terrain, especially transport and dispersion simulations, may greatly benefit from downscaled meteorology.

Future studies of the multiscale modeling framework will focus on the development and quantification of turbulence and the impacts of improved representation of land surface heterogeneity at resolutions between the mesoscale and microscale. Additionally, these studies will evaluate the multiscale modeling framework's applicability to non-neutral atmospheric conditions, such as those observed during nighttime IOPs of JU2003.

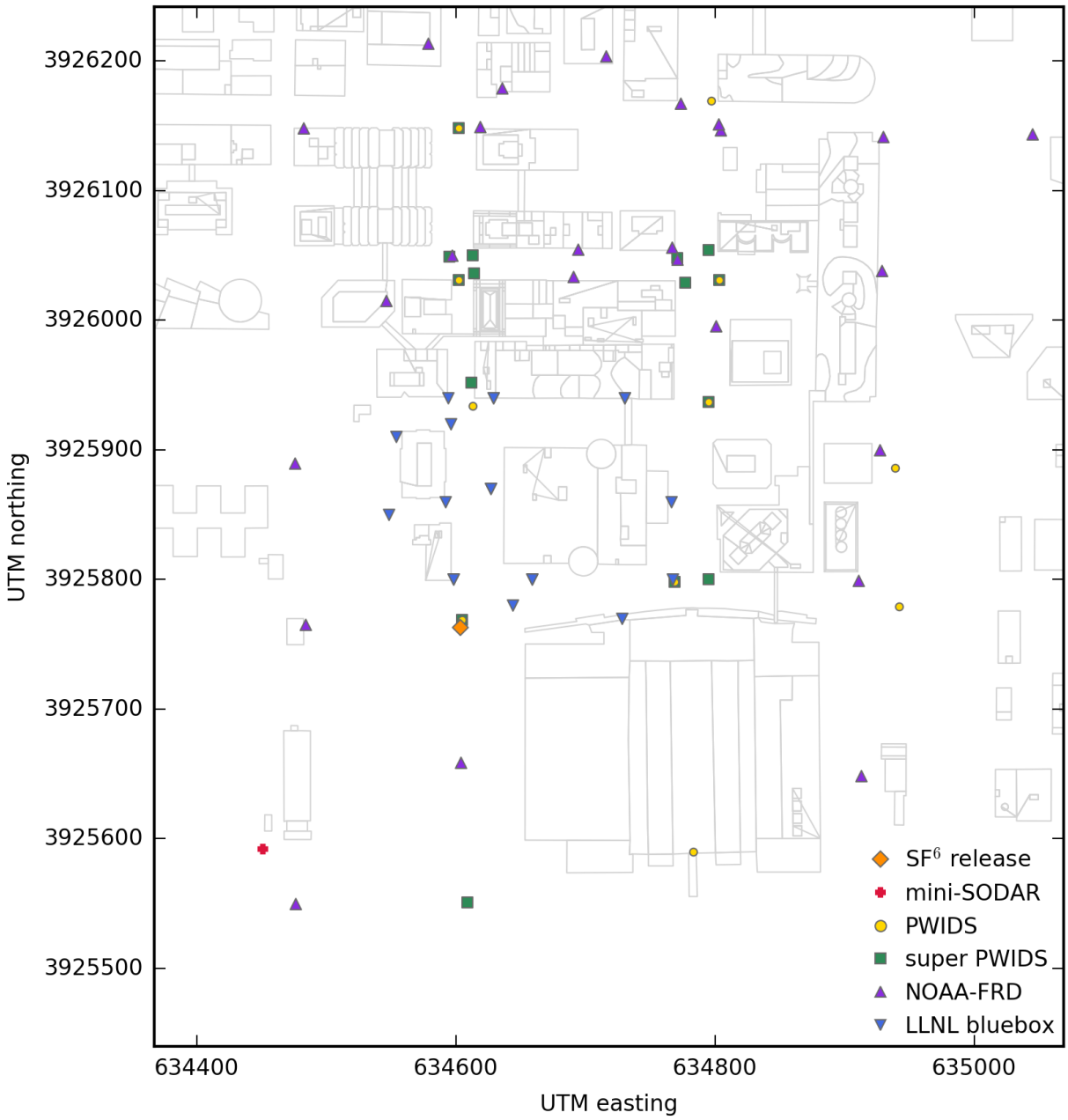

Figure 2.3: A map of the Oklahoma City business district showing measurement stations used during the analysis of simulation results. The SF_6 release location was located at UTM coordinates (634603, 3925763). The ANL miniSODAR was located at UTM coordinates (634451, 3925592). The plot's limits are coincident with the lateral boundaries of the innermost domain with 2 m horizontal resolution.

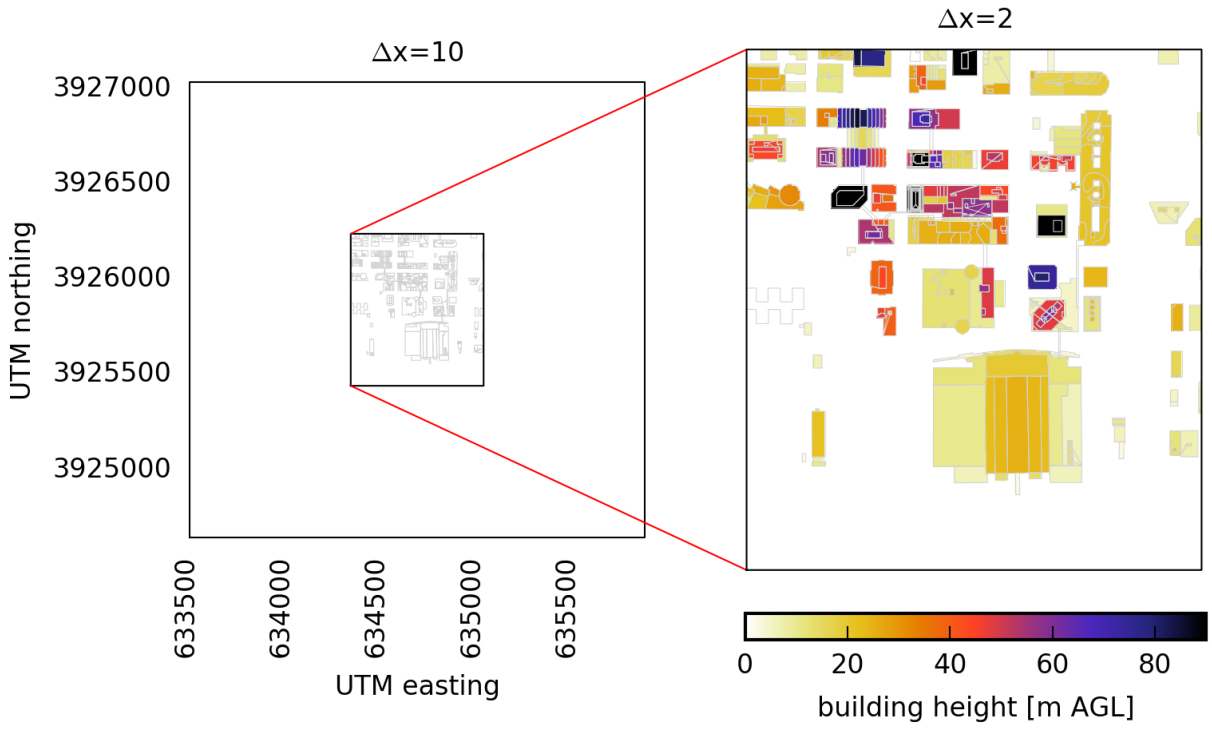

Figure 2.4: A plan view of the two domain nested configuration used for idealized WRF-IBM simulations. The outer domain is marked with UTM coordinates.

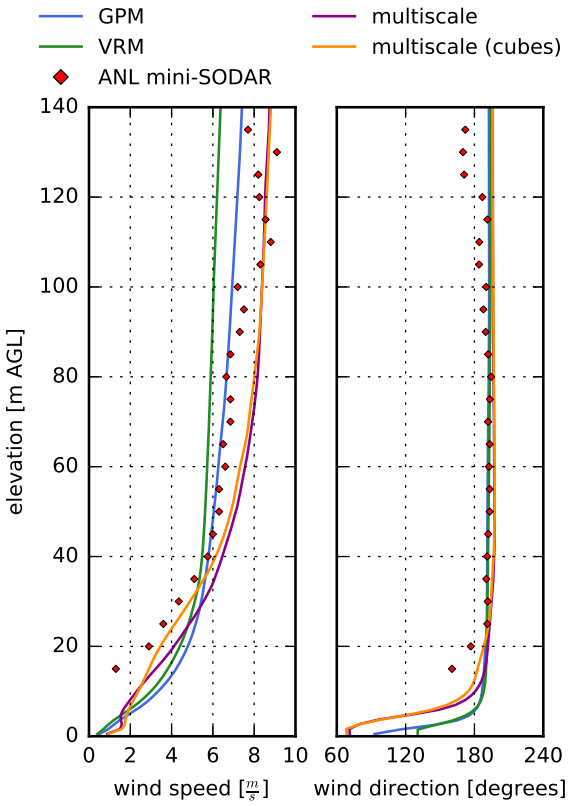

Figure 2.5: Vertical profiles at the ANL miniSODAR location (634451, 3925592) of horizontal wind speed and direction. Profiles have been time-averaged over the 30 minute SF_6 release period. Observations from the ANL miniSODAR are included along with results from the idealized VRM, idealized GPM, multiscale simulation, and the multiscale simulation with added roughness elements on the 10 m domain (cubes).

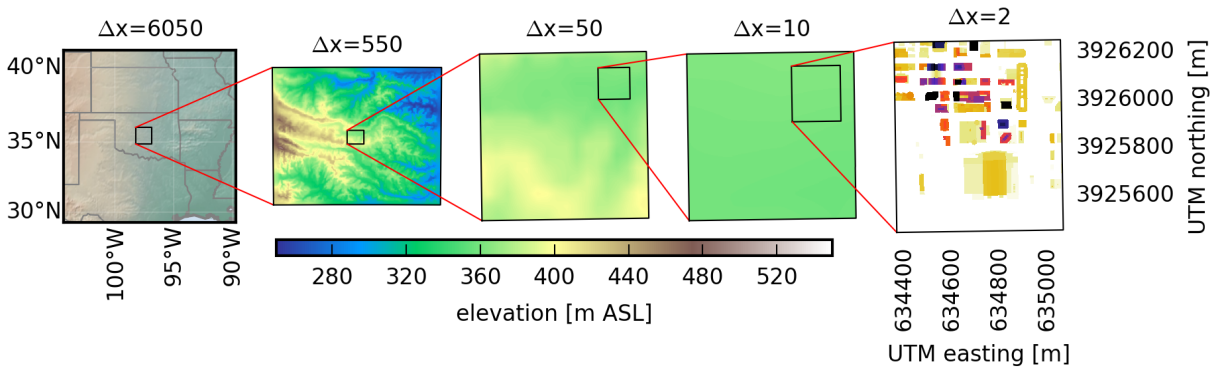

Figure 2.6: Configuration of domains used in the multiscale simulation centered over the business district of Oklahoma City, OK. The five domains have resolutions of 6.05 km, 550 m, 50 m, 10 m, and 2 m. The 550 m, 50 m, and 10 m domains include contour levels of topography. The 2 m domain includes contours of the building heights AGL (colorbar not shown). Dimensions of each domain and other configuration information is included in Table 2.1

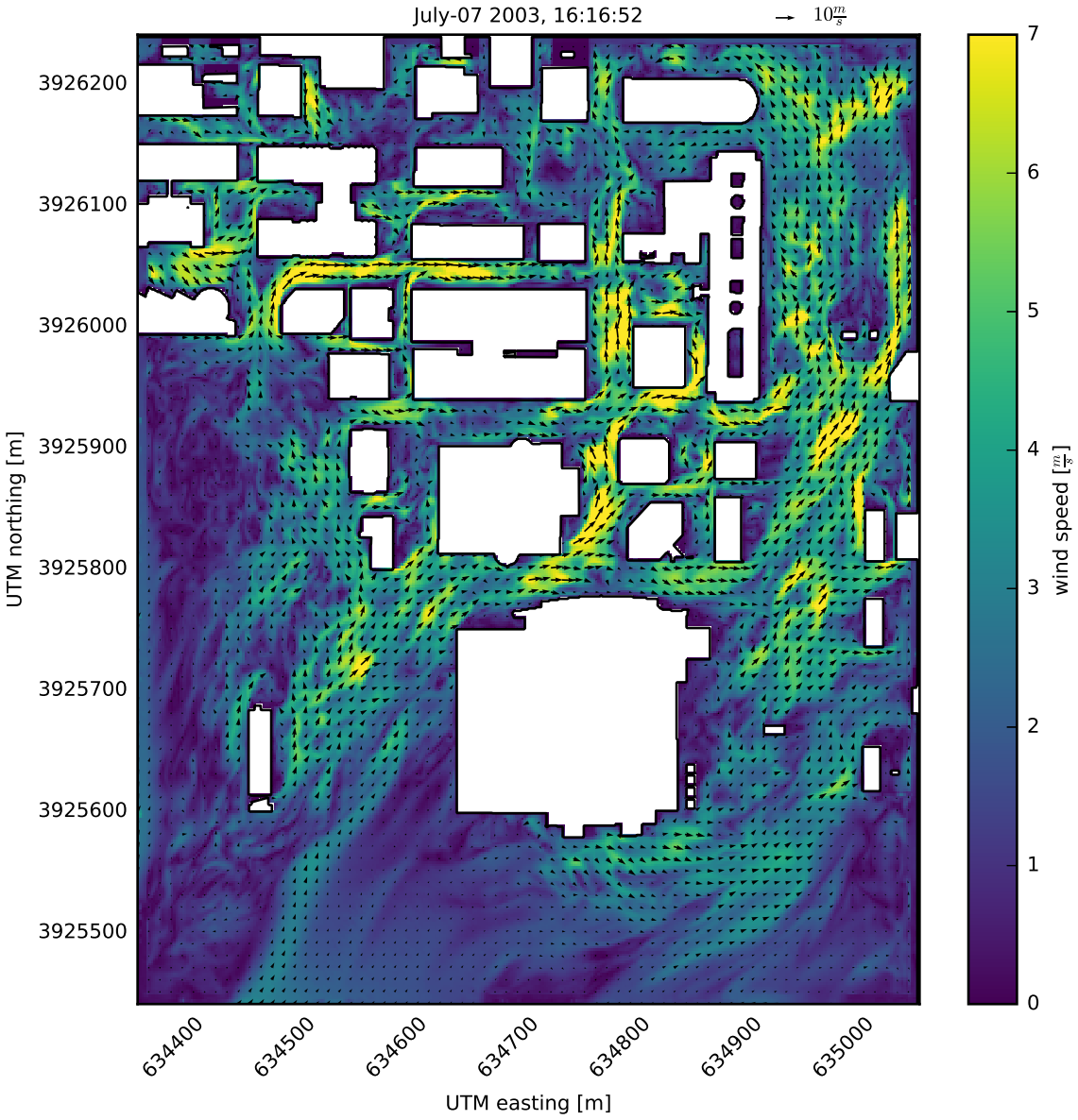

Figure 2.7: Instantaneous horizontal wind speed 8 m AGL at 16:16:52 UTC from the 2 m domain of the multiscale simulation. Quivers are included at every fifth grid point. An animation of horizontal wind speed at 8 m AGL from the innermost four domains of the multiscale simulation is included in the supplementary materials.

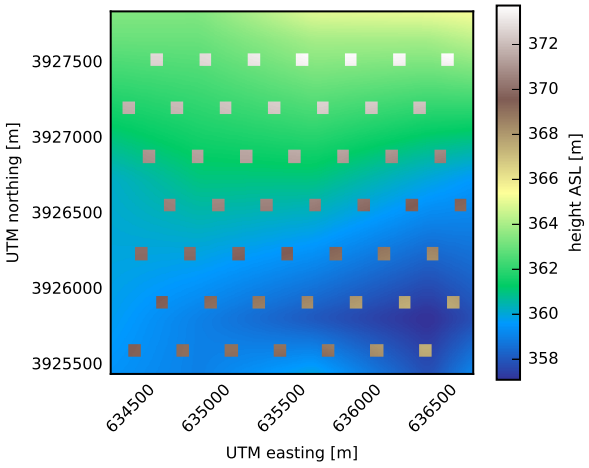

Figure 2.8: Topography from the multiscale simulation 10 m domain with cubes (80×80×10 m) added to mimic the effects of the urban terrain.

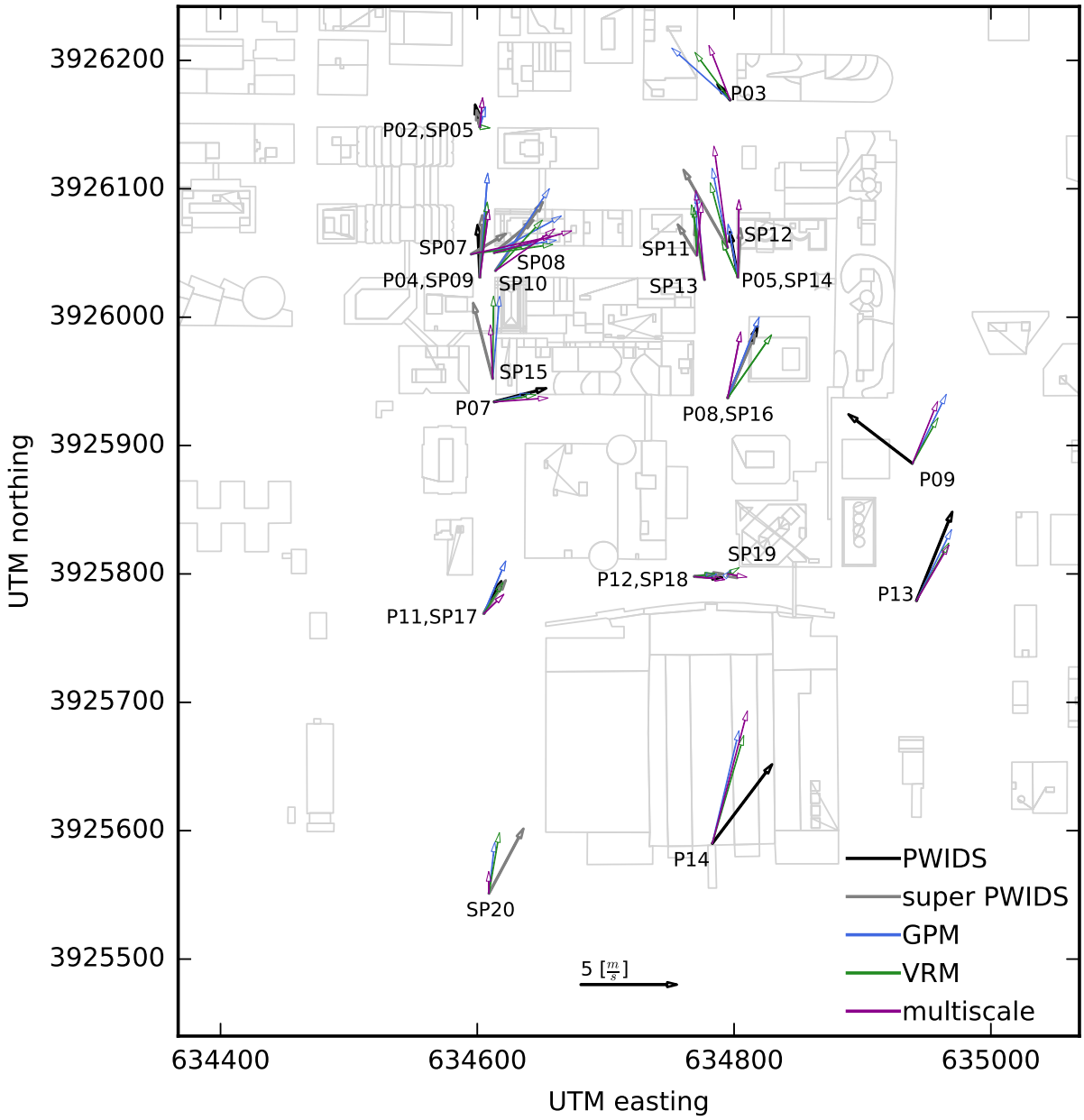

Figure 2.9: Horizontal wind speed and direction, time-averaged over the 30 minute SF_6 release period, at the locations of DPG PWIDS (P) and DPG super PWIDS (SP). Arrows are included for observations and the three simulations (idealized GPM, idealized VRM, and multiscale).

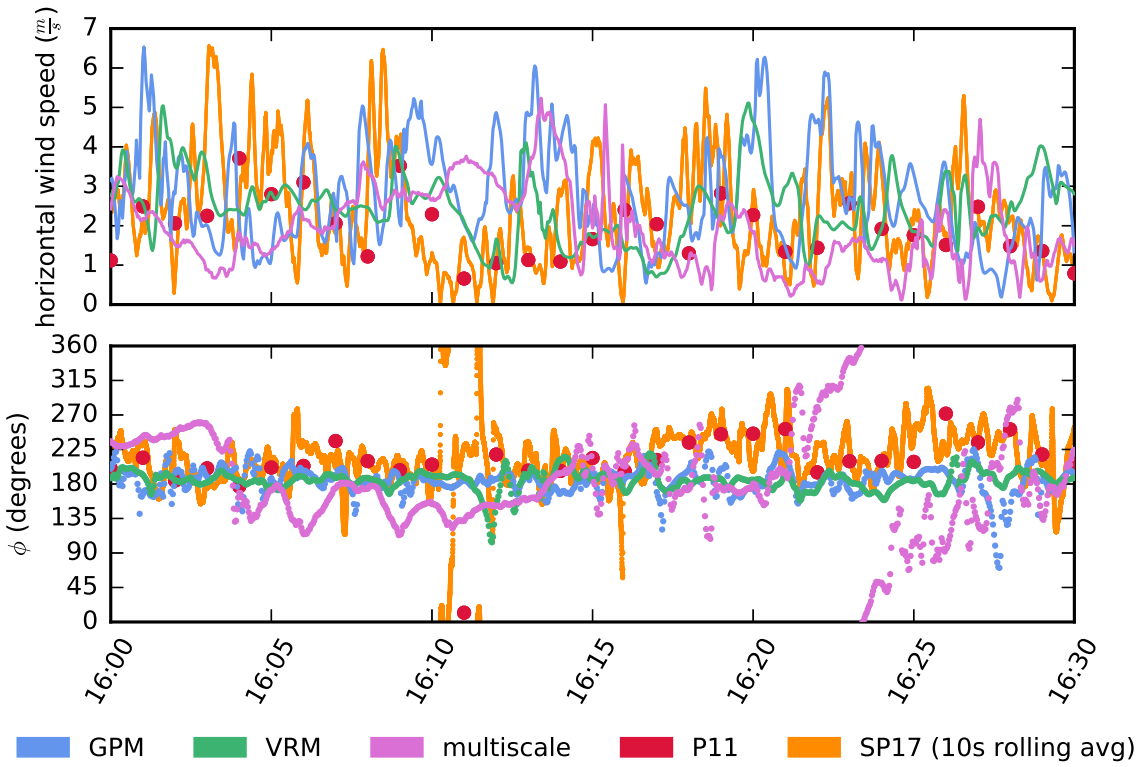

Figure 2.10: A timeseries of horizontal wind speed and wind direction at 8 m AGL at the SF_6 release location for the idealized GPM, idealized VRM, and multiscale simulations. Also plotted are DPG PWIDS (P11) and super PWIDS (SP17), which are collocated 8 m AGL at the release location. Data from SP17 is shown after the application of a rolling average filter with window length of 10 s.

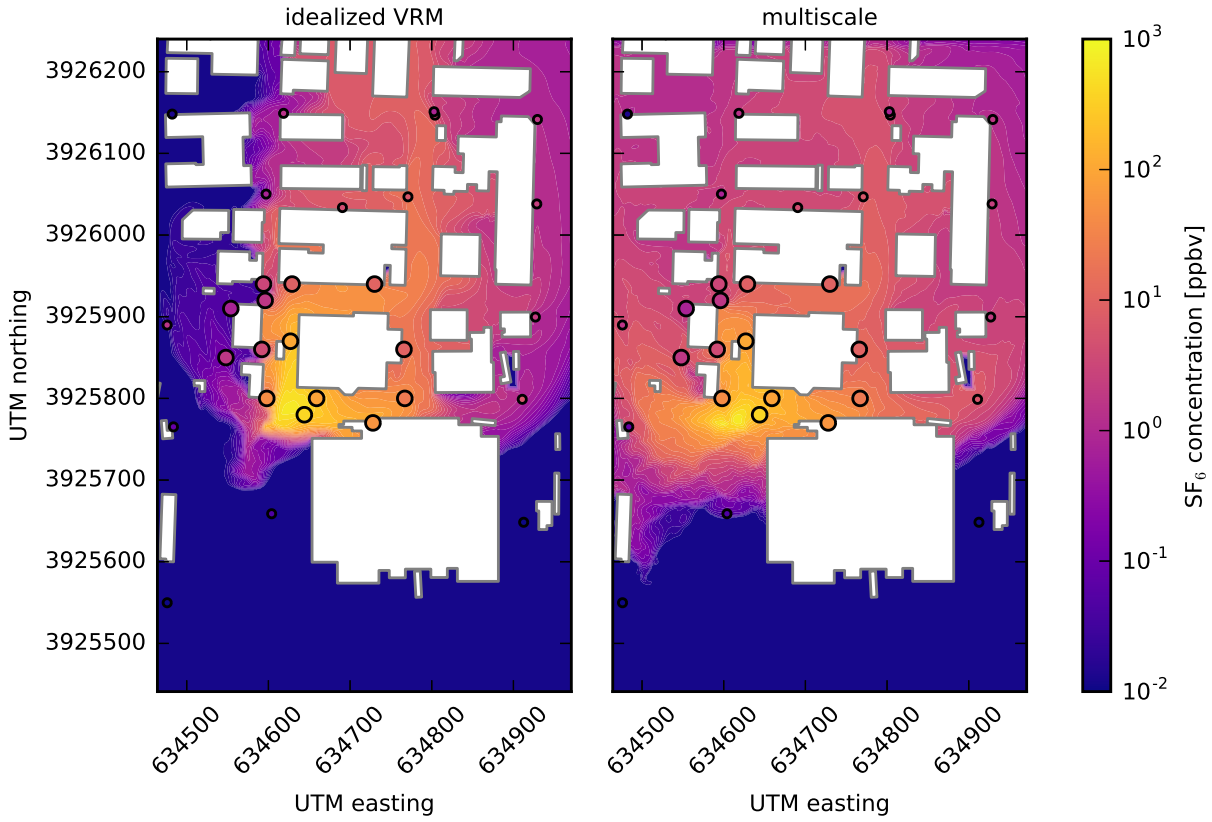

Figure 2.11: SF_6 concentrations at 2.5 m AGL from the idealized WRF-IBM-VRM simulation (left) and multiscale simulation (right). Both the observed and predicted concentrations shown are time-averaged over the 30 minute release period. Large circles represent time-averaged measurements from LLNL "bluebox" stations. Small circles represent time-averaged measurements from NOAA ARL FRD PIGS stations. Only LLNL stations with height of 2.5 m AGL and NOAA stations with a height of 8 m AGL are shown. An animated version of this plot is available in the supplemental materials.

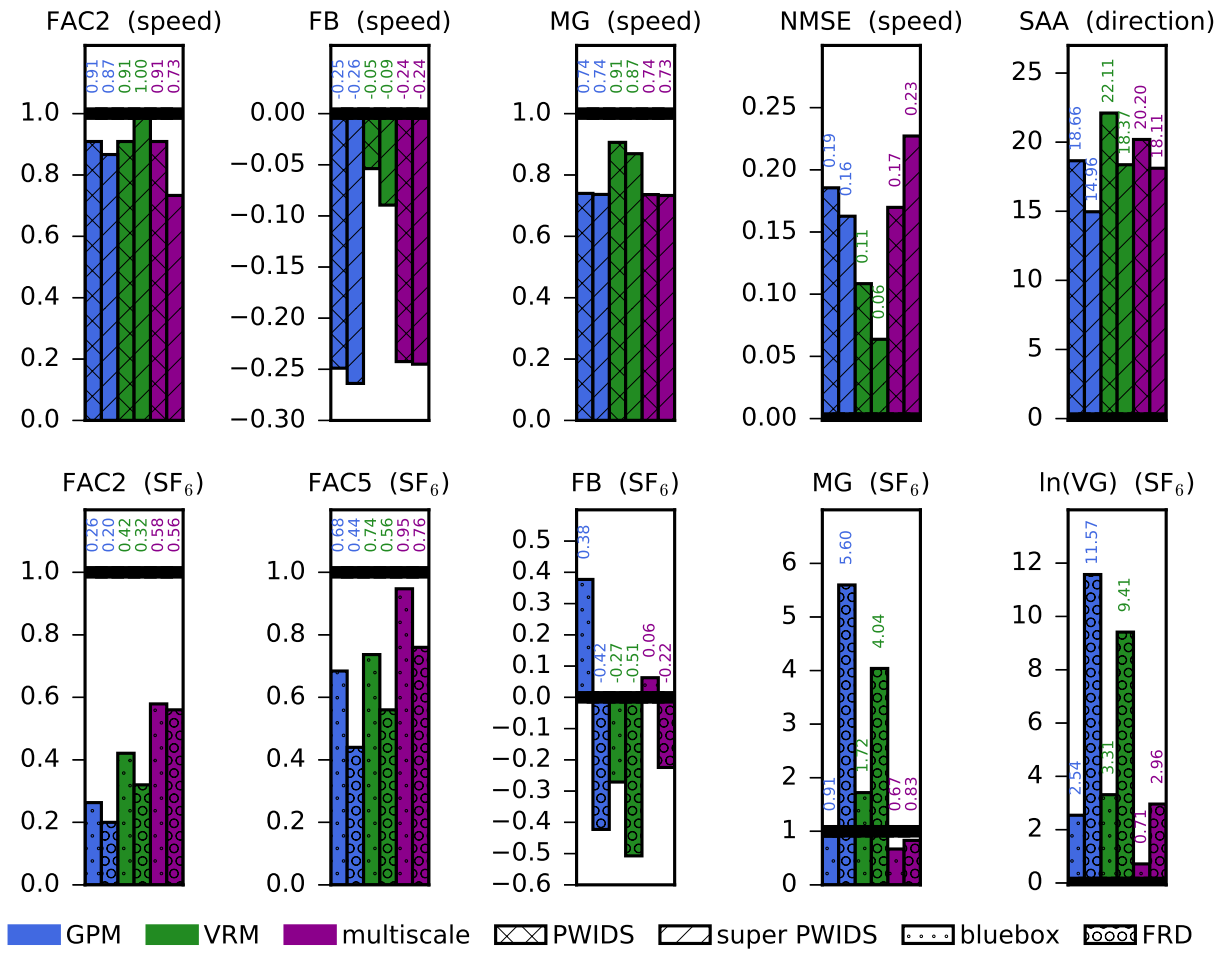

Figure 2.12: Model skill test results evaluating horizontal wind speed and wind direction (top row), and SF_6 concentration (bottom row) for the idealized VRM, idealized GPM, and multiscale simulations compared to DPG PWIDS and super PWIDS, and LLNL "bluebox" and NOAA ARL FRD integrated tracer samplers. Black lines indicate a perfect model score.

Chapter 3

Investigation of sensitivity to grid resolution

3.1 Introduction

Recent developments to numerical weather prediction (NWP) models have made feasible large-eddy simulations (LES) of the planetary boundary layer (PBL) over complex topography using microscale resolutions (i.e. $\Delta < 100$ m). Results of these simulations are particularly sensitive to the model configuration and grid quality (Mirocha et al. 2013; Mirocha and Lundquist 2017). Recent research, such as the multiscale simulations of Wiersema et al. (2020), highlight the difficulty of configuring nested simulations with five or more modeling domains that are each sensitive to both their configuration and that of their parent domain(s).

In multiscale simulations, an inaccurate or nonphysical solution on a parent domain will corrupt the solutions of any nested child domains. Following this logic, modelers should use best practices when constructing grids, selecting parameterizations and configuring each simulation. Unfortunately, defining "best practices" is easier said than done, especially when modeling within notoriously complicated regimes, such as the *terra incognita* (i.e. the turbulence gray zone) (Wyngaard 2004).

The turbulence gray zone is a numerical regime where the energy-containing length scales of turbulence are roughly the same magnitude as the scale of the LES filter (i.e. related to the grid resolution). In this regime, the use of a planetary boundary layer scheme is inappropriate because the largest turbulent features can be resolved, however the use of a LES turbulence closure model is also questionable because a large portion of energetic turbulence cannot be resolved. Because multiscale simulations use a telescoping sequence of nested domains with grid resolutions spanning between the mesoscale and microscale, at least one of the intermediate domains is likely to be within the turbulence gray zone.

Another problem that can hinder multiscale NWP simulations is grid distortion over steep terrain slopes due to the body-fitted (i.e. terrain-following) coordinates commonly used in

NWP models, such as the Weather Research and Forecasting (WRF) model that is used in this study. When simulating over real topography at LES resolutions (i.e. $\Delta < 200$ m), the resolved terrain slopes are increased compared to those in more coarse resolution simulations.

Immersed boundary methods (IBMs) are techniques for imposing the effects of a physical boundary on fluid flow. These methods do not require a body-fitted coordinate system, such as the terrain-following vertical coordinate in the WRF model, which can greatly simplify gridding. IBMs provide a robust and convenient procedure for implementing bottom boundary conditions, particularly at high resolutions over complex topography where terrain-following coordinates result in grid distortion that may cause model failure. Variations of IBMs have been developed for a wide variety of applications and excellent summaries of current techniques have been written by Iaccarino and Verzicco (2003), Senocak et al. (2004), Mittal and Iaccarino (2005) and Bao et al. (2016).

In this study, we attempt to clarify some of the "best practices" for configuring simulations of the PBL over complex terrain when using grid resolutions that range from 25 to 200 m. In particular, this study examines simulation sensitivity at various grid resolutions to the choice of IBM algorithm that is used to maintain the bottom boundary condition. Additionally, the hybrid Reynolds Averaged Navier Stokes (RANS) and LES scheme of Senocak et al. (2007) is investigated and found to improve the results of simulations within the turbulence gray zone.

The 24 simulations compared here use topography specified using an Agnesi function that resembles a smooth, steep, symmetric hill. To avoid errors resulting from the topography gray zone, where grid resolution is of the the same magnitude as the scale of topographic features, the idealized terrain has been configured such that it is adequately resolved for all grid resolutions evaluated.

There are many past sensitivity studies evaluating simulations over complex terrain, including the Bolund hill (Diebold et al. 2013) and Askervein hill (Silva Lopes et al. 2007; Arthur et al. 2019). Both the Bolund and Askervein hills have small spatial scales and cannot be adequately resolved at the coarse grid resolutions (i.e. 50, 100 and 200 m) evaluated in this study, which is why idealized topography is used. It should be noted that most, but not all, previous grid resolution sensitivity studies over complex terrain have purposefully avoided using resolutions within the turbulence gray zone.

A notable previous grid resolution sensitivity study that includes gray zone resolutions is that of Bao (2018), which also evaluated flow over an idealized hill at 50, 100 and 200 m resolutions using three IBM algorithms. There are several differences between the current study and that of Bao (2018), including changes to the IBM algorithms, different idealized hill slopes, the addition of simulations at 25 m grid resolution, differences in the methodology used to calculate the simulation error, and an increased emphasis on the spatial distribution of the simulation error.

More recently, Arthur et al. (2019) evaluated the performance of two IBM algorithms, also used in this study, including analysis of simulations over topography of an idealized hill with horizontal grid resolutions of 16, 32, 64 and 128 m. Additionally, the configuration at each horizontal resolution was evaluated at several grid aspect ratios ranging from $1 \leq$

$\Delta_x/\Delta_z \leq 16$. While the configurations of Arthur et al. (2019) are similar to those evaluated here, the present study evaluates only one grid aspect ratio, includes more coarse resolutions, and emphasizes the spatial distribution of the error.

3.2 Immersed boundary method algorithms

Two IBM algorithms are evaluated in this study; the velocity reconstruction method (IBM-VRM) and the shear reconstruction method (IBM-SRM), which are detailed below.

For the IBM algorithms considered here, the surface boundary is immersed within the modeling grid and divides the domain into grid points in the fluid domain that are above the immersed boundary (IB) and grid points in the solid domain that are beneath the IB. IBMs maintain a bottom boundary condition by modifying velocities at grid points that are in proximity to the IB through the addition of a body force term shown here in a simplified form of the governing equation for momentum,

$$\partial_t \boldsymbol{V} + \boldsymbol{V} \cdot \boldsymbol{\nabla} \boldsymbol{V} = -\alpha \boldsymbol{\nabla} p + \nu_t \nabla^2 \boldsymbol{V} + \boldsymbol{g} + \boldsymbol{F_B} \tag{3.1}$$

where $\boldsymbol{V}$ is the velocity vector, α the specific volume, p is pressure, $\boldsymbol{g}$ is gravitational acceleration, ν_t is turbulent viscosity, and $\boldsymbol{F_B}$ the body force term. For the simulations simulations in this study, $\boldsymbol{F_B}$ is not directly calculated; instead, the effects of $\boldsymbol{F_B}$ are implied by adjusting variables near the immersed boundary to maintain a desired boundary condition.

Velocity reconstruction method

The IBM-VRM used here is similar to the method used in Senocak et al. (2004), which modifies near-surface velocities above the IB to maintain a log-law boundary condition. IBM-VRM reconstructs velocities at grid points above and adjacent to the IB, which are referred to as reconstruction points (RPs). Further details and validation of the IBM-VRM can be found in Bao et al. (2018) and Wiersema et al. (2020).

For each RP, the method calculates a vector that passes through the RP and is normal to the nearest section of the IB. Next, an interpolation point (IP) is located by projecting away from the IB and along the vector until reaching the face of a grid cell. The IP magnitude is determined using an inverse distance weighting (IDW) interpolation scheme and the magnitudes of the nearest neighboring grid points that are above the IB. Additional details of the IDW interpolation scheme are included in Lundquist et al. (2012) and Wiersema et al. (2020). The IP and RP magnitudes can then be related, as shown in Equations 3.3a and 3.3b, by assuming a log-law for neutrally-stratified flow over a rough surface,

$$U = \frac{u_*}{\kappa} \ln\left(\frac{z}{z_0}\right), \tag{3.2}$$

where z is surface normal distance from the IB, z_0 is a roughness height, u_* is the friction velocity, κ is the von Kármán constant ($\kappa = 0.4$ is used here), and U is the magnitude of

the velocity. Using the assumed log-law relationship, the RP velocities are related to the IP as follows,

$$U_{RP} = U_{IP} \frac{\ln\left(\frac{d_{RP}}{z_0}\right)}{\ln\left(\frac{d_{IP}}{z_0}\right)}. \tag{3.3a}$$

By assuming a linear relationship of w, the surface normal velocity, with d, the distance from the IB, and $w\,(d = 0) = 0$ then w_{RP} is found to be,

$$w_{RP} = w_{IP}\ \frac{d_{RP}}{d_{IP}}. \tag{3.3b}$$

The tangential wind speed, U_{RP}, can then be separated into u and v velocities, where θ is the tangential wind direction defined using geographic convention.

$$\theta = \arctan\left(\frac{u_{IP}}{v_{IP}}\right) \tag{3.4a}$$

$$u_{RP} = U_{RP}\ \sin\theta, \quad v_{RP} = U_{RP}\ \cos\theta \tag{3.4b}$$

Finally, the u, v, and w velocities at the RP, which are calculated in Equations 3.3b and 3.4b using a surface-normal coordinate system, are rotated to the grid orientation.

Velocities beneath the IB, which do not represent physical flow, are involved in the calculation of the resolved strain-rate tensor, S_{ij}. This can lead to errors in the eddy viscosity that can be particularly noticeable as grid resolution is coarsened. For the 3D Smagorinsky closure scheme used in these simulations, the eddy viscosity ν_t is calculated as,

$$\nu_t = \left(C_s\left(\Delta_x\Delta_y\Delta_z\right)^{\frac{1}{3}}\right)^2 \left|S_{ij}\right|, \tag{3.5a}$$

where C_s is the Smagorinsky coefficient (0.18 is used here) and the resolved strain-rate tensor is defined as,

$$S_{ij} = \frac{1}{2}\left(\frac{\partial u_i}{\partial x_j} + \frac{\partial u_j}{\partial x_i}\right) \tag{3.5b}$$

The eddy viscosity is reconstructed at grid points above and adjacent to the IB. This reconstruction assumes a linear relationship of ν_t with distance from the IB and $\nu_t = 0$ m^2 s^{-1} at the IB (Senocak et al. 2004; DeLeon et al. 2018; Arthur et al. 2019).

Shear reconstruction method

The IBM-SRM used in these simulations has previously been evaluated by Bao et al. (2016) and Bao (2018) and follows comparable implementations by Chester et al. (2007) and Ma and Liu (2017). At grid points near the immersed boundary, IBM-SRM calculates the model stresses necessary to maintain a log-law boundary condition. Unlike IBM-VRM, velocities above the IB are not directly modified but instead are indirectly controlled by

modification of the stresses. IBM-SRM reconstructs the stress tensor for each grid point adjacent to and above the IB. Reconstructed stress values are then extrapolated to the grid points adjacent to and below the IB. Velocities are set to 0 m s^{-1} at all grid points beneath the IB but they are not directly modified at grid points located above the IB.

For each grid point where reconstruction is to be performed, the surface-tangential stress τ_S^t is calculated as,

$$\tau_S^t = \left[\frac{\kappa U_{IP}^t}{\ln\left(\frac{d_r}{z_0}\right)} \right]^2 \tag{3.6}$$

where κ is the von Kármán constant ($\kappa = 0.4$), U_{IP}^t is the surface-tangential velocity at the surface-normal distance d_r from the IB, and z_0 is the roughness length. For this study, $d_r = 1.2\Delta_z$ and U_{IP}^t is calculated using the IDW interpolation scheme.

After calculating the stress components at all reconstruction points, the stresses above the IB are then extrapolated to grid points that are beneath and adjacent to the IB. For each stress set via extrapolation, the grid point location is projected in the surface normal direction across the IB and three interpolation points (IP) are specified at distances from the IB of 1.1, 2.2 and 3.3 times Δ_z. At each IP, the stress component is calculated using the IDW interpolation scheme and the stresses at nearest neighboring grid points. A second order Lagrange polynomial,

$$\tau_{EP} = 3\tau_{\mathrm{IP1}} - 3\tau_{\mathrm{IP2}} + \tau_{\mathrm{IP3}} \tag{3.7}$$

is used to calculate the stress at an extrapolation point, τ_{EP}, using the stress at three IPs, where IP1 is nearest to the IB and IP3 is farthest.

Because the IBM-SRM requires grid points beneath the bottom boundary (i.e. ghost points) for the extrapolation of above-boundary stresses, this IBM algorithm is currently not compatible with nested domains of WRF simulations that include a terrain-following parent domain, such as the multiscale simulations of Wiersema et al. (2020). This incompatibility arises due to the WRF model's restriction that nested domains have the same total column pressure at coincident grid points. For this reason, the IBM-SRM is currently limited to idealized and microscale-only simulations.

3.3 Hybrid RANS/LES scheme

In LES, a subgrid-scale (SGS) turbulence model is used to parameterize turbulent motions at scales that are unable to be resolved. Optimally, the LES grid resolution will be fine enough to resolve the bulk of energetic turbulent motions and it is assumed that the SGS model parameterizes a small portion of the total turbulent energy. Near the rough bottom boundary, the characteristic length scale of turbulence decreases and the fraction of turbulent energy parameterized by the SGS model increases. This typically results in inaccurate behavior by the SGS model near the surface.

One workaround of this problem is a hybrid formulation of Reynolds-averaged Navier Stokes and LES proposed by Senocak et al. (2007). Away from boundaries, where the LES resolves the energy-containing scales of turbulence, the SGS model is applied. Near boundaries, a RANS solution for the eddy viscosity, ν_t, is applied. Transitioning between these regimes is accomplished using an exponential blending function (Equation 3.8) (van Driest 1956):

$$\nu_t = \left[\left(1 - \exp\left(\frac{-z}{h} \right) \right)^2 \left(C_s \Delta^2 \right) + \exp\left(\frac{-z}{h} \right)^2 (\kappa z)^2 \right] |S| \,. \tag{3.8}$$

In the above equation, z is the height above the boundary, h is a user-specified blending height, C_s is the Smagorinsky coefficient (0.18 for these simulations), κ is the von Karman constant of 0.4, and Δ is a function of the horizontal and vertical grid resolutions (Δ_x, Δ_y and Δ_z) and map scale factors (m_x and m_y) calculated using Equation 3.9.

$$\Delta = \left(\frac{\Delta_x}{m_x} \, \frac{\Delta_y}{m_y} \, \Delta_z \right)^{\frac{1}{3}} \tag{3.9}$$

Selection of a blending height h is informed by bounds based on numerical and physical limits. Following Senocak et al. (2007), we assume a physical upper bound of the surface layer depth. Stull (1988) observes that a surface layer with a logarithmic velocity profile exists in approximately the bottom 10% of a neutrally stratified PBL with depth h_{PBL}. The lower bound of h is based upon the numerical length scale of the LES closure inferred using the Nyquist theorem to be twice the grid resolution. These bounds provide an acceptable range of values to guide our choice of h for each simulation configuration.

$$2 \, \min\left(\Delta_x, \, \Delta_y, \, \Delta_z \right) < h < 0.1 \, h_{PBL} \tag{3.10}$$

A value of $h = 6 \, \Delta_z$ is used for our simulations with the hybrid RANS/LES scheme enabled.

3.4 Sensitivity study over idealized topography

Six model configurations are evaluated using the WRF model version 3.8.1 by simulation of flow over an idealized hill at four different resolutions. These 24 simulations are distinguished by their grid resolution, bottom boundary condition, and whether the RANS/LES hybrid scheme is enabled.

Horizontal resolutions of Δ_x = 25, 50, 100 and 200 m are used with vertical resolutions of Δ_z = 5, 10, 20 and 20 m, respectively. Simulations with Δ_x = 25, 50 and 100 m have a near-surface aspect ratio (Δ_x/Δ_z) of 5, which is near the recommended aspect ratio of 4 from Mirocha et al. (2013). Maintaining an aspect ratio of 5 in the present simulations with Δ_x = 200 m would result in a problematically coarse vertical resolution near the surface. We have chosen to instead use the same vertical resolution as the Δ_x = 100 m simulations

Table 3.1: Simulation details for the idealized hill cases, including the domain extents in each dimension (L_x, L_y and L_z), the number of grid points N in each dimension (N_x, N_y and N_y) and the grid resolutions (Δ_x and Δ_z). The vertical grid resolution Δ_z is constant up to 400 m above which it is stretched by a factor r until reaching Δ_z=100 m, above which it remains constant. L_z and N_z are increased for IBM cases to accommodate an additional two grid cells beneath the terrain, which are necessary for the IBM-SRM algorithm.

Case	$(L_x,$	$L_y,$	$L_z/L_{z\ ibm})$	$(N_x,$	$N_y,$	$N_z/N_{z\ ibm})$	$\Delta_x = \Delta_y$	Δ_z	r
1 (true)	(6,	6,	4/ 4.01)	(240,	240,	150/ 152)	25	5	1.050
2	(6,	6,	4/ 4.02)	(120,	120,	99/ 101)	50	10	1.050
3	(6,	6,	4/ 4.04)	(60,	60,	69/ 71)	100	20	1.049
4	(6,	6,	4/ 4.04)	(30,	30,	69/ 71)	200	20	1.052

and not maintain the grid aspect ratio, which may introduce additional variability to the simulations with $\Delta_x = 200$ m. We note also that the optimal grid aspect ratio discussed previously is not necessarily expected to hold over topography (Mirocha et al. 2010). A summary of the four grid configurations is included as Table 3.1.

The simulation terrain is of an idealized hill defined by an Agnesi function (Equation 3.11). Each domain has horizontal extents of 6 km and the idealized hill is sized such that it is large enough to allow the model configurations to be tested at coarse horizontal resolutions of $\Delta_x = 100$ and 200 m.

$$h\left(x, y\right) = \frac{h_p}{1 + \left(x/L_h\right)^2 + \left(y/L_h\right)^2} \tag{3.11}$$

Values of $h_p = 250$ m and $L_h = 800$ m are used for all simulations. These constants result in topography that is a compromise between providing a tall enough obstruction to create a well defined flow separation in the lee of the hill and the need to avoid steep slopes that would be prohibitive for the terrain-following simulations.

The simulations use periodic lateral boundary conditions and are forced by a geostrophic velocity of $u_1^g = 10$ m s^{-1}. The 3-dimensional Smagorinsky turbulence closure is used with coefficient $C_s = 0.18$. A uniform surface roughness of $z_0 = 0.1$ m is applied when using the IBM methods. Rayleigh damping is applied to vertical velocities within the top 2000 m of each domain using a damping coefficient of 0.2 s^{-1}.

High-resolution results

First we examine the results from simulations using the basic implementations of both the IBM-VRM and IBM-SRM compared to terrain-following WRF at $\Delta_x = 25$ m. The results of each simulation are time averaged over hours 24-48, during which the flow is turbulent and quasi-steady. A similar flow solution is achieved by all three methods, with a turbulent

wake in the lee of the hill and the highest velocities observed as the flow passes over the hill summit. The flow veers near the surface due to the Coriolis force and the resulting time-averaged surface winds are from the southwest. For this reason, we evaluate the simulation results along a transect angled at 75° clockwise from north and intersecting the domain center (i.e. hill summit). The time-averaged along-transect velocity, V_t, is defined as

$$\langle V_t \rangle = \langle V_h \rangle \cos\left(\langle \phi \rangle - \phi_t\right), \tag{3.12}$$

where $\langle V_h \rangle$ is the time-averaged wind speed, $\langle \phi \rangle$ is the time-averaged wind direction, and ϕ_t is the angle of the transect. Vertical profiles of time-averaged along-transect velocity $\langle V_t \rangle$ from the simulations with $\Delta_x = 25$ m are shown in Figure 3.1. The results of these simulations are qualitatively similar to those of Ma and Liu (2017), who compared multiple IBM algorithms in the WRF model for simulation of flow over an idealized hill with a similar domain setup and grid resolution.

Further examination of the flow profiles along the transect in Figures 3.1 reveals differences between the six simulations at 25 m horizontal resolution. While the along-transect profiles are visually aligned over the flatter parts of the topography (e.g., the first four profiles in Figure 3.1a), minor differences occur at the steepest regions and at the summit. Large differences in $\langle V_t \rangle$ between the $\Delta_x = 25$ m simulations are evident in the lee of the hill (Figure 3.1b). In general, both the IBM-VRM and IBM-SRM yield slower flow near the surface, especially in the lee of the hill, compared to WRF. All three methods do produce an inflection point in the velocity profile in the lee of the hill, which indicates the presence of recirculating flow.

With the hybrid RANS/LES scheme enabled, all three configurations show a notable reduction in the strength of the recirculation formed in lee of the hill. Both terrain-following WRF and the IBM-VRM simulation produce velocity profiles in lee of the hill, shown in Figure 3.1b, that maintain a logarithmic shape comparable to those upwind of the hill, shown in Figure 3.1a. Only the IBM-SRM simulation appears to produce flow separation in lee of the hill and establish a recirculation. The strength of this recirculating flow is nearly identical to that predicted by the terrain-following WRF simulation when the hybrid RANS/LES scheme is disabled.

The high-resolution ($\Delta_x = 25$ m) idealized hill case highlights the limits imposed upon native WRF by errors related to the terrain following grid. When configuring these simulations, multiple idealized hill heights were completed prior to settling on the current terrain configuration. As the hill height is increased, the maximum slopes correspondingly increase. The current configuration, which has a maximum slope of 20.3°, is near the limits of the WRF model when using terrain-following coordinates because of the errors associated with grid distortion.

At $\Delta_x = 25$ m, topography of realistic hills would likely yield significantly higher resolved slopes that would prove problematic for the use of terrain-following coordinates. It should also be noted, as discussed by Daniels et al. (2016), that errors due to grid distortion are a function of both the terrain slope and the grid aspect ratio, $\alpha = \Delta_x/\Delta_z$. Over sloped

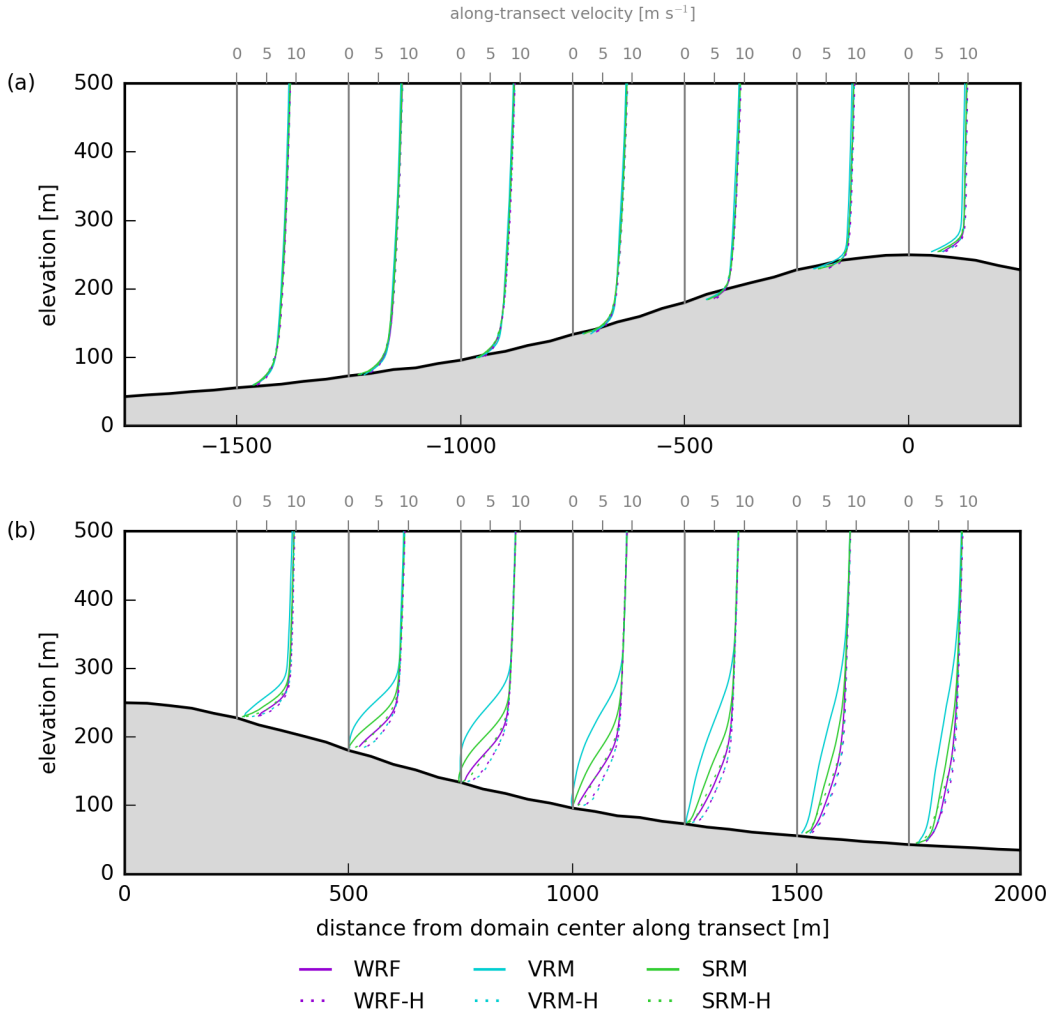

Figure 3.1: Time-averaged along-transect velocity profiles $\langle V_t \rangle$ from simulations with terrain-following WRF, IBM-VRM, and IBM-SRM at $\Delta_x = 25$ m with and without the hybrid RANS/LES scheme. The profiles are oriented along a transect angled at 75° clockwise from north and passing through the domain center (i.e. hill summit). The transect is split into two subplots showing in lee of the idealized hill (a) and upwind of the idealized hill (b). Simulations with the hybrid RANS/LES scheme enabled are labeled with "-H".

topography, a high α may cause the elevation difference between adjacent grid points being larger than the vertical grid spacing, which results in numerical errors when approximating the horizontal gradient terms (Mahrer 1984). Despite a relatively gentle maximum slope, the grid aspect ratio of $\alpha = 5$ provides an additional potential for errors (see Figure 1 in Daniels et al. 2016).

The idealized hill results demonstrate that even when using relatively high resolution ($\Delta_x = 25$ m), there may be significant differences in the flow predicted over complex terrain by terrain-following WRF, IBM-VRM and IBM-SRM. These differences were most pronounced in the lee of the hill where recirculating flow may develop. In the next section, these differences will be explored more thoroughly, and as a function of grid resolution.

Grid resolution study

A grid resolution study is performed to examine WRF and IBM performance as the model grid is coarsened from the simulations in Section 3.4. Flow over the idealized hill is simulated using terrain-following WRF, as well as the IBM-VRM and the IBM-SRM with horizontal resolutions of $\Delta_x = 25$, 50, 100 and 200 m. A summary of the four grid configurations is included as Table 3.1. The finest ($\Delta_x = 25$ m) terrain-following WRF case is taken to be the "true" solution, such that the error in other simulations is defined relative to it. An aspect ratio value of 5 is used here for cases 1-3. As mentioned in Section 3.4, when $\Delta_x = 200$ m, Δ_z is kept at 20 m because an extremely coarse Δ_z of 40 m would lead to poor results and undesired behavior near the surface.

The following process is used to calculate the difference between each simulation and the true solution. First, both solutions are time averaged between hours 24-48 to remove turbulent fluctuations. Then, the time-averaged wind fields are vertically interpolated onto planes at constant heights above ground level. Because we are most interested in the near-surface differences in the flow, we consider ten planes at 10 m increments between 10 and 100 m above ground level (AGL). Next, if the comparison case has coarser horizontal resolution than the true solution, the true solution is horizontally downsampled to the resolution of the coarser case. When downsampling, fine domain grid cells within a coarse domain grid cell are averaged with equal weight given to each. Finally, the error E is calculated based on the total velocity magnitude $V = \sqrt{u_i^2}$ as,

$$E = \langle V \rangle - \langle V \rangle_{\text{true}}. \tag{3.13}$$

If $E > 0$ the flow is fast relative to the true flow, and if $E < 0$ it is slow. A single estimate for the error in each simulation is calculated by spatially averaging the absolute value of E on each plane AGL and then averaging again to yield a column-averaged absolute error,

$$E_{\text{avg}} = \frac{\sum_{i=1}^{n} \overline{|E(z_i)|}}{n} \tag{3.14}$$

where n is the number of planes AGL, z_i is the height AGL of plane i, and $\overline{v}$ represents the horizontal spatial average of a variable v. The results of the grid resolution study are summarized in Figure 3.2, which shows E_{avg} calculated using $n = 10$ at 10 m intervals between 10 and 100 m AGL. This study focuses on the error resulting from the surface boundary condition, which is why E_{avg} is calculated over the bottom 100 m of the boundary layer.

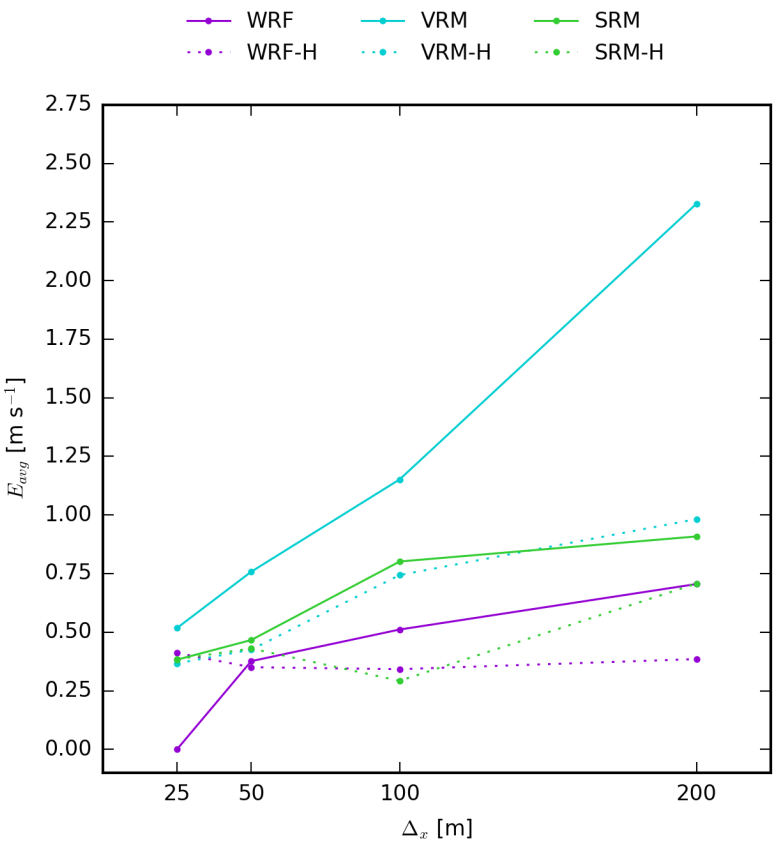

Figure 3.2: Summary of grid resolution study results, showing the average error E_{avg}, calculated from Equation 3.14, over the bottom 100 m AGL from the 24 simulations. The 24 simulation configurations are detailed in Table-3.1. Configurations include terrain-following WRF, IBM-VRM, and IBM-SRM. Each configuration is tested at four grid resolutions (25, 50, 100 and 200 m) with and without the hybrid RANS/LES scheme. Simulations with the hybrid RANS/LES scheme enabled are labeled with "-H".

With the hybrid RANS/LES scheme disabled, terrain-following WRF produces the lowest E_{avg} over the range of resolutions tested, with a maximum average error of roughly 0.7 m s^{-1} over the bottom 100 m AGL when $\Delta x = 200$ m. The performance of IBM-SRM follows a similar trend to native WRF, although its E_{avg} is higher by roughly 0.25 m s^{-1}. IBM-VRM displays the highest E_{avg} at all resolutions and the largest increase in E_{avg} as Δ_x is increased.

When the hybrid RANS/LES scheme is enabled, all three configurations display decreased error at all resolutions and $E_{\text{avg}} \approx 0.375$ m s^{-1} at $\Delta_x = 25$ m. Impressively, terrain-following WRF shows a relatively flat trend of E_{avg} with Δ_x. Both IBM-VRM and IBM-SRM yield lower E_{avg} when the hybrid RANS/LES scheme is enabled, with the lower error of the two IBM configurations produced by IBM-SRM at all resolutions.

The current topography is near to the slope limits imposed by terrain-following coordinates and, especially at the resolutions considered here, terrain-following coordinates are unlikely to be feasible for simulations over real topography. Based upon the simulations analyzed here, either of the IBM algorithms with the hybrid RANS/LES scheme would be an excellent configuration to use over complex terrain at 25 or 50 m resolution. If an IBM is necessary at more coarse resolutions of 100 or 200 m then the IBM-SRM with the hybrid RANS/LES scheme is recommended.

A more complete understanding of the differences between each simulation and the high-resolution solution as a function of grid resolution can be gained from Figure 3.3 which includes horizontal contour plots of E averaged across the 10 planes between 10 and 100 m AGL for each simulation configuration.

The errors associated with each configuration have similar patterns and generally increase in magnitude as grid spacing increases. All configurations display a positive wind speed bias near the summit of the idealized hill and a negative bias in the recirculation zone formed in the lee of the hill. Simulations with the IBM-VRM and the IBM-SRM show domain-wide errors that increase in magnitude as Δ_x is increased. These errors are likely related to the varying location of the intersection between the immersed boundary and grid. The IBM-VRM appears to be significantly more sensitive to the immersed boundary position than the IBM-SRM, especially at $\Delta_x = 200$ m, which has been previously observed in other studies (Bao et al. 2016; Bao 2018; Arthur et al. 2019). This sensitivity primarily results from interpolation errors due to increased physical distance between nearest neighboring grid points, and the increased distance of RPs from the IB, which can greatly influence the applicability of the log-law. Additionally, the larger aspect ratio used for the $\Delta_x = 200$ m grid may increase these errors.

Enabling the hybrid RANS/LES scheme generally yields a visible reduction in the magnitude of E everywhere except for the hill summit. Of the 24 simulations, those using IBM-VRM show the most pronounced improvements at all resolutions when the hybrid RANS/LES scheme is applied. In particular, the strong negative wind speed bias in the lee of the hill is nearly eliminated. At $\Delta_x = 100$ and 200 m, there is a negative wind speed bias everywhere except for the hill summit, which is greatly reduced when the hybrid RANS/LES scheme is enabled.

Enabling the hybrid RANS/LES scheme appears to cause a clear improvement to the IBM-VRM simulations at all resolutions. The cause of this dramatic improvement becomes clear when examining the inner workings of the IBM-VRM. By directly modifying velocities above the immersed boundary, the IBM-VRM reduces the effect of turbulent transfer of momentum on the near-surface velocities. This reduces momentum transport to the near-surface, which reduces wind speeds in regions where there is substantial mixing and downward transport of high-momentum flow from aloft, such as the lee of the hill. By enabling the hybrid RANS/LES scheme, the near-surface velocities are more strongly influenced, via an increase in ν_t, by the downward transport of momentum from aloft.

3.5 Summary and conclusions

Diagnosing and understanding the complexities of LES of the PBL is necessary for improving multiscale modeling efforts. Simulations of flow over an idealized hill were used to evaluate three bottom boundary conditions; that of the standard terrain-following WRF model and two immersed boundary methods (IBM-VRM and IBM-SRM). Simulations of each bottom boundary condition were evaluated at grid resolutions of 25, 50, 100 and 200 m. These grid resolutions were selected to observe the applicability of each bottom boundary condition at various grid resolutions, including resolutions within the turbulence gray zone. Even at high resolutions ($\Delta_x = 25$ m) the bottom boundary condition is found to have a large effect on the flow solution, especially in lee of the hill where recirculating flow develops. As the grid resolution is coarsened, there is an increase in the magnitude of differences between the flow solutions with different surface boundary conditions.

Additionally, the grid resolution sensitivity study was repeated with the hybrid RANS/LES scheme of Senocak et al. (2007), which modifies the near-surface eddy viscosity in an attempt to account for a decrease in the characteristic turbulence length scale near the bottom boundary. The hybrid RANS/LES scheme was found to improve simulations at all resolutions with the most pronounced improvement in those using the IBM-VRM.

The finest grid resolution used in this study was constrained by the available computational resources. If sufficient computational resources are available, future research should consider a wider range of grid resolutions, which will hopefully provide a more specific recommendation for grid resolutions at which it is recommended to use the hybrid RAMS/LES scheme. Because error decreases as the grid is refined, future studies should consider using a higher resolution specifically for the true simulation. With additional computing resources, this author would expand this study to use 10 m resolution for the true simulation and evaluate model performance at resolutions of 20, 40, 60, 80, 100, 150, 200, 250 and 300 m.

If this study is repeated and expanded then the hybrid VRM/SRM approach of Bao et al. (2018) should be considered. The hybrid IBM algorithm attempts to address the deficiencies of the individual methods by combining the VRM and SRM algorithms. With this approach, the near-surface velocities and stresses are jointly modified to maintain a log-law boundary condition. It should be noted that this hybrid IBM algorithm has shown improved performance relative to the individual VRM and SRM algorithms, however this new algorithm requires ghost-points and is thus incapable of being applied on a domain that is nested within a terrain-following parent domain.

The results of this study can be distilled into several "best practices" and observations. First, modelers should attempt to avoid the complexities introduced by an IBM for as long as the resolved topographic slopes remain tolerable by a NWP model's native terrain-conforming grid. Second, even at fine resolutions, modelers should take care when setting a bottom boundary condition because there are large differences between flow solutions with different surface boundary conditions as demonstrated by the simulations here with 25 and 50 m grid resolutions. Third, if the introduction of ghost points is not problematic then the IBM-SRM is recommended over the IBM-VRM algorithm because IBM-SRM produced lower

error regardless of the resolution. Finally, the hybrid RANS/LES scheme is recommended because it reduced the error of each configuration tested.

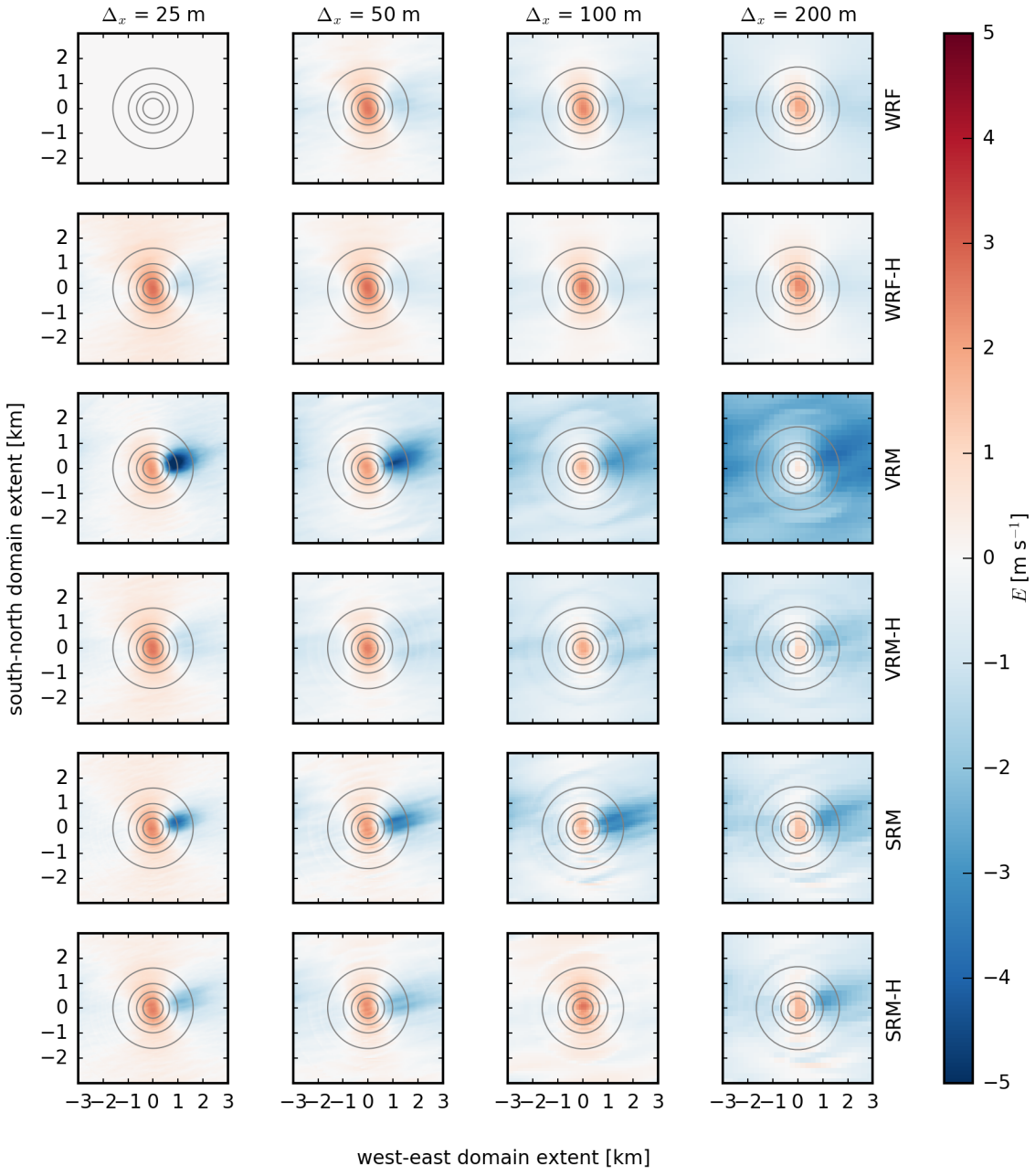

Figure 3.3: Error in three dimensional wind speed (E based on Equation 3.13) between terrain-following WRF, IBM-VRM, and IBM-SRM solutions with and without the RANS/LES hybrid scheme for grid resolutions of $\Delta_x = 25$, 50, 100 and 200 m as detailed in Table 3.1. Simulations with the hybrid RANS/LES scheme enabled are labeled with "-H".

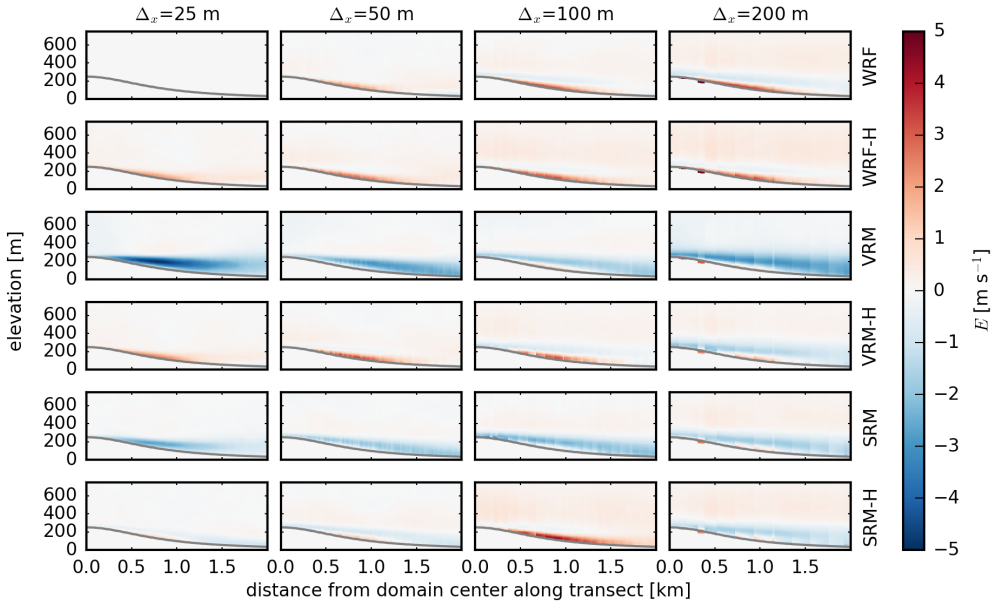

Figure 3.4: Error in the three dimensional wind speed (E based on Equation 3.13) along a transect through the modeling domain. E is shown from 6 simulations configurations each run at 4 resolutions (Δ_x = 25, 50, 100 and 200 m). The six configurations include terrain-following WRF, IBM-VRM and IBM-SRM, each with and without the hybrid RANS/LES scheme. The profiles are oriented along a transect angled at 75° clockwise from north and passing through the domain center (i.e. hill summit). Simulations with the hybrid RANS/LES scheme enabled are labeled with "-H".

Chapter 4

Investigation and comparison of turbulence represented in microscale and multiscale simulations

4.1 Introduction

Many applications for high resolution numerical weather prediction (NWP) are complicated by transient meteorological conditions or phenomena that span a wide range of spatial scales from centimeters to kilometers. Accurate downscaling of time-varying mesoscale ($\Delta x > 1$ km) meteorological data to microscale resolutions ($\Delta x < 10$ m) has recently been shown to improve microscale resolution simulations of scalar transport in an urban environment (Wiersema et al. 2020). While these simulations (see Chapter 2) demonstrated the importance of downscaling, they also highlight the associated difficulties.

As named by Wyngaard (2004), the terra incognita, also called the turbulent gray zone, is a range of spatial scales where planetary boundary layer turbulence parameterizations (i.e. PBL schemes) and large-eddy simulation (LES) turbulence closure models are both ill suited. This problem arises due to the assumption that a domain using a PBL scheme is coarse enough that negligible turbulent motions are resolved and that a domain using an LES closure has high enough resolution that the majority of the turbulent energy spectra is resolved. Multiscale modeling necessitates the transition from coarse resolutions using a PBL scheme to fine resolutions using a LES closure. Simulating and downscaling through these intermediate resolutions is a major challenge for multiscale modeling.

Predictions of transport and mixing require the accurate representation of turbulence, especially for flows over complex terrain. Wiersema et al. (2020) demonstrated that compared to a microscale-only simulation, a multiscale simulation might show weaker agreement with wind field observations but improved predictions of transport and mixing. It is hypothesized that this results from large-scale meteorological forcing and turbulence that is only downscaled and resolved in the multiscale simulation. In LES, it is possible that “mean

velocity profiles are sometimes well predicted, while the turbulence quantities may be under or over-predicted by a factor of two" (Ferziger and Perić 2002, p. 337). With this in mind, the goal of this study is to to improve microscale predictions for transport and mixing over complex topography by understanding and improving the representation and downscaling of turbulence within a multiscale model.

Depending on the study, the forcing applied to microscale NWP simulations can vary greatly in complexity. The most basic forcing methodology is to enforce a fixed atmospheric state, such as neutral and dry with a logarithmic velocity profile, at the inflow lateral boundaries and an open condition at the outflow lateral boundaries; see Chan and Leach (2007) for an example using the FEM3MP model. Steady inflow conditions are problematic for LES because a significant distance from the inflow boundaries (i.e. fetch) is required for turbulence to develop.

A common method of providing turbulent inflow is to develop turbulence within a coarse resolution simulation with periodic boundary conditions. This periodic domain can be tuned by adjusting the forcing such that it provides the desired inflow conditions to the nested domain of interest; see Sullivan et al. (1996) and Golaz et al. (2009). A disadvantage of this nested approach is that tuning requires *a priori* meteorological knowledge (i.e. local observations). Additionally, the resolved turbulent scales are restricted by the extent of the parent domain and this configuration does not include the effects of regional or mesoscale meteorology.

Coupling of mesoscale NWP and microscale models allows for regional and mesoscale effects to influence a LES, which has been shown to improve simulations of transport and mixing in urban areas (Park et al. 2015; Li et al. 2018). Because mesoscale NWP models produce smooth velocity fields, relative to an LES, the downscaled meteorology is often modified to include synthetic turbulence or turbulence extracted from a precursor LES simulation. Running multiple models in sequence adds significant complexity to the simulation. Additionally, the coupling approach only downscales what is resolved by the mesoscale NWP. This coupled model approach does not resolve meteorological phenomena, including turbulence, with scales smaller than that resolved in the mesoscale NWP but larger than those resolved in the LES.

The multiscale modeling approach of Wiersema et al. (2020) provides a downscaling methodology for providing a LES with turbulent forcing that includes regional and mesoscale meteorology. Additionally, this methodology does not require *a priori* knowledge but instead downscales a meteorological forecast product. Downscaling is performed through a telescoping series of nested domains with grid resolutions that range between the mesoscale and microscale. In this way, the highest resolution domain is supplied forcing that includes meteorological features and turbulence from all scales that are resolved within the telescope of nested domains.

In this study we evaluate a modified configuration of the multiscale simulation from Wiersema et al. (2020) with a specific focus on the representation of turbulence in the highest resolution domain. As in Wiersema et al. (2020), we simulate transport and mixing of a tracer gas (SF_6) released during the Joint Urban 2003 field campaign (JU2003) in the central

business district of Oklahoma City, OK. Section 4.2 includes details of the JU2003 field campaign. Our multiscale configuration is comprised of six nested domains with horizontal resolutions ranging between 4.95 km and 2 m. Initial conditions and mesoscale forcing are supplied by the North American Regional Reanalysis (NARR) (Mesinger et al. 2006).

This multiscale simulation is evaluated both with and without the cell perturbation method (CPM) of Muñoz-Esparza et al. (2015), which is detailed in Section 4.3. The CPM introduces small temperature perturbations along the inflow boundaries that follow a grid refinement. These perturbations promote the development of turbulence and are applied here when transitioning from a coarse resolution domain with a PBL scheme to a fine resolution domain using a LES turbulence closure model.

Two multiscale simulations (with and without the CPM) are compared to a microscale-only simulation with periodic lateral boundary conditions and forcing that is tuned using local observations. The microscale-only configuration is representative of traditional computational fluid mechanics simulations, such as the configurations used in previous JU2003 simulations by Chow et al. (2008), Golaz et al. (2009), Lundquist et al. (2012) and Bao et al. (2018). Sections 4.4 and 4.5 include comprehensive details about the microscale-only and multiscale configurations, respectively.

Performance of the three simulations (microscale-only, multiscale and multiscale CPM) is qualitatively evaluated in Section 4.6 and quantitatively evaluated in Sections 4.7 and 4.8 by comparing the simulations to observations of meteorological conditions and tracer gas concentrations during JU2003. These comparisons include statistical measures of model skill for the prediction of wind speed, wind direction, tracer concentration and turbulence kinetic energy. Additionally, spectra of turbulence kinetic energy are analyzed and compared to sonic anemometer observations.

4.2 Joint Urban 2003 Field Campaign

The Joint Urban 2003 (JU2003) atmospheric dispersion study in Oklahoma City, Oklahoma was led by the Defense Threat Reduction Agency (DTRA) and the U.S. Department of Homeland Security (DHS) with the objective of investigating flows downwind of tall buildings and in street canyons and tracer dispersion around and downwind of tall buildings. A detailed overview of the study can be found in (Allwine and Flaherty 2006).

Numerous and extensive simulations have been performed using models of varying degrees of fidelity and a focus on urban meteorology and tracer dispersion within the central business district of Oklahoma City during the JU2003 intensive observational periods (IOPs). Hanna et al. (2011) compared results from four diagnostic urban wind flow models coupled with Lagrangian particle dispersion models (LPDMs) applied to IOP 8. Burrows et al. (2007) applied a Reynold's-averaged Navier-Stokes (RANS) model with a k-ω turbulence model to five JU2003 tracer releases. Gowardhan et al. (2011) also applied a RANS model, QUIC-CFD, to IOP 8 and compared these results to a diagnostic wind flow model. Chan and Leach (2007) and Lundquist et al. (2012) ran large-eddy simulations of IOP 3 using the

FEM3MP and the WRF-IBM models, respectively, with initial conditions and boundary conditions specified using a one-dimensional vertical wind profile synthesized from JU2003 observations. Li et al. (2018) initialized and forced a large-eddy simulation of IOP 3 using a precursor mesoscale simulation modified with a diagnostic turbulence reconstruction scheme. Most recently, Wiersema et al. (2020) simulated the first continuouse tracer release of IOP 3 using a multiscale simulation consisting of six nested domains that transition between the mesoscale and microscale.

Several datasets of observations from JU2003 are used in this study for initializing and forcing the microscale-only simulation and also for analyzing model performance and the simulations' skill. Observations used in this study include a sonic anemometer at the SF_6 release location that was deployed by the Field Research Division of the NOAA Air Resources Laboratory (ARL-FRD), a SODAR deployed by Argonne National Laboratory (ANL) in the botanical gardens located to the south-west of the SF_6 release location, 11 portable weather information display stations (PWIDS) with propeller and vane anemometers and 15 Super PWIDS with sonic anemometers deployed by the Dugway Proving Grounds (DPG), 20 programmable integrating gas samplers (PIGS) deployed by NOAA ARL-FRD, and 19 "bluebox" integrating gas samplers deployed by Lawrence Livermore National Laboratory (LLNL). The LLNL bluebox gas samplers are sited, relatively, near the SF_6 release location, and the ARL-FRD gas samplers are sited further afield.

Structures within the central business district are represented using an immersed boundary method (IBM) in the highest resolution domain of each simulation. Details of the IBM are included in Chapter 2 and Wiersema et al. (2020). Height of the immersed boundary is specified by sampling a LiDAR dataset of building geometries in the central business district of Oklahoma City, OK. Some manual adjustments are applied to the LiDAR dataset, especially near concave geometries, to ensure high quality interpolations for the IBM. Additionally, structures located near the southern domain boundary are removed to prevent nonphysical flow effects that could develop as a result of the inflow not including the effects of these buildings. Finally, two elevated walkways are removed because the IBM implementation does not currently allow for void space, such as the gap beneath the walkways. The processed urban geometry is shown in Figure 4.1a. Grid points where manual adjustments were made are shown in Figure 4.1b.

4.3 The cell perturbation method

In nested multiscale models, traversing the turbulence "gray zone" involves the transition from a planetary boundary layer (PBL) scheme used on coarse resolution domains to a large-eddy simulation (LES) turbulence closure model used on high resolution domains. In contrast to turbulent flow resolved in a high resolution LES, the flow on coarse resolution domains using a PBL scheme is smooth with minimal resolved turbulence. When a LES domain is nested within a parent domain using a PBL scheme the nested LES domain requires a prohibitively long distance to fully develop turbulence (i.e. fetch) (Mirocha et al.

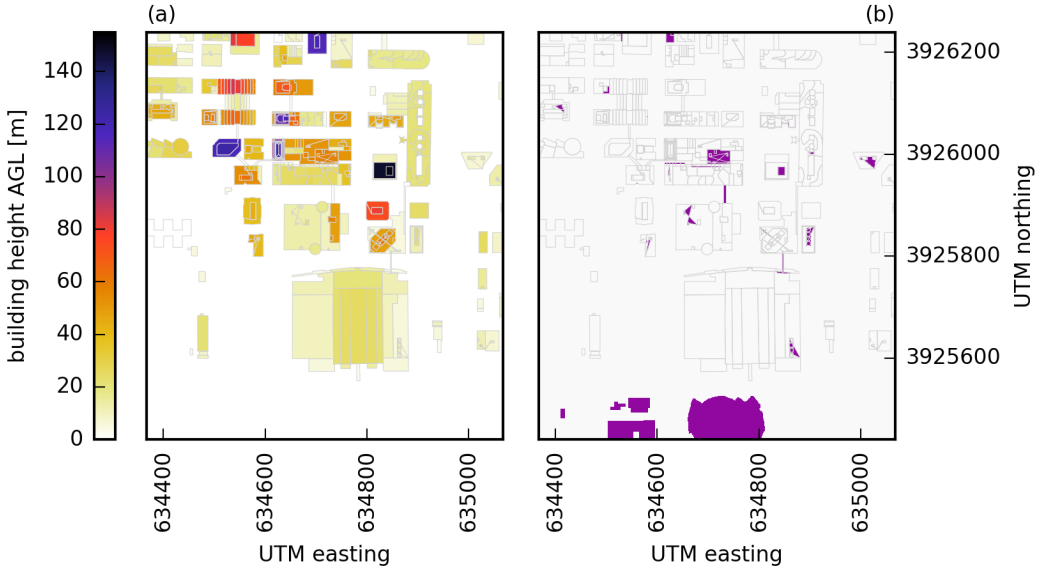

Figure 4.1: (a) Building geometries and heights above ground level that are used to specify the immersed boundary height within the $\Delta = 2$ m domain and (b) grid points where the building geometry was manually modified to a value different than that of the LiDAR dataset.

2013). The cell perturbation method (CPM) (Muñoz-Esparza et al. 2014, 2015; Muñoz-Esparza and Kosović 2018) greatly reduces the fetch necessary for turbulence development by introducing small temperature perturbations along the lateral inflow boundaries. The CPM has previously been demonstrated to improve LES simulations of flow over complex urban terrain by Lee et al. (2019), which used the CPM to develop turbulence in a microscale-only simulation forced using fixed inflow velocity profiles.

Potential temperature perturbations are applied on patches of 8×8 grid points in the horizontal dimensions and patches of 2 grid points in the vertical dimension up to a specified distance in the horizontal and vertical. These dimensions were selected to be large enough that they would not be quickly dissipated by the WRF model. As discussed in Muñoz-Esparza et al. (2014), the WRF model's finite difference schemes introduce numerical diffusion that rapidly dissipates energy for $k \gtrsim 2\pi/6\Delta x$ (Skamarock 2004; Knievel et al. 2007). Perturbations are applied three patches (24 grid points) inward from the boundary if the predominant flow in the PBL along the boundary is directed into the high-resolution domain. Perturbations are not applied if the predominant flow in the PBL along a boundary is directed outward from the high-resolution domain.

Following Muñoz-Esparza et al. (2015), the perturbation magnitudes for each patch are randomly assigned with a uniform distribution and a maximum amplitude calculated based

on the relative strength of advective and buoyant forcing that are represented by a perturbation Eckert number,

$$Ec = \frac{U_g^2}{c_p \tilde{\theta}_{pm}} \tag{4.1}$$

where $\tilde{\theta}_{pm}$ is the maximum perturbation amplitude, c_p is the specific heat capacity at constant pressure, and U_g is the geostrophic wind speed. This procedure differs from that of Muñoz-Esparza et al. (2015) in that U_g is calculated as the horizontal domain-averaged wind speed at a height of 1.1 times the maximum height of the PBL within the domain. Rather than diagnosing a PBL height from the mesoscale domains, the simulations here use a constant PBL height of 500 m and Ec =0.2.

The timescale at which perturbations are recalculated, Γ, is determined by approximating the time required for the mean flow to traverse a horizontal distance of three patch lengths. Γ varies only in the vertical dimension. Calculation of Γ at vertical index k begins with a domain-average of u and v velocities at the topmost vertical grid level in the patch, yielding $\overline{u_k}$ and $\overline{v_k}$. Next, the perturbation timescale is calculated as

$$\Gamma_k = \frac{pn\Delta}{(\overline{u_k}^2 + \overline{v_k}^2)^{\frac{1}{2}} \cos(\phi_k)} \tag{4.2a}$$

$$\phi_k = \min\left(\theta_k, \frac{\pi}{2} - \theta_k\right) \tag{4.2b}$$

$$\theta_k = \arctan\left(\frac{|\overline{u_k}|}{|\overline{v_k}|}\right) \tag{4.2c}$$

where p is the number of patches extending inward from the boundary, n is the number of horizontal grid points per patch, and Δ is the horizontal grid resolution.

Since Γ_k depends upon the vertical grid level, meteorological variables (i.e. velocities), and grid variables (i.e. resolution, patch sizes, and number of patches) it is difficult to provide a typical value. For reference, if considering a case with $p = 3$ patches, $n = 8$ grid points per patch, $\Delta = 30$ m and $\overline{u_k} = \overline{v_k} = 7$ m s^{-1}, then $\Gamma_k \approx 100$ s.

4.4 Microscale-only configuration

The microscale-only simulation in this study uses a two-domain nested configuration with horizontal grid resolutions of 10 and 2 m and closely follows the setup of Wiersema et al. (2020). The parent 10 m domain has periodic lateral boundary conditions and is allowed to "spin up" for 6 hours and 50 minutes prior to the initialization of the 2 m domain. This two-domain configuration has the advantage of providing turbulent inflow to the 2 m simulation. Due to the simplified nature of the microscale-only simulation, it is necessary for the modeler to specify idealized initial conditions and forcing for the 10 m domain.

Initial conditions are specified as neutral and dry with a velocity profile that is constructed from local observations recorded near the SF_6 release location during the JU2003 field campaign. These observations include the ANL miniSODAR, DPG PWIDS 10 and 11, DPG super PWIDS 17 and 20, and the NOAA ARL-FRD sonic anemometer sited at the release location. Data from each of these instruments is temporally averaged over the 30 minute SF_6 release period. Near-surface velocities are set using the ARL-FRD sonic anemometer for 2 m AGL and an average of the four DPG stations for 8 m AGL. The ANL miniSODAR observations are used to set velocities between 15 and 135 m AGL. Velocities at 135 m AGL are maintained until reaching the model top, which is approximately 400 m AGL in the microscale-only simulation.

Forcing is applied by the addition of a uniform pressure gradient throughout the 10 m and 2 m domains. The magnitude of this pressure gradient is tuned to maintain agreement between velocities in the 2 m domain and JU2003 observations, specifically the observed velocity profile that is also used as initial conditions. As is common with microscale simulations, this configuration does not include transient forcing or the effects of regional meteorology.

4.5 Multiscale configuration

The multiscale model configuration uses six nested domains with horizontal resolutions of 4.95 km, 1.65 km, 330 m, 30 m, 10 m and 2 m. Positions of the six domains are shown in Figure 4.2. For this set of simulations, since the predominant wind direction on the LES domains is consistent and known, the 10 m and 2 m domains are positioned in the north-east quadrant of their respective parent domains such that the "fetch" distances between inflow boundaries of the nested domains is increased versus a centered arrangement of the domains.

There are slight differences between the multiscale configuration used here and the configuration from Wiersema et al. (2020) and Chapter 2. The primary change is switching from five domains with resolutions of 6050, 550, 50, 10 and 2 m to six domains with resolutions of 4950, 1650, 330, 30, 10 and 2 m. The multiscale simulation from Wiersema et al. (2020), specifically the 50 m domain, produced elongated flow structures and few small-scale structures, which is common in coarse resolution LES using the Smagorinsky turbulence closure model (Hutchins and Marusic 2007; Ludwig et al. 2009; Kirkil et al. 2012). The updated domain configuration uses 30 m resolution for the first LES domain, which was chosen to reduce the prominence of the elongated flow features.

The outermost (4.95 km) domain is initialized and forced by the NCEP North American Regional Reanalysis (NARR) dataset (Mesinger et al. 2006). Unlike the microscale-only simulation, the multiscale simulation does not use JU2003 observations. By only relying on a meteorological forecast product, such as the NARR dataset, the multiscale configuration is running as a "forecast" and, if computational resources were significantly more powerful, the simulation could be used in a predictive capability.

The computational burden of the multiscale simulation is reduced by staggering the start times of each nested domain, which allows for development of the flow within a parent prior

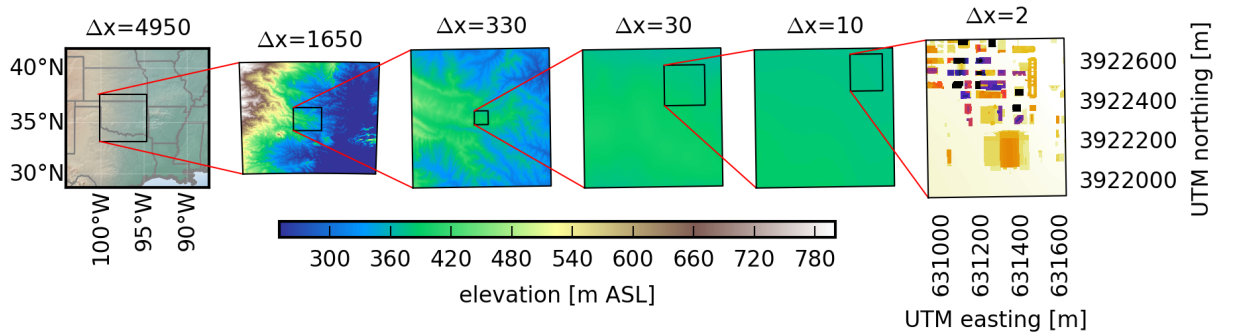

Figure 4.2: Positioning of grids in the six-domain multiscale model configuration. A map showing state boundaries is overlaid on the 4.95 km domain. Contours of ground elevation above sea level are shown on the 1.65 km, 330 m, 30 m, and 10 m domains. The 2 m domain uses a different colorbar and is overlaid with contours of surface elevation, including buildings, as resolved within the simulation.

to initializing a child domain. This spin-up time is crucial as it allows for each domain to advance sufficiently beyond the initial conditions and develop features of scales not resolved in the initial flow field or the corresponding parent domain. Beginning with the 4.95 km domain, the six domains have start times of 0300, 0600, 0900, 1200, 1500, and 1550 UTC. The simulation is terminated at 1630 UTC, corresponding to the shutoff of the SF_6 release.

Terrain-following coordinates and the standard WRF bottom boundary conditions are used on the 4.95 km, 1.65 km, 330 m and 30 m domains. The velocity reconstruction immersed boundary method is used on the 10 m and 2 m domains with a constant roughness length $z_0 = 0.1$ m. The Mellor-Yamada-Janjic planetary boundary layer scheme is enabled on 330 m domain and its parents. At LES resolutions (30 m, 10 m, and 2 m), the three-dimensional Smagorinsky turbulence closure scheme is used with a coefficient $C_s = 0.18$. Additional details on the multiscale simulation configuration are included in Table 4.5.

As with the microscale-only configuration, the vertical levels of each domain are carefully controlled. A model top of 200 hPa is used for all domains in the multiscale configuration. Because this covers approximately 30 times the vertical extent of the microscale-only simulation, substantially more vertical grid levels are necessary for the 10 m and 2 m domains relative to their counterparts in the microscale-only simulation. Near-surface vertical grid levels for the 10 m and 2 m multiscale domains are selected to match, as closely as possible, the vertical grid levels from the microscale-only configuration. Above 400 m AGL, which is the height of the model top of the microscale-only configuration, the vertical grid levels are stretched in height at a constant rate of $(z_{k+1} - z_k) / (z_k - z_{k-1}) = 1.05$. This aggressive stretching greatly reduces the computational costs but results in highly stretched grid cells with small aspect ratios (Δ_x/Δ_z ¡ 1) near the model top. Any error associated with poor grid quality is restricted to the topmost levels of the 10 and 2 m domains, where it does not

Table 4.1: Six-domain multiscale model configuration for JU2003 simulations. TF = terrain-following coordinate. IBM = immersed boundary method. MYJ = Mellor-Yamada-Janjic planetary boundary layer turbulence parameterization. Smag = 3D Smagorinsky turbulence closure scheme. WSM3 = WRF Single-Moment 3-class microphysics scheme. RRTM = Rapid Radiative Transfer Model longwave radiation model. KF = Kain-Fritsch cumulus parameterization.

	D1	D2	D3	D4	D5	D6
Δx , Δy [m]	4950	1650	330	30	10	2
Start Time [UTC]	0300	0600	0900	1200	1500	1550
Coordinate	TF	TF	TF	TF	IBM	IBM
Time Step [s]	30	10	2	$\frac{1}{5}$	$\frac{1}{15}$	$\frac{1}{75}$
East-West Grid Points	301	301	311	342	301	351
South-North grid Points	301	301	311	342	301	401
Bottom-Top Grid Points	51	51	96	121	146	243
Tell Perturbation Method	-	-	-	enabled	-	-
Turbulence	MYJ	MYJ	MYJ	Smag	Smag	Smag
Micro-Physics	WSM3	WSM3	WSM3	none	none	none
Longwave Radiation	RRTM	RRTM	RRTM	RRTM	none	none
Shortwave Radiation	Dudhia	Dudhia	Dudhia	Dudhia	none	none
Surface Layer Scheme	MM5	MM5	MM5	MM5	none	none
Land Surface Model	Noah	Noah	Noah	Noah	Noah	Noah
Cumulus Parameterization	KF	KF	none	none	none	none

affect the near-surface flow.

4.6 Qualitative analysis of simulation results

A visual comparison of the simulation results reveals several noteworthy differences in the predictions of SF_6 concentrations and turbulence kinetic energy (TKE). Figure 4.3 includes horizontal contours at 2.5 m AGL of SF_6 concentrations that are time-averaged over the 30 minute release period. The plumes from both multiscale simulations are significantly less constrained than that in the microscale-only simulation. This increased width of the multiscale plumes is due to oscillations in the inflow of the 2 m domain that are not replicated when using the idealized forcing of the microscale only configuration. Visually, the multiscale simulations show improved agreement with the observations, especially at sensors west of the SF_6 release location.

Transport of SF_6 upwind, relative to the predominant flow direction, from the SF_6 release location is also seen in both multiscale simulations. This upwind transport does not appear in the microscale-only simulation because it results from the downscaling of flow variability

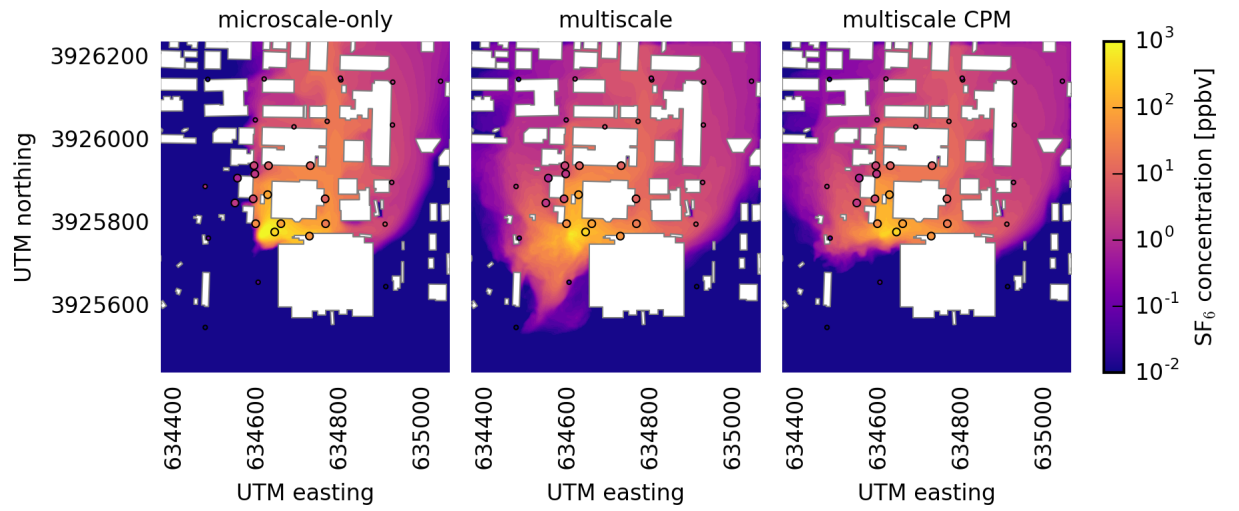

Figure 4.3: Horizontal contours of SF_6 concentrations at 2.5 m above ground level time-averaged over the SF_6 release window (1600-1630 UTC) from the microscale-only, multiscale and multiscale with CPM simulations. Concentration observations are overlaid as filled circles with the larger markers corresponding to the LLNL bluebox gas samplers and small markers the NOAA ARL-FRD gas samplers.

from the intermediate resolution domains. Intermittent periods of near-zero wind speed and highly variable wind direction occur at the SF_6 release location in both multiscale simulations and in the JU2003 observations (see Figure 10 in Wiersema et al. 2020). It is during these intermittent periods that coherent flow patterns may induce substantial upwind transport of the SF_6 plume. When the CPM is enabled, the additional small-scale turbulence generated in the 30 m domain helps to break apart these coherent flow patterns, which results in a reduction in the upwind transport. The extent of upwind transport in the three simulations is evident when comparing the time-averaged plumes shown in Figure 4.3.

The resolved TKE within each simulation is determined using Equation 4.3 with the perturbation velocity components calculated by subtracting a 10 minute rolling average from each velocity component time series:

$$q^2 = \frac{1}{2}\left(u'^2 + v'^2 + w'^2\right) \tag{4.3}$$

At Super PWIDS locations, the three velocity components are output at each model time step; $\frac{1}{75}$ s for the 2 m domain. Due to hardware limitations, velocities at every model time step are only saved at the grid points nearest to a Super PWIDS and the six adjacent grid points (north, south, east, west, above and below). Because a single grid point may not be the best choice for representing a real-world station, the TKE is calculated at each Super PWIDS as the average of TKE in the seven grid point cluster. Calculations of TKE at locations other

than the Super PWIDS stations, such as the horizontal contours of TKE in Figure 4.5 and vertical profiles of TKE in Figure 4.6a, are performed using simulation history files with a 3 s output interval. Due to difference in the spatial averaging and temporal resolution of the velocity fields, small variations are expected between TKE calculated with the two data sources.

To verify that the two data sources result in a comparable estimate of TKE, we calculate TKE along vertical profiles at the ANL miniSODAR and DPG PWIDS 03 using both data sources from the multiscale CPM simulation, which is shown in Figure 4.4. TKE calculated with the two data sources is compared at 20 grid points per vertical profile, which yields a mean absolute difference of 0.11 m^2 s^{-2} and a standard deviation of the absolute differences of 0.14 m^2 s^{-2}. At each grid point evaluated, the percent difference between TKE calculated with different data sources is found as the ratio of the absolute difference and average of the TKE calculations. For the two profiles evaluated, the average percent difference is 2.5%, which lends confidence in the calculations of TKE using simulation history files with the lower temporal resolution of 3 s.

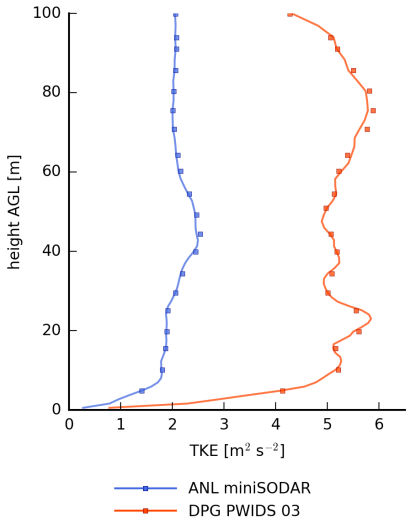

Figure 4.4: Vertical profiles of TKE from the Δ=2 m domains above the ANL miniSODAR and DPG PWIDS 03. The dotted lines represent TKE calculated using simulation history files with a 3 s output interval. Square markers represent TKE calculated using output at every model time step. The profiles have been time-averaged over the 30 minute SF_6 release period between 1600 and 1630 UTC.

A similar spatial pattern of resolved TKE is produced by all three simulations, which can be seen in the horizontal contours of time-averaged resolved TKE at 8 m AGL in Figure 4.5. Regions of elevated TKE develop throughout the simulation and are pronounced where buildings obstruct the flow and channel it through narrow gaps (see coordinates 634500, 3926000

in Figure 4.5), at the intersection of street canyons (see coordinates 634850, 3925900), and in the lee of tall buildings (see coordinates 634850, 3926050). Both multiscale simulations resolve more TKE compared to the microscale-only simulation. Qualitatively, the microscale-only simulation appears to underestimate TKE compared to the DPG Super PWIDS and the multiscale simulations show improved visual agreement. This visual analysis is confirmed by the model skill metrics for TKE that are discussed in the following section.

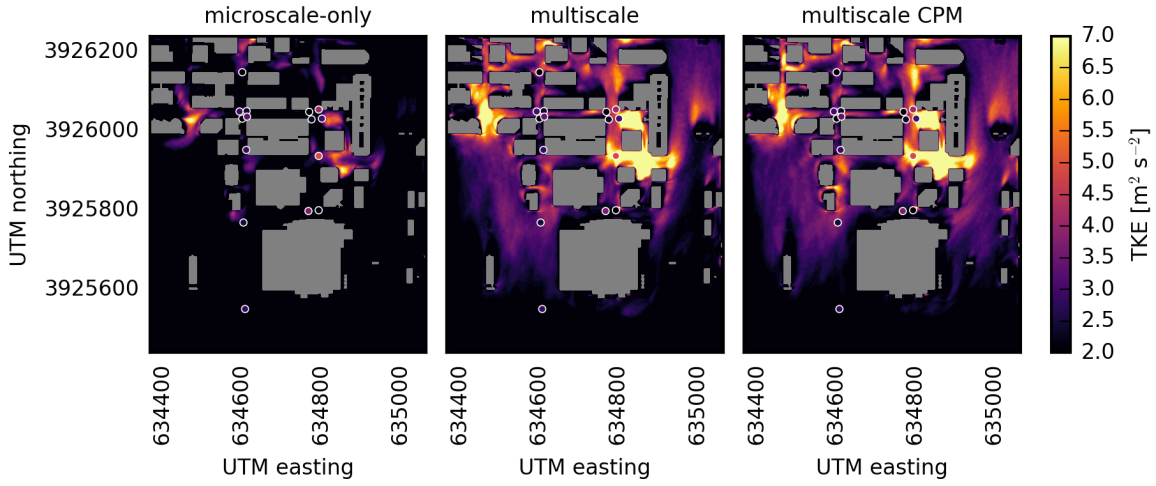

Figure 4.5: Horizontal contours of resolved TKE at 8 m above ground level time-averaged over the SF_6 release period (1600-1630 UTC) from the microscale-only, multiscale and multiscale with CPM simulations. TKE calculated from the DPG Super PWIDS observations is overlaid using filled circles. Contours of TKE are calculated using simulation history files.

Figure 4.6a shows vertical TKE profiles along a transect between the ANL miniSODAR and DPG PWIDS 03. This transect was selected to loosely follow the predominant wind direction, pass near the SF_6 release location and provide a transition from the inflow and outflow of the 2 m domain. The location of each vertical profile within the 2 m domain is shown in Figure 4.6b. As seen in Figure 4.5, the three simulations produce similar shape profiles with different magnitudes. In each vertical profile, the microscale-only simulation resolves less TKE than the multiscale simulations. Generally, the multiscale simulations produce similar profiles; however, enabling the CPM generally causes a slight increase in TKE, especially in the lee of buildings.

Figure 4.6c shows the overlaid TKE profiles from the multiscale CPM simulation with the color of each profile corresponding to the associated marker in Figure 4.6b. When advancing along the transect from south to north, there is an increase in the maximum height that TKE is influenced by the buildings. In these simulations, the region upwind of the inflow

boundaries consists of single story structures and parking lots. If taller structures were present upstream of the inflow then the 2 m domain would need to be expanded to ensure sufficient distance over which the flow can develop prior to reaching the SF_6 release location.

4.7 Statistical analysis of model skill

Measures of model skill proposed by Chang and Hanna (2004) and Calhoun et al. (2004) are used to compare the predictions of each simulation to JU2003 observations. These measures model skill have been applied to numerous previous studies, including several JU2003 simulations (Burrows et al. 2007; Chan and Leach 2007; Chow et al. 2008; Hanna et al. 2011; Lundquist et al. 2012; Wiersema et al. 2020). Six model skill scores are used in this study: the fraction of predictions within a factor of x (FACx); fractional bias (FB); geometric mean bias (MG); geometric variance (VG); normalized mean squared error (NMSE); and scaled average angle (SAA).

$$\text{FACx} = \text{fraction of data that satisfies} 1/x \leq X_p/X_o \leq x \tag{4.4a}$$

$$\text{FB} = 2\left(\overline{X_o} - \overline{X_p}\right) / \left(\overline{X_o} + \overline{X_p}\right) \tag{4.4b}$$

$$\text{MG} = \exp\left(\overline{\ln\left(X_o\right)} - \overline{\ln\left(X_p\right)}\right) \tag{4.4c}$$

$$\text{VG} = \exp\left(\overline{\left(\ln\left(X_o\right) - \ln\left(X_p\right)\right)^2}\right) \tag{4.4d}$$

$$\text{NMSE} = \overline{\left(X_o - X_p\right)^2} / \left(\overline{X_o}\ \overline{X_p}\right) \tag{4.4e}$$

$$\text{SAA} = \Sigma\left(|U_i||\phi_i|\right) / \left(N|\overline{U_i}|\right) \tag{4.4f}$$

In the above equations, X_o is the set of observational data and X_p are the corresponding predictions from a simulation, N is the number of observations, ϕ_i is the difference between observed and predicted wind directions, and $|U_i|$ is the predicted wind speed. Values for X_o and X_p are time-averages over the 30 minute release period. An overbar indicates averaging of all locations.

Skill scores evaluating wind speeds, direction and SF_6 concentrations predicted by the microscale-only and multiscale simulations are graphically represented in Figure 4.7. These skill scores are comparable with those from the 5-domain multiscale setup reported in Chapter 2 and in Wiersema et al. (2020) where it was observed that microscale-only simulations performed best at predicting wind speeds and a multiscale simulation performed best at predicting SF_6 concentrations. It is not surprising that the microscale-only simulation, the only simulation with forcing based upon local JU2003 observations, would perform best at prediction of wind speed and direction. The microscale-only simulation was provided inflow that was tuned to ensure agreement with local observations, whereas the multiscale simulations were provided a meteorological forecast product with a horizontal resolution of 32 km. Another perspective is that the 2 m domain's entire footprint could fit approximately 18000 times within a single grid cell of the NARR data!

Each simulation yields negative FB scores for wind speed, which indicate that all simulations overestimate near-surface wind speeds. We hypothesize this is due to the absence of drag induced by buildings in the intermediate resolution domains and also due to missing small-scale sources of drag in the 2 m domain, such as vegetation and architectural features. Enabling the CPM results in a further decrease in the FB score, which is likely due to increased vertical mixing that transports high momentum flow from aloft towards the surface. Overall, the microscale-only simulation displays the highest model skill for predicting wind speeds and direction, followed by the multiscale simulation and the multiscale CPM simulation.

Similar to the simulations from Chapter 2 and Wiersema et al. (2020), the multiscale simulation outperforms the microscale-only simulation at predicting SF_6 concentrations. Compared to the microscale-only simulation, the multiscale simulations show improved skill for every metric evaluating prediction of both SF_6 and TKE. Enabling CPM results in a slight decrease in the model skill scores for the prediction of SF_6 and TKE.

The microscale-only simulation's large and positive FB score indicates a substantial underestimate of TKE. The upper limit of turbulence length scales supported on the microscale-only simulation's 10 m domain may be partly responsible for the underestimation of TKE. The multiscale simulations develop energetic, large-scale, coherent flow structures in the domains with 30, 330, and 1650 m horizontal resolution, which the microscale-only simulation is unable to reproduce. Analysis of TKE spectra is performed in the following section to investigate the scales of motions resolved by the different simulations.

Overall, both multiscale simulations overestimate TKE but the magnitude of this error is less than the underestimate by the microscale-only simulation. Enabling CPM increases the overestimation of TKE and results in slightly reduced model skill for both TKE and SF_6. Both multiscale simulations show improved model skill at predicting SF_6 and TKE compared to the microscale-only simulation.

4.8 Spectral analysis of turbulence kinetic energy

Spectral analysis of TKE is used to investigate differences in the forcing between the microscale and multiscale simulations as well as the effects of the CPM. Energy spectra are calculated following Equation 4.5 where $\mathcal{F}(x)$ represents the discrete Fourier transform of series x.

$$E(\omega) = \frac{1}{2}\left(|\mathcal{F}(u')|^2 + |\mathcal{F}(v')|^2 + |\mathcal{F}(w')|^2\right) \tag{4.5}$$

DPG Super PWIDS 17 (SP17), located 8 m AGL at the SF_6 release location, is well sited to observe flow with relatively unobstructed upstream conditions. SP17 is the most reliable observation of unobstructed flow leading into the central business district because directly upwind from the sonic anemometer are botanical gardens, single story structures and parking lots. TKE spectra at SP17 calculated using the sonic anemometer observations

and the three simulations are shown in Figure 4.8. The TKE spectra of SP17 observations displays excellent agreement with the expected $-\frac{5}{3}$ power law scaling in the inertial subrange.

Compared to the microscale-only simulation, the multiscale simulation has improved agreement with SP17 within the inertial subrange, particularly at frequencies greater than 0.05 s^{-1}. This extension of the resolved inertial subrange within multiscale simulations is due to the energetic low-frequency motions generated on the intermediate resolution domains. When downscaled and allowed to develop on a higher resolution domain, these large-scale motions break down into smaller, higher frequency motions. While the microscale-only simulation receives fully developed turbulent flow at the lateral boundaries of the 2 m domain, the 10 m parent domain does not resolve the larger scales of turbulence that are generated and downscaled using the telescoping grids of the multiscale simulation.

Both of the multiscale simulations overestimate the energy in large-scale motions at frequencies lower than 0.05 s^{-1}. This overestimation may be the result of persistent large-scale structures in the flow that are not realistically cascading into smaller scale motions. The use of a more sophisticated LES turbulence closure model, such as the dynamic reconstruction method (Chow et al. 2005; Chow and Street 2009), might help to reduce this buildup of energy in the large scales. In the LES domains, extending the "fetch", the distance between the inflow boundaries and grid refinement interfaces, may also improve the results by providing additional time for the flow to develop smaller scales of turbulence prior to downscaling. Configuring a multiscale simulation requires striking a difficult-to-optimize balance between the simulation's computational costs, the resolution and extent of each grid, and the degree of physical accuracy that can be expected. The sensitivity of terrain-following coordinates and different IBM algorithms to grid resolution for simulations over complex terrain is explored in Chapter 3, however significantly more research is required before any "best practices" can be decisively stated.

Enabling the CPM in the multiscale simulation results in a clear increase in the energy resolved at frequencies greater than 0.04 s^{-1}. As expected, the CPM promotes the development of turbulence on the 30 m domain and highly energetic turbulent features that develop on the 30 m domain are then downscaled through the 10 m domain and into the 2 m domain, where they are a major contributor to the increase in resolved TKE seen in Figure 4.8.

4.9 Conclusions

This chapter demonstrates that, compared to a microscale-only simulation, a multiscale simulation can substantially improve predictions of transport and mixing and TKE. Two simulation configurations are compared; a traditional microscale-only simulation and a six-domain multiscale simulation. These simulations predict meteorology and the transport and mixing of SF_6 throughout the central business district of Oklahoma City, OK, during the JU2003 field campaign. The microscale-only simulation uses a two-domain nested configuration with idealized boundary conditions and forcing that is tuned using local observations

from JU2003. The multiscale simulation uses a six-domain nested configuration with initial conditions and forcing provided by NARR, a meteorological forecast product.

Several statistical measures of model skill are used to evaluate the performance of each simulation versus JU2003 observations. As was observed in Chapter 2 and Wiersema et al. (2020), the microscale-only simulation shows the most skill at predicting wind speed and direction due to tuning of the simulation forcing to match JU2003 observations. The multiscale simulation shows the most skill at predicting both SF_6 concentrations and TKE. The superior skill of the multiscale simulation results from downscaling of large-scale turbulence through a telescoping series of nested domains. These results demonstrate the importance of including large-scales when forcing a microscale simulation.

Enabling the CPM of Muñoz-Esparza et al. (2015) was found to promote the development of turbulence and improve the transition from a RANS parent domain to a LES child domain, however the associated increased downward transport of high momentum flow exacerbated the existing positive wind speed bias in the 30 m and 10 m domains. Future research should focus on reducing this positive wind speed bias by improving the representation of poorly resolved obstacles, such as buildings, and including their effects on flow in the intermediate resolution domains. Additionally, future studies should consider more advanced turbulence closures, such as the dynamic reconstruction model (Chow et al. 2005), that may improve the development of turbulence at intermediate resolutions.

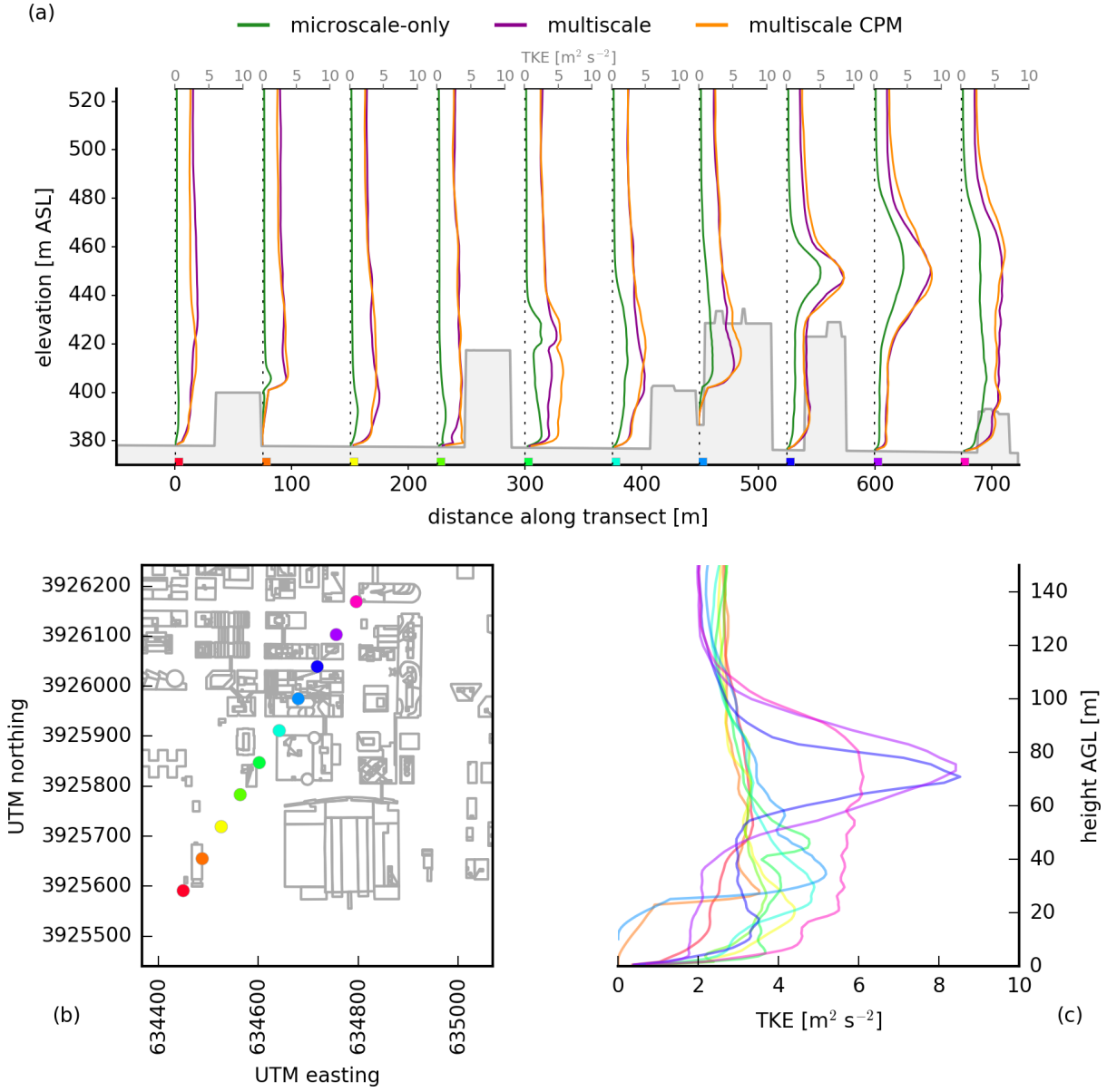

Figure 4.6: Vertical profiles of TKE from the Δ=2 m domains along a transect between the ANL miniSODAR and DPG PWIDS 03 (a), profile locations within the 2 m domain (b), and vertical profiles of TKE from the multiscale CPM simulation with line-color corresponding to the profile location (c). All vertical profiles have been time-averaged over the SF_6 release period (1600-1630 UTC). The red marker at the south west corner of (b) corresponds to the ANL miniSODAR. The pink marker that is nearest to the northern boundary in (b) corresponds to the DPG PWIDS 03.

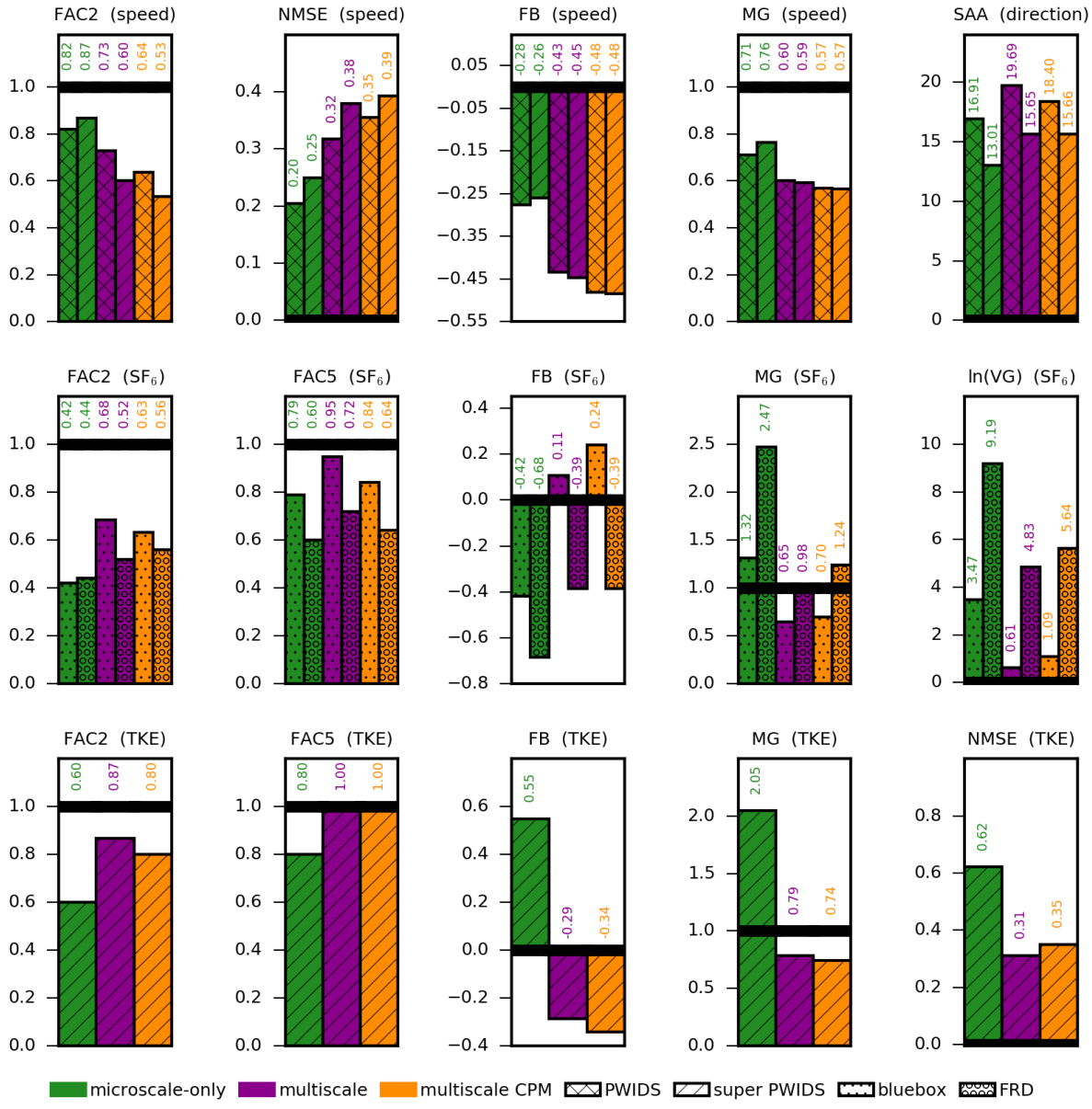

Figure 4.7: Model skill test results evaluating horizontal wind speed and wind direction (top row), SF_6 concentration (middle row), and turbulence kinetic energy (bottom row) for the microscale-only simulation and multiscale simulations with and without CPM. Simulation results are evaluated against DPG PWIDS and super PWIDS, LLNL "bluebox" and NOAA ARL FRD integrated tracer samplers. The thick black lines represent the score of a perfect model.

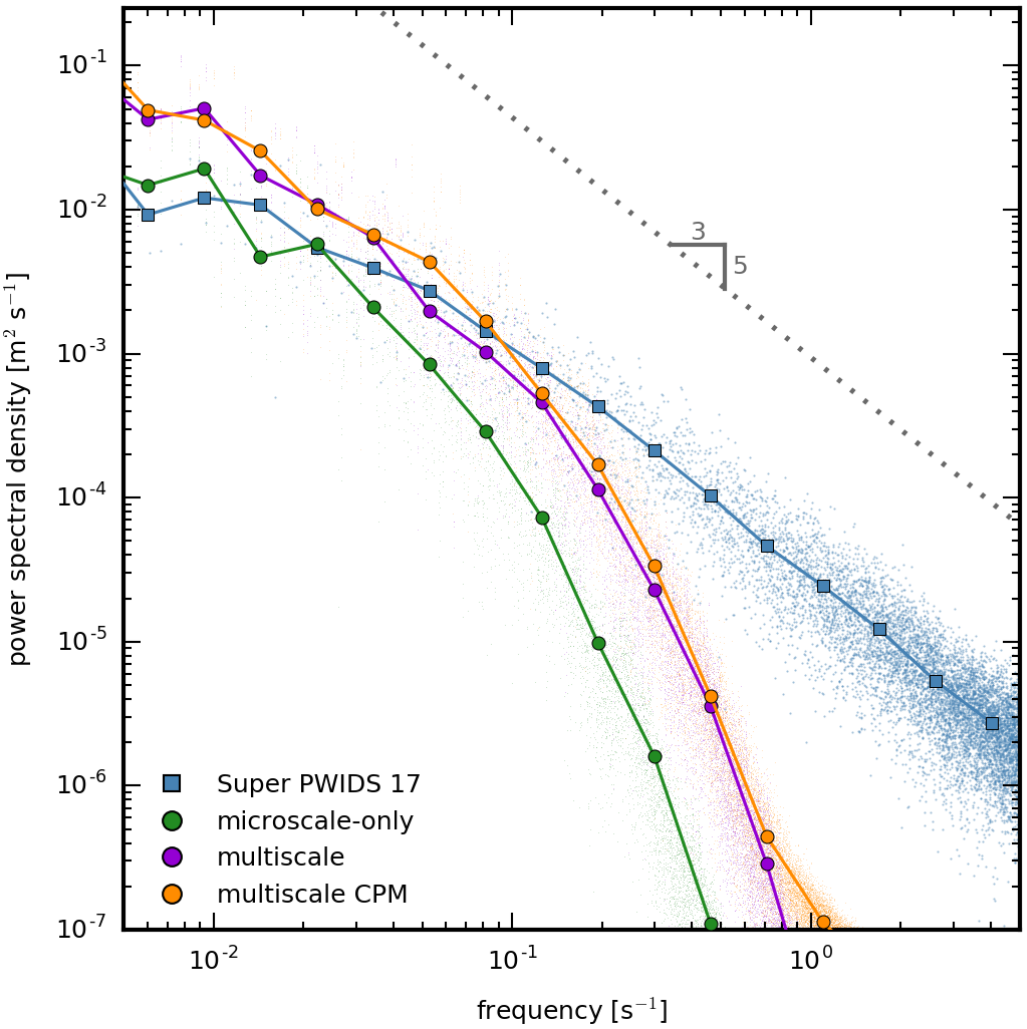

Figure 4.8: Frequency spectra of turbulent kinetic energy (TKE) at 8 m above ground level at the SF_6 release location. Included on this plot are observations from the DPG Super PWIDS 17 and simulation results from three model configurations; microscale-only, multiscale, and multiscale with the cell perturbation method. The large markers are mean values of frequency bins.

Chapter 5

Conclusions and recommendations

5.1 Summary of findings

Mesoscale to microscale atmospheric simulations

Multiscale atmospheric simulations over complex terrain are demonstrated using the WRF model with the immersed boundary method, vertical grid refinement, and a cell perturbation method. These WRF developments allow for realistic meteorology and large-scale turbulence to be downscaled from a NWP meteorological forecast product through a telescoping sequence of nested domains and ultimately force a microscale simulation over complex urban terrain.

A five-domain multiscale WRF simulation is demonstrated with the model initialization and mesoscale forcing supplied by the NARR dataset. This simulation predicts transport and mixing of a passive tracer gas (SF_6) released during the third intensive observational period of the Joint Urban 2003 field campaign in the central business district of Oklahoma City, OK. The simulation's five domains have horizontal resolutions of 6050, 550, 50, 10 and 2 m. The IBM VRM algorithm (Bao et al. 2018; Wiersema et al. 2020) is enabled for the 10 and 2 m domains. This algorithm is especially useful since it does not rely upon ghost points, which greatly simplifies the nesting of an IBM VRM child domain inside of a traditional terrain-following WRF parent domain.

A vertical grid nesting procedure (Daniels et al. 2016) is used to specify the number and placement of vertical grid levels in each of the five domains. Crucially, this provides control over the grid aspect ratio of the domains using a large-eddy simulation turbulence closure model.

In addition to the multiscale simulation in Chapter 2, two microscale-only model configurations are also evaluated. The microscale-only configurations are representative of typical microscale large-eddy simulations from the literature, such as those by Golaz et al. (2009); Lundquist et al. (2012); and Bao et al. (2018). The two configurations differ only in the choice of IBM algorithm, which is either the no-slip ghost point method of Lundquist et al. (2012) or the velocity reconstruction method of Bao et al. (2018).

Both microscale-only configurations use a two-domain nested configuration with horizontal resolutions of 10 and 2 m. Periodic lateral boundary conditions are applied to the 10 m parent domain, which is allowed to develop turbulence and reach a quasi-steady-state prior to initializing the 2 m domain. The 2 m domain of these microscale-only simulations is configured to be as similar as possible to the 2 m domain of the multiscale simulation.

Qualitative analysis of the wind field solution and SF_6 plume from each simulation shows similar behavior of the microscale simulations. In the time series of horizontal wind speed and wind direction, Figure 2.10, the multiscale simulation displays an increased variability of the wind speed and wind direction, which results in additional SF_6 plume meandering relative to the microscale-only simulations. This effect is pronounced in the time-averaged SF_6 plumes shown in Figure 4.3, where the multiscale simulation's plume is much wider and includes significantly more transport upwind of the SF_6 release location.

Quantitative analysis of the microscale-only and multiscale simulations involves a suite of model skill metrics suggested in Chang and Hanna (2004) and Calhoun et al. (2004) that are used to evaluate the performance of each simulation for the prediction of wind speeds, wind directions, and SF_6 concentrations. A graphical representation of the simulations' model skill is included in Figure 2.12.

The relative performance of the two IBM algorithms is evaluated by comparing the model skill of the microscale-only simulations. The microscale-only simulation using the VRM IBM algorithm shows slightly improved model skill compared to that using the GPM IBM algorithm. This improvement is attributed to the VRM algorithm enforcing a log-law boundary condition, which, at the resolutions being evaluated, is more appropriate than the GPM algorithm's no-slip boundary condition.

The impact of downscaling realistic meteorology is evaluated by comparing the skill of the microscale-only simulations to that of the multiscale simulation. The microscale-only simulations have higher model skill at predicting wind speeds and wind direction. This is expected because the microscale-only simulations are tuned using local observations. Despite not being tuned using local observations, the multiscale simulation outperforms the microscale-only simulations at predicting SF_6 concentrations. This is attributed to differences in the forcing, such as the large-scale flow features from the mesoscale and intermediate resolution domains of the multiscale simulation.

All three simulations overestimate the near-surface wind speed, as shown in Figure 2.5, which shows vertical profiles of time-averaged wind speed above a location near the inflow of the 2 m domain. It is hypothesized that this overestimation is due to upstream roughness elements (i.e. buildings and vegetation) that are not well represented in the intermediate resolution domains. This hypothesis is tested by introducing large rectangular roughness elements in the 10 m domain to represent the missing sources of drag. The simulation with these roughness elements shows improved agreement with the vertical profile of wind speed observed near the inflow and shown in Figure 2.5. Future research should include treatments on the intermediate resolution domains for poorly resolved sources of roughness, such as buildings and vegetation.

Investigation of sensitivity to grid resolution

Chapter 3 includes a series of simulations over a steep idealized hill that explore the parameter space of grid resolution and surface boundary condition (i.e. IBM algorithm). The primary objective of this sensitivity study is to better inform future multiscale modeling efforts over complex terrain. In particular, this study seeks to improve domain configurations at intermediate resolutions (i.e. 25 m $\lesssim \Delta \lesssim$ 200 m) where there are presently no obvious "best practices".

Simulations at 25, 50, 100 and 200 m grid resolution are evaluated using the standard WRF bottom boundary condition and terrain-following coordinates, the velocity reconstruction method IBM algorithm (Senocak et al. 2004; Bao et al. 2018), and the shear reconstruction method IBM algorithm (Chester et al. 2007; Bao et al. 2016; Ma and Liu 2017). These 12 configurations are also evaluated with a hybrid RANS/LES scheme (Senocak et al. 2007), which blends solutions for the eddy viscosity from the Smagorinsky turbulence closure away from the surface and a RANS solution near the surface.

Each of the simulations is evaluated relative to the 25 m resolution standard WRF simulation, which is treated as a "true" solution. An emphasis is placed on the solution within 100 m of the surface. Domain-averaged error over the bottom 100 m is evaluated for each of the simulations. The spatial distribution of error is thoroughly investigated, including an analysis of error along a transect through the domain center and aligned with the predominant wind direction.

The results of this study are distilled into several "best practices". First, terrain-following coordinates should be used for domains where the resolved topographic slopes are mild or moderate and the corresponding numerical errors are manageable. Second, there is a large sensitivity to the surface boundary condition at all resolutions tested and modelers should not assume that high grid resolution will negate errors from an inappropriate surface boundary condition. Third, the SRM IBM algorithm outperformed the VRM IBM algorithm, however the SRM IBM requires ghost points and cannot be used on a domain nested within a terrain-following parent domain. The SRM IBM should be used if an IBM is necessary and the simulation can support the restrictions imposed by the algorithm. Finally, the hybrid RANS/LES scheme of Senocak et al. (2007) yielded improved results at all resolutions tested and is highly recommended for use at similar grid resolutions (i.e. 25 $\lesssim \Delta \lesssim$200 m).

Investigation and comparison of turbulence represented in microscale and multiscale simulations

Chapter 4 investigates the downscaling of turbulence in a slightly altered configuration of the multiscale simulation from Chapter 2 and compares the results to those from a microscale-only simulation. The updated multiscale configuration has six domains with resolutions of 4950, 1650, 330, 30, 10 and 2 m. Changes in the domain resolutions are intended to improve the development of turbulence in the intermediate resolution domains. A 30 m resolution is used for the first LES domain versus the 50 m resolution used in the previous multiscale

simulation. The microscale-only configuration remains unchanged with a 10 m resolution parent domain with periodic lateral boundary conditions and a 2 m resolution child domain.

The multiscale simulation is run with and without the cell perturbation method from Muñoz-Esparza et al. (2014, 2015); Muñoz-Esparza and Kosović (2018). The CPM introduces small potential temperature perturbations within the PBL and along inflow lateral boundaries. When transitioning from a parent domain using a PBL scheme to an LES child domain, the CPM can promote the development of small-scale turbulence following transition across a grid refinement interface.

As in Chapter 2, the microscale-only and multiscale simulations (with and without the CPM) are compared to JU2003 observations, however additional consideration is given to the resolved turbulence kinetic energy throughout the 2 m domain. TKE is calculated from sonic anemometers deployed during JU2003 and compared to that resolved in the simulations. The model skill metrics used in Chapter 2 are also applied to these simulations for evaluating wind speed, wind direction, SF_6 concentrations and TKE.

Figure 4.7 shows a graphical comparison of the model skill from the microscale-only and multiscale simulations. The relative behavior is similar to what was reported in Chapter 2 and Wiersema et al. (2020). The microscale-only simulation, which is tuned using local observations, best predicts wind speeds and directions, however the multiscale simulation best predicts SF_6 concentrations. Importantly, the multiscale simulation also best predicts TKE, with a slight overestimate versus the large underestimate by the microscale-only simulation. This is hypothesized to be a result of downscaled large-scale flow features and turbulence, which cannot be resolved in the microscale-only simulations.

With the CPM enabled, the skill of the multiscale simulation decreases slightly for predictions of wind speed, SF_6 concentration, and TKE. This reduction is thought to result from the CPM causing an increase in the energetic large-scale flow features that contribute heavily to the resolved TKE. These additional energetic flow features cause an increase in the vertical transport and mixing of high momentum flow from aloft to the near-surface. This results in higher wind speeds and resolved TKE. Even with the CPM disabled, the multiscale simulation overpredicts both wind speeds and TKE. This problem is exacerbated by enabling the CPM.

Qualitative analysis confirms the underprediction of TKE by the microscale simulation and overprediction by the multiscale simulation. This qualitative analysis includes a visual comparison of horizontal contours of resolved TKE from the three simulations and vertical profiles of resolved TKE along a transect through the central business district, shown in Figures 4.5 and 4.4, respectively.

A spectral analysis of resolved TKE at the SF_6 release location, shown in Figure 4.8, displays trends expected by the conclusions from the qualitative analysis and the analysis of model skill scores. Both multiscale simulations resolve more energy at all scales than the microscale-only simulation. Enabling the CPM slightly increases the resolved TKE at most scales. Relative to sonic anemometer observations, both of the multiscale simulations overpredict energy at the large scales and underpredict energy at the small scales. A more sophisticated LES turbulence closure model, such as the dynamic reconstruction model (Chow

et al. 2005), may reduce the persistence of large-scale coherent features and increase the energy contained in small scale motions.

5.2 Recommendations for future research and development

While multiscale atmospheric modeling over complex terrain is achievable using the framework developed and described here, there are many opportunities for improvement of the existing modeling methods and tools.

The IBM algorithm is one potential method that should be a focus for future development and improvement. In particular, the velocity reconstruction method IBM algorithm, which is used in the multiscale simulations of Chapters 2 and 4, works well at the microscale but is less accurate at more coarse resolutions. The simplicity of the VRM IBM algorithm contributes to the method being robust enough to handle complex urban terrain at high resolutions, however more advanced methods should be investigated for use at resolutions greater than approximately 2 m. Future developers of IBM algorithms for the WRF model should be cautious of algorithms that require ghost points beneath the IB, as the governing equations of the model have fundamental problems associated with nesting domains that do not share bottom and top pressure levels along the refinement interfaces.

Another model development for consideration is an IBM algorithm to enforce a flux boundary condition for scalar variables (i.e. potential temperature, moisture, chemical species, and tracers) without requiring ghost points. Such a method is simple to develop for uncomplicated topography, however urban IB geometries prove challenging as the interpolation scheme may have few options for nearest neighbors and select grid points that result in a feedback effect. This is particularly problematic when modifying potential temperature and moisture since a grid point with an inaccurate solution for these variables will affect the pressure and result in spurious flow.

The multiscale simulations in Chapters 2 and 4 are configured with static data sets, including topography and land use, at a low resolution relative to the microscale grids. While not insurmountable, there are several nuanced challenges associated with the use of higher resolution static data sets. First, it can be quite difficult to gather and assemble enough tiles of a data set to cover the spatial extent of the mesoscale resolution domains in a multiscale simulation. The WRF model version 3.8.1 requires uniform tile dimensions for static data sets, which complicates the manual manipulation required for high resolution data sets when many tiles are necessary. Additionally, if different data sets are used for mesoscale and microscale domains then these data sets are required to share any necessary lookup tables.

As discussed in Chapter 4, domains at resolutions within the turbulence gray zone are likely to benefit from a more sophisticated LES turbulence closure model. The dynamic reconstruction model (DRM) (Chow et al. 2005; Kirkil et al. 2012) would be an excellent

choice due to consistent performance across a wide range of grid resolutions (Simon et al. 2019). Development of the DRM for use with an IBM would require intelligent adjustment of filters when in proximity to the IB.

Another potential enhancement for the multiscale simulations is an improved treatment for poorly resolved subgrid-scale topographic features, particularly in the intermediate resolution domains. One possible solution may be to introduce drag at grid cells where buildings are present. A canopy model framework could be another useful option (Arthur et al. 2018b).

Configuring each nested grid in a multiscale simulation involves numerous decisions that, for the moment, are primarily based upon the modeler's judgement because there are few established "best practices". Chapter 3 begins to investigate the model performance at grid resolutions within the turbulence gray zone, however many additional studies are needed to better inform future multiscale modeling efforts. It is recommended that these studies investigate the model's sensitivity to grid resolution, nesting refinement ratio, grid aspect ratio, and choice of LES turbulence closure model.

5.3 Advice for multiscale atmospheric modeling

An important, although quite obvious, lesson learned from this study was that an inaccurate solution in an intermediate or mesoscale resolution domain will result in an inaccurate solution in the microscale resolution domains. When modelers evaluate future multiscale simulations, they should cautiously evaluate the accuracy of each simulation domain. Relative to a microscale-only simulation, the many domains of a multiscale simulation provide additional opportunities for the introduction of errors, which influence the solution at the microscale. As demonstrated here, multiscale simulations can greatly benefit from the intermediate and mesoscale resolution domains, however they also complicate the model configuration process.

Similar to the lesson above, modelers should reduce the simulation complexity by only modeling the scales where high quality forecasts do not yet exist. This was demonstrated by a multiscale configuration, not shown here, that was similar to that in Chapter 2 however, for purely aesthetic purposes, the outermost domain covered a much larger spatial extent that included the Rocky Mountains and a significant portion of the Gulf of Mexico. Configuring this outermost domain proved to be challenging due to inaccurate sea surface temperatures and the complications introduced by the Rocky Mountains. Ultimately, a much improved result was achieved by relying more heavily on the NARR forecast product and reducing the domain extent such that the Gulf of Mexico and the Rocky Mountains were no longer included in the simulation domain.

When evaluating future multiscale simulations, care should be taken to ensure that high skill scores are due to the physical accuracy of the model and not due to compensating errors. An illustrative example of this can be seen in Chapter 4. The 30 m domain's flow solution is quite smooth relative to a comparable simulation with periodic lateral boundary conditions. Relatively speaking, a reduction in turbulent mixing yields a reduction in the vertical transport of momentum and thus a reduction in the near-surface wind speed. Mean-

while, large sources of drag, such as buildings and vegetation, are poorly represented on intermediate resolution domains, which adds a positive bias to the near-surface wind speeds due to missing drag. These inaccuracies appear to be compensating, and result in a slight overestimate in near-surface wind speeds. This theory is reinforced by enabling the CPM, which improves the development of turbulence, which increases momentum transport and near-surface wind speeds.

Bibliography

Allwine, J., and J. Flaherty, 2006: Joint Urban 2003: Study overview and instrument locations. Tech. Rep. PNNL-15967, Pacific Northwest National Laboratory. [Available online at https://pnnl.gov/main/publications/external/technical_reports/PNNL-15967.pdf].

Arthur, R., K. Lundquist, J. Mirocha, and F. K. Chow, 2018a: Topographic effects on radiation in the WRF model with the immersed boundary method: implementation, validation, and application to complex terrain. *Monthly Weather Review*, in press.

Arthur, R. S., K. A. Lundquist, D. J. Wiersema, J. Bao, and F. K. Chow, 2019: Evaluating implementations of the immersed boundary method in the weather research and forecasting model. *Monthly Weather Review*, in preparation.

Arthur, R. S., J. D. Mirocha, K. A. Lundquist, and R. L. Street, 2018b: Using a canopy model framework to improve large-eddy simulations of the neutral atmospheric boundary layer in the weather research and forecasting model. *Monthly Weather Review*, **147 (1)**, 31–52.

Baklanov, A., A. Rasmussen, B. Fay, E. Berge, and S. Finardi, 2002: Potential and shortcomings of numerical weather prediction models in providing meteorological data for urban air pollution forecasting. *Urban Air Quality - Recent Advances, Proceedings*, 43–60, 3rd International Conference on Urban Air Quality - Measurement, Modeling and Management, Loutraki, Greece, March 20-23, 2001.

Bao, J., 2018: An improved immersed boundary method for atmospheric boundary layer simulations over complex terrain. Ph.D. thesis, University of California, Berkeley.

Bao, J., K. Lundquist, and F. K. Chow, 2016: Comparison of different implementations of the immersed boundary method in WRF. *22^{th} Symposium on Boundary Layers and Turbulence*, Salt Lake City, UT, American Meteorological Society.

Bao, J., K. Lundquist, and F. K. Chow, 2018: Large-eddy simulation over complex terrain using an improved immersed boundary method in the Weather Research and Forecasting model. *Monthly Weather Review*, **146 (9)**, 2781–2797.

Burrows, D. A., E. A. Hendricks, S. R. Diehl, and R. Keith, 2007: Modeling turbulent flow in an urban central business district. *Journal of Applied Meteorology and Climatology*, **46**, 2147–2164.

Calhoun, R., F. Gouveia, J. Shinn, S. Chan, D. Stevens, R. Lee, and J. Leone, 2004: Flow around a complex building: Comparisons between experiments and a Reynolds-averaged Navier-Stokes approach. *Journal of Applied Meteorology*, **43**, 696–710.

Chan, S., and M. Leach, 2007: A validation of FEM3MP with Joint Urban 2003 data. *Journal of Applied Meteorology and Climatology*, **46**, 2127–2146.

Chang, J., and S. Hanna, 2004: Air quality model performance evaluation. *Meteorology and Atmospheric Physics*, **87 (1–3)**, 167–196.

Charney, J. G., 1948: On the scale of atmospheric motions. *Geofysiske Publikasjoner*, **17 (2)**.

Charney, J. G., R. Fjørtoft, and J. von Neumann, 1950: Numerical integration of the barotropic vorticity equation. *Tellus*, **2 (4)**, 237–254.

Charney, J. G., and N. A. Phillips, 1953: Numerical integration of the quasi-geostrophic equations for barotropic and simple baroclinic flows. *Journal of Meteorology*, **10 (2)**, 71–99.

Chen, F., and J. Dudhia, 2001: Coupling an advanced land-surface / hydrology model with the Penn State/ NCAR MM5 modeling system. *Monthly Weather Review*, **129**, 569–585.

Chester, S., C. Meneveau, and M. B. Parlange, 2007: Modeling turbulent flow over fractal trees with renormalized numerical simulation. *Journal of Computational Physics*, **225 (1)**, 427–448.

Chow, F. K., B. Kosović, and S. Chan, 2008: Source inversion for contaminant plume dispersion in urban environments using building-resolving simulations. *Journal of Applied Meteorology and Climatology*, **47 (6)**, 1553–1572.

Chow, F. K., and R. L. Street, 2009: Evaluation of turbulence closure models for large-eddy simulation over complex terrain: Flow over Askervein hill. *Journal of Applied Meteorology and Climatology*, **48 (5)**, 1050–1065.

Chow, F. K., R. L. Street, M. Xue, and J. H. Ferziger, 2005: Explicit filtering and reconstruction turbulence modeling for large-eddy simulation of neutral boundary layer flow. *Journal of the Atmospheric Sciences*, **62 (7)**, 2058–2077.

Coen, J. L., M. Cameron, J. Michalakes, E. G. Patton, P. J. Riggan, and K. M. Yedinak, 2012: WRF-Fire: Coupled weather-wildland fire modeling with the Weather Research and Forecasting model. *Journal of Applied Meteorology and Climatology*, **52**, 16–38.

Courant, R., K. Friedrichs, and H. Lewy, 1928: Über die partiellen differenzengleichungen der mathematischen physik. *Mathematische Annalen*, **100 (1)**, 32–74.

Courant, R., K. Friedrichs, and H. Lewy, 1967: On the partial difference equations of mathematical physics. *IBM Journal of Research and Development*, **11 (2)**, 215–234.

Daniels, M., K. Lundquist, J. Mirocha, D. Wiersema, and F. K. Chow, 2016: A new vertical grid nesting capability in the weather research and forecasting (WRF) model. *Monthly Weather Review*, **144 (10)**, 3725–3747.

DeLeon, R., M. Sandusky, and I. Senocak, 2018: Simulations of turbulent flow over complex terrain using an immersed boundary method. *Boundary-Layer Meteorology*, **167 (3)**, 399–420.

Diebold, M., C. Higgins, J. Fang, A. Bechmann, and M. B. Parlange, 2013: Flow over hills: A large-eddy simulation of the Bolund case. *Boundary-Layer Meteorology*, **148 (1)**, 177–194.

Ferziger, J. H., and M. Perić, 2002: *Computational Methods for Fluid Dynamics*. third, rev. ed., Springer.

García-Sánchez, J. van Beeck, and C. Gorlé, 2018: Predictive large eddy simulations for urban flows: Challenges and opportunities. *Building and Environment*, **139**, 146–156.

Golaz, J.-C., J. D. Doyle, and S. Wang, 2009: One-way nested large-eddy simulation over the Askervein hill. *Journal of Advances in Modeling Earth Systems*, **1**.

Gowardhan, A. A., E. R. Pardyjak, I. Senocak, and M. J. Brown, 2011: A cfd-based wind solver for an urban fast response transport and dispersion model. *Environmental Fluid Mechanics*, **11**, 439–464.

Grell, G. A., S. E. Peckham, R. Schmitz, S. A. McKeen, G. Frost, W. C. Skamarock, and B. Elder, 2005: Fully coupled "online" chemistry within the WRF model. *Atmospheric Environment*, **39**, 6957–6975.

Hanna, S., D. Strimaitis, and J. Chang, 1993: Hazard Response Modeling Uncertainty (A Quantitative Method) Vol I - User's Guide for Software for Evaluating Hazardous Gas Dispersion Models. Tech. Rep. AFESC Contract No. FO8653-89-C-0136, H.Q. AFESC/RDVS, Tyndall AFB, FL 32403, 71 pp.

Hanna, S., and Coauthors, 2011: Comparisons of JU2003 observations with four diagnostic urban wind flow and Lagrangian particle dispersion models. *Atmospheric Environment*, **45**, 4073–4081.

Holton, J. R., 2004: *An Introduction to Dynamic Meteorology*. Fourth edition ed., Elsevier Academic Press, Burlington, MA.

Hutchins, N., and I. Marusic, 2007: Evidence of very long meandering features in the logarithmic region of turbulent boundary layers. *Journal of Fluid Mechanics*, **579**, 1–28.

Iaccarino, G., and R. Verzicco, 2003: *Applied Mechanics Review*, **56 (3)**, 331–347.

Jafari, S., N. Chokani, and R. S. Abhari, 2012: An immersed boundary method for simulation of wind flow over complex terrain. *Journal of Solar Energy Engineering-Transactions of the ASME*, **134 (1)**, 011 006–011 006–12.

Janjić, Z., 2002: Nonsingular implementation of the Mellor-Yamada level 2.5 scheme in the NCEP Meso model. Tech. Rep. NCEP Office Note #437, National Centers for Environmental Protection, 61 pp.

Kirkil, G., J. Mirocha, E. Bou-Zeid, F. K. Chow, and B. Kosović, 2012: Implementation and evaluation of dynamic subfilter-scale stress models for large-eddy simulation using WRF. *Monthly Weather Review*, **140**, 266–284.

Klemp, J. B., 2011: A terrain-following coordinate with smoothed coordinate surfaces. *Monthly Weather Review*, **139 (7)**, 2163–2169.

Klemp, J. B., W. C. Skamarock, and O. Fuhrer, 2003: Numerical consistency of metric terms in terrain-following coordinates. *Monthly Weather Review*, **131 (7)**, 1229–1239.

Knievel, J. C., G. H. Bryan, and J. P. Hacker, 2007: Explicit numerical diffusion in the WRF model. *Monthly Weather Review*, **135 (11)**, 3808–3824.

Lee, G.-J., D. Muñoz-Esparza, C. Yi, and H. J. Choe, 2019: Application of the cell perturbation method to large-eddy simulations of a real urban area. *Journal of Applied Meteorology and Climatology*, **58 (5)**, 1125–1139.

Lesieur, M., and O. Métais, 1996: New trends in large-eddy simulations of turbulence. *Annual Review of Fluid Mechanics*, **28 (1)**, 45–82.

Li, H., G. Cui, and Z. Zhang, 2018: A new scheme for the simulation of microscale flow and dispersion in urban areas by coupling large-eddy simulation with mesoscale models. *Boundary-Layer Meteorology*, **167**, 145–170.

Li, Q., E. Bou-Zeid, and W. Anderson, 2016: The impact and treatment of the Gibbs phenomenon in immersed boundary method simulations of momentum and scalar transport. *Journal of Computational Physics*, **310**, 237–251.

Lorenz, E. N., 1963: Deterministic nonperioidic flow. *Journal of the Atmospheric Sciences*, **20**, 130–141.

Ludwig, F. L., F. K. Chow, and R. L. Street, 2009: Effect of turbulence models and spatial resolution on resolved velocity structure and momentum fluxes in large-eddy simulations of neutral boundary layer flow. *Journal of Applied Meteorology and Climatology*, **48**, 1161–1180.

Lundquist, K., 2010: Immersed boundary methods for high-resolution simulation of atmospheric boundary-layer flow over complex terrain. Ph.D. thesis, University of California, Berkeley.

Lundquist, K., F. K. Chow, and J. Lundquist, 2010: An immersed boundary method for the Weather Research and Forecasting model. *Monthly Weather Review*, **138**, 796–817.

Lundquist, K., F. K. Chow, and J. Lundquist, 2012: An immersed boundary method enabling large-eddy simulations of complex terrain in the WRF model. *Monthly Weather Review*, **140 (12)**, 3936–3955.

Ma, Y., and H. Liu, 2017: Large-eddy simulations of atmospheric flows over complex terrain using the immersed-boundary method in the Weather Research and Forecasting model. *Boundary-Layer Meteorology*, **165 (3)**, 421–445.

Mahrer, Y., 1984: An improved numerical approximation of the horizontal gradients in a terrain-following coordinate system. *Monthly Weather Review*, **112 (5)**, 918–922.

Marjanovic, N., S. Wharton, and F. K. Chow, 2014: Investigation of model parameters for high-resolution wind energy forecasting: Case studies over simple and complex terrain. *Journal of Wind Engineering and Industrial Aerodynamics*, **134**, 10–24.

Mellor, G., and T. Yamada, 1982: Development of a turbulence closure-model for geophysical fluid problems. *Reviews of Geophysics*, **20 (4)**, 851–875.

Mesinger, F., and Coauthors, 2006: North American Regional Reanalysis: A long-term, consistent, high-resolution climate dataset for the North American domain, as a major improvement upon the earlier global reanalysis datasets in both resolution and accuracy. *Bulletin of the American Meteorological Society*, **87**, 342–360.

Mirocha, J., G. Kirkil, E. Bou-Zeid, F. K. Chow, and B. Kosović, 2013: Transition and equilibrium of neutral atmospheric boundary layer flow in one-way nested large-eddy simulations using the Weather Research and Forecasting model. *Monthly Weather Review*, **141**, 918–940.

Mirocha, J., J. Lundquist, and B. Kosović, 2010: Implementation of a nonlinear subfilter turbulence stress model for large-eddy simulation in the advanced research WRF model. *Monthly Weather Review*, **138**, 4212–4228.

Mirocha, J., and K. Lundquist, 2017: Assessment of vertical mesh refinement in concurrently nested large-eddy simulations using the Weather Research and Forecasting model. *Monthly Weather Review*, **145 (8)**, 3025–3048.

Mittal, R., and G. Iaccarino, 2005: Immersed boundary methods. *Annual Review of Fluid Mechanics*, **37**, 239–261.

Moeng, C.-H., J. Dudhia, J. Klemp, and P. Sullivan, 2007: Examining two-way grid nesting for large eddy simulation of the PBL using the WRF model. *Monthly Weather Review*, **135**, 2295–2311.

Monin, A. S., and A. M. Obukhov, 1954: Basic laws of turbulent mixing in the surface layer of the atmosphere. *Tr. Akad. Nauk SSSR Geophiz. Inst.*, **24 (151)**, 163–187.

Muñoz-Esparza, D., and B. Kosović, 2018: Generation of inflow turbulence in large-eddy simulations of nonneutral atmospheric boundary layers with the cell perturbation method. *Monthly Weather Review*, **146 (6)**, 1889–1909.

Muñoz-Esparza, D., B. Kosović, J. Mirocha, and J. van Beeck, 2014: Bridging the transition from mesoscale to microscale turbulence in numerical weather prediction models. *Boundary-Layer Meteorology*, **153**, 409–440.

Muñoz-Esparza, D., B. Kosović, J. van Beeck, and J. Mirocha, 2015: A stochastic perturbation method to generate inflow turbulence in large-eddy simulation models: Application to neutrally stratified atmospheric boundary layers. *Physics of Fluids*, **27 (035102)**.

Nelson, M. A., M. J. Brown, S. A. Halverson, P. E. Bieringer, A. Annunzio, G. Bieberbach, and S. Meech, 2016: A case study of the Weather Research and Forecasting model applied to the Joint Urban 2003 tracer field experiment. part 2: Gas tracer dispersion. *Boundary-Layer Meteorology*, **161 (3)**, 461–490.

Neophytou, M., A. Gowardhan, and M. Brown, 2011: An inter-comparison of three urban wind models using Oklahoma City Joint Urban 2003 wind field measurements. *Journal of Wind Engineering and Industrial Aerodynamics*, **99**, 357–368.

Panofsky, H., and J. Dutton, 1984: *Atmospheric Turbulence*. A Wiley interscience publication, Wiley.

Park, S.-B., J.-J. Baik, and S.-H. Lee, 2015: Impacts of mesoscale wind on turbulent flow and ventilation in a densely built-up urban area. *Journal of Applied Meteorology and Climatology*, **54**, 811–824.

Peskin, C. S., 1972: Flow patterns around heart valves: A digital computer method for solving the equations of motion. Ph.D. thesis, Albert Einstein College of Medicine, [Available online at http://www.umi.com/hp/Products/DisExpress.html order no. 7230378].

Ray, P. S., 1986: *Mesoscale Meteorology and Forecasting*. American Meteorological Society, Boston.

Richardson, L. F., 1922: *Weather Prediction by Numerical Process*. Cambridge University Press, Boston, 66 pp.

Senocak, I., A. Ackerman, D. Stevens, and N. Mansour, 2004: Topography modeling in atmospheric flows using the immersed boundary method. Annual research briefs, Center for Turbulence Research, NASA Ames/Stanford University, 11 pp. [Available online at https://ntrs.nasa.gov/archive/nasa/casi.ntrs.nasa.gov/20050061074.pdf].

Senocak, I., A. S. Ackerman, M. P. Kirkpatrick, D. E. Stevens, and N. N. Mansour, 2007: Study of near-surface models for large-eddy simulations of a neutrally stratified atmospheric boundary layer. *Boundary-Layer Meteorology*, **124**, 405–424.

Silva Lopes, A., J. Palma, and F. A. Castro, 2007: Simulation of the askervein flow. part 2: Large-eddy simulations. *Boundary-Layer Meteorology*, **125**, 85–108.

Simon, J. S., B. Zhou, J. D. Mirocha, and F. K. Chow, 2019: Explicit filtering and reconstruction to reduce grid dependence in convective boundary layer simulations using wrf-les. *Monthly Weather Review*, **147 (5)**, 1805–1821.

Skamarock, W., 2004: Evaluating mesoscale NWP models using kinetic energy spectra. *Monthly Weather Review*, **132 (12)**, 3019–3032.

Skamarock, W. C., J. B. Klemp, M. G. Duda, L. Fowler, S.-H. Park, and T. D. Ringler, 2012: A multi-scale nonhydrostatic atmospheric model using centroidal voronai tesselations and c-grid staggering. *Monthly Weather Review*, **140 (9)**.

Skamarock, W. C., and Coauthors, 2008: A description of the advanced research WRF version 3. NCAR Technical Note TN-475+STR, National Center for Atmospheric Research. [Available online at https://www2.mmm.ucar.edu/wrf/users/docs/technote/v3_technote.pdf].

Smagorinsky, J., 1963: General circulation experiments with the primitive equations. *Monthly Weather Review*, **91 (3)**, 99–164.

Stauffer, D. R., and N. L. Seaman, 1990: Use of four-dimensional data assimilation in a limited-area mesoscale model. part i: Experiments with synoptic-scale data. *Monthly Weather Review*, **118**, 1250–1277.

Stull, R. B., 1988: *An Introduction to Boundary Layer Meteorology*. Kluwer Academic Publishers.

Sullivan, P., J. C. McWilliams, and C. hoh Moeng, 1996: A grid nesting method for large-eddy simulation of planetary boundary-layer flows. *Boundary-Layer Meteorology*, **80 (1-2)**, 167–202.

Taylor, D. M., F. K. Chow, M. Delkash, and P. T. Imhoff, 2018: Atmospheric modeling to assess wind dependence in tracer dilution method measurements of landfill methane emissions. *Waste Management*, **73**, 197–209.

Tennekes, H., and J. L. Lumley, 1972: *A First Course in Turbulence*. The MIT Press, Cambridge, MA.

Tewari, M., H. Kusaka, F. Chen, W. J. Coirier, S. Kim, A. A. Wyszogrodzki, and T. T. Warner, 2010: Impact of coupling a microscale computational fluid dynamics model with a mesoscale model on urban scale contaminant transport and dispersion. *Atmospheric Research*, **96**, 656–664.

Tseng, Y.-H., C. Meneveau, and M. B. Parlange, 2006: Modeling flow around bluff bodies and predicting urban dispersion using large eddy simulation. *Environmental Science and Technology*, **40 (8)**, 2653–2662.

van Driest, E. R., 1956: On turbulent flow near a wall. *Journal of the Aeronautical Sciences*, **23 (11)**, 1007–1011.

Venkatram, A., and J. C. Wyngaard, 1988: *Lectures on Air Pollution Modeling*. American Meteorological Society.

Wiersema, D. J., K. A. Lundquist, and F. K. Chow, 2020: Mesoscale to microscale simulations over complex terrain with the immersed boundary method in the weather research and forecasting model. *Monthly Weather Review*, **148 (2)**, 577–595.

Wyngaard, J., 2004: Toward numerical modeling in the "terra incognita". *Journal of Atmospheric Science*, **61 (14)**, 1816–1826.

Zangl, G., L. Gantner, G. Hartjenstein, and H. Noppel, 2004: Numerical errors above steep topography: A model intercomparison. *Meteorologische Zeitschrift*, **13 (2)**, 69–76.

Appendix A

American Meteorological Society full copyright notice